ABSTRACT

STEVENS, DERRICK RYAN. Molecular Dynamics in Self-assembled Monolayers and Polymers studied via sensitive Dielectric Spectroscopy. (Under the direction of Dr. Laura Clarke).

For many molecular systems, interpreting experimental molecular dynamics, by studying the response of a system to external stimuli, is a difficult task. Often the experimental response cannot be reasonably connected to a specific molecular motion. The aim of this work is to examine molecular systems where this difficulty can be overcome. We use sensitive dielectric spectroscopy to investigate the molecular dynamics of two different systems, chlorosilane self-assembled monolayers and modified siloxane polymers. The polymers studied responded to changes in their surrounding media by altering their wetting characteristics. Because this macroscopic responsive is present, we are able correlate the microscopic response (as measured by dielectric spectroscopy) to likely molecular motions. The goal of the self-assembled monolayer work is similar albeit by a different approach. In this case, the degrees of freedom were limited by using surface bound molecules. By controlling the molecular density we are able to investigate both local, non-cooperative motions as well as interacting dynamics. Specifically, we will show a connection between the interacting dynamics of the self-assembled monolayers to glass transitions found in more complicated materials.

Molecular Dynamics in Self-assembled Monolayers and Polymers studied via sensitive Dielectric Spectroscopy

by
Derrick Stevens

A dissertation submitted to the Graduate Faculty of
North Carolina State University
in partial fulfillment of the
requirements for the degree of
Doctorate of Philosophy

Physics

Raleigh, North Carolina

July 3rd, 2009

APPROVED BY:

_____	_____
Dr. Laura Clarke Committee Chair	Dr. Karen Daniels
_____	_____
Dr. Keith Weninger	Dr. David Brown

BIOGRAPHY

The author was born Aug. 8, 1982 in Nashville, Tennessee. He received his Bachelor's of Science in Physics at Tennessee Technical University in 2004. After completing his undergraduate degree he arrived the following semester at North Carolina State University to begin his Ph. D. studies.

TABLE OF CONTENTS

LIST OF TABLES

LIST OF FIGURES

Chapter 1-Introduction

The term “molecular dynamics” in modern science often brings to mind computational efforts. With computational molecular dynamics, molecules are simulated and various numerical methods are applied in an effort to solve for the atomic motion [1,2]. However, molecular dynamics are experimentally measureable, as manifest through the response of a system to external stimuli. Techniques like dielectric spectroscopy or fluorescence polarization anisotropy apply a field (electric or optical) and measure the response of the system (polarization or direction of fluorescence output) as a function of time or field frequency in order to probe the dynamics within. The difficulty in interpreting such measurements is that the system under study has so many degrees of freedom that connecting the observed system response to a particular motion is often impossible. Molecular dynamics computational calculations can then be useful in making such a connection; however, there too, the molecular size of the species under study is limited by available computational power. For instance, the most common condensed matter system where physical dynamics (rotations, translations, and the like) are studied is polymers. Polymers, which are generally rigid below their glass transition temperature and flexible above it, manifest their microscopic molecular dynamics with a change in more macroscopic physical properties. However, these very long, flexible or semi-flexible, molecules have an almost uncountable number of degrees of freedom. The difficulty is compounded by the fact that there can be multiple specific motions that exhibit similar dynamical signatures. That is, specific energies

and time scales of a certain motion are not necessarily exclusive to that motion. This flexibility is fundamental to the properties that make polymeric materials so highly useful for the myriad applications in which they are used (and their ubiquitous place in modern life), but it also contributes to the difficulties in the scientific study of these materials.

The motivation of the research described in this thesis is to explore nanoscale systems where certain degrees of freedom have been constrained or removed, but others remain present. Under such conditions, an experimental measurement of a relaxation time can be directly connected to a particular motion within that system. In this thesis, a specialized type of dielectric spectroscopy was used to measure the system relaxation time. The prototypical molecule for this work is small (which minimizes the number of bonds about which rotation can possibly occur) and rigidly attached to a surface (which minimizes translational motion). Ideally, this molecule would have only one bond about which rotation could occur, and thus essentially only one degree of freedom (see Figure 1.1). (Note: for most molecular systems, vibrations of atoms along the bond length, which could represent an additional degree of freedom, are not populated at or near room temperature and can be neglected.) In the case above, in which there is essentially one degree of freedom (rotation), the experimental measurement of the system's response time gives a measure of the actual dynamics for an individual molecule. Systems of this sort are referred to as molecular rotors and have been reviewed in Michl (2009) and Kottas et. al. (2005) [3,4].

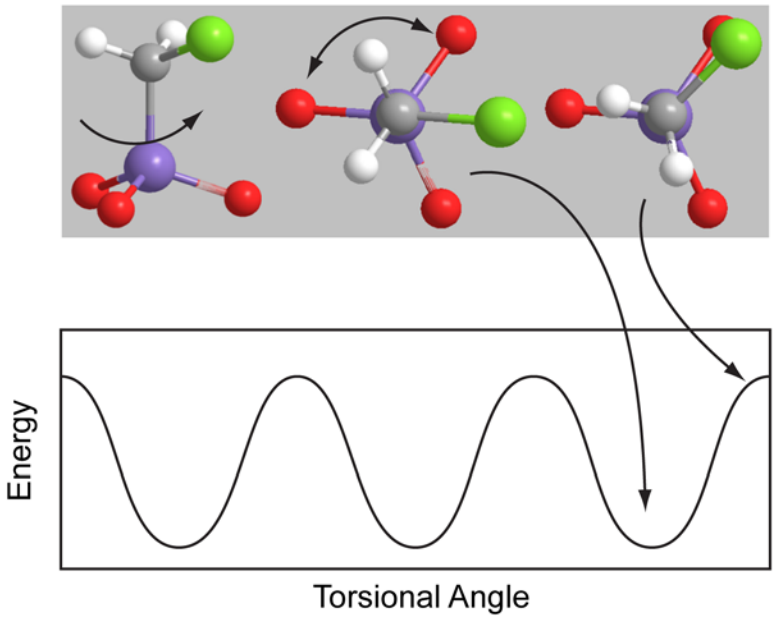

Figure 1.1: Illustration of a simple molecular rotor (top) with a corresponding 3-fold potential diagram (bottom).

In this thesis, two molecular systems and corresponding questions are explored. The first issue examined is the utilization of surface-bound molecules, slightly more complex than the idealized molecular rotor described above, to study both non-interacting and interacting dynamics and investigate our ability to observe the evolution between the two. We, also, examine how these dynamics relate to systems with more complex dynamics; namely, polymeric systems and their glass transitions. Secondly, molecular dynamics were measured for polymer based responsive surfaces. This was done in an effort to correlate the macroscopic surface response and microscopic molecular motions of the system.

A primary motivation for investigating systems of surface-bound molecules, described above, is that polymer dynamics tend to be very complex for even a single molecule. Also, experimentally, it is often a large collection of interacting molecules under study, which modifies their dynamics (giving it, for instance, a more complicated temperature dependence) and further increases the difficulty in understanding polymer dynamics. In fact, it is this interaction that leads to the presence of the glass transition temperature, below which dynamics are dramatically quenched. Because of the great complexity of the system, the glass transition, as described above, remains one of the fundamental unsolved problems in condensed matter physics. The molecular interaction for our surface-bound molecules however, can be controlled in an explicit way by changing the density of the system. We utilize self-assembled monolayer chemistry to fabricate these samples, which results in molecules randomly positioned on a substrate. Each molecule is tethered to the surface to minimize its translational motion, and the number of surface-bound molecules (i.e. sample density) can be explicitly controlled.

A more thorough examination of this molecular system is given in Section 3.3, but in general these molecules, alkylsiloxanes, consist of some reactive group for surface attachment, some carbon chain length, and may include a termination group such as bromine.

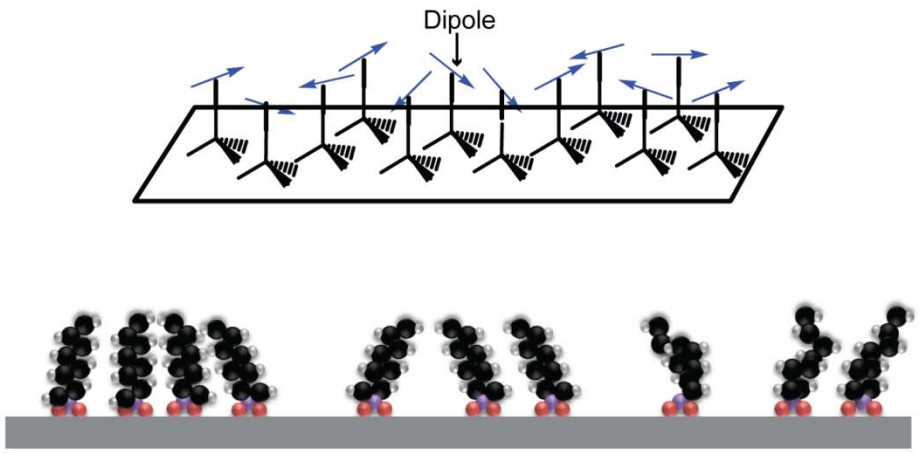

Figure 1.2: Self-assembled monolayer illustrated as randomly oriented dipoles attached to a surface (top). Illustrations of the alkylsiloxane molecules attached to a surface at various densities (bottom).

Throughout the thesis, these samples will be referred to as monolayer samples and are illustrated in Figure 1.2. Under this scheme, a rotor-like system can be used as a model for the true, and much more complex, glass transition in polymers. We are inspired in this reductionist approach by the research on glass transitions within systems where molecules are arranged in a crystal (minimizing their transitional motion) but can still rotate [5]. Such systems are referred to as plastic crystals (Figure 1.3 illustrates the differences between structural glasses, orientational glasses, and glassy monolayers). In plastic crystal systems, as the temperature is reduced, molecular interactions become important and the system undergoes a glass transition (referred to as an orientational glass transition). Our monolayer

samples system represents a complementary model to this work. The specifics of the self-assembled monolayers used are found in Section 3.3.

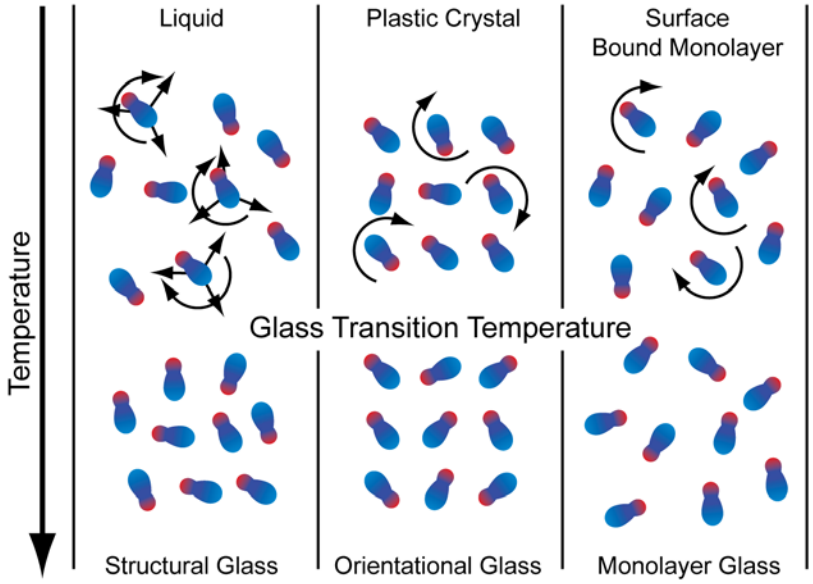

Figure 1.3: A liquid (top left) has translational and rotational degrees of freedom, both of which are quenched below the glass transition (bottom left). Additionally, the density has changed. The plastic crystal (top middle) is positionally ordered and only has rotational degrees of freedom. Below the glass transition (bottom middle) this rotation is quenched. A surface bound monolayer (top right) will have rotational freedom, however this is a positionally disordered system unlike the plastic crystal. Below the glass transition (bottom right) the disorder and density remain with the rotational motion quenched. [5]

Dielectric spectroscopy is a common experimental technique in polymer science; thus a natural way to understand the limits and advantages of our system is to measure truly polymeric systems in addition to the self-assembled monolayer systems discussed above. All polymer systems show changes in macroscopic properties that reflect their microscopic

motions; for instance, the transition in physical properties of a polymer above and below its glass transition temperature. In many novel polymer systems, such as responsive surfaces, these macroscopic dynamics can be clearly measured. A responsive polymer surface where the wetting properties change depending upon its local environment (for instance exposure to water or air) is an example of this material type (Figure 1.4). In these materials, particular molecular groups (different side chains of the polymer, if you like) have a greater affinity for certain environments (for instance water or air). Thus when exposed to a change in conditions (the stimulus in this case), the system responds by altering its microscopic configurations (literally the most conducive groups in the polymer migrate to the surface). This experiment, then, measures a macroscopic response time. We examined (in collaboration with Jan Genzer) the connection between these macroscopic response times and the microscopic response measured with dielectric spectroscopy.

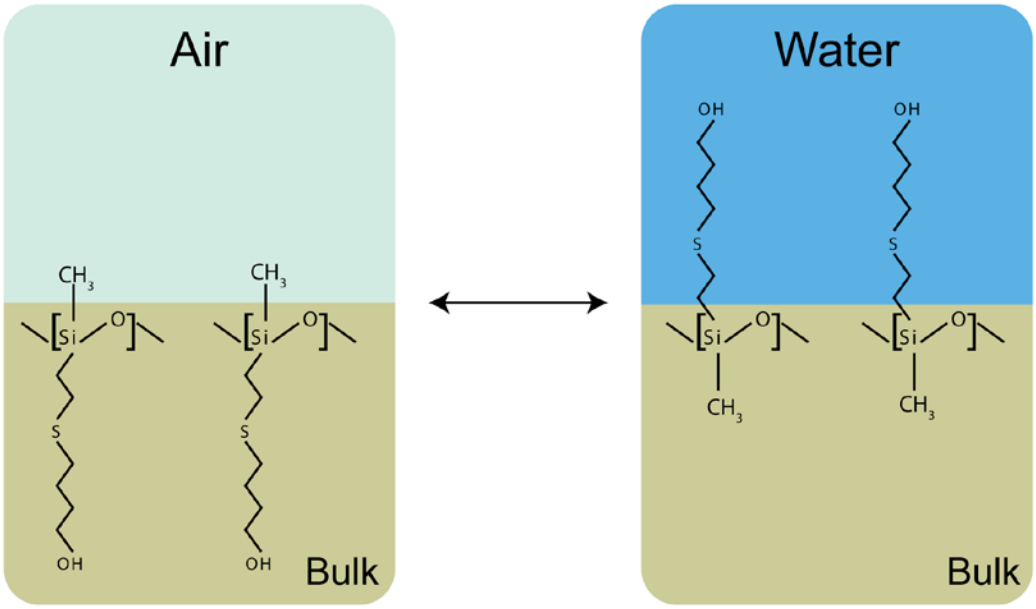

Figure 1.4: Schematic of a responsive polymer surface. Upon exposure to water the hydroxyl (OH) terminated side groups migrate to the surface. [6]

Chapter 2-Dielectric Relaxation Theory

Dielectric spectroscopy is a technique which allows observation of the dynamics of molecules in the hertz to megahertz range. This technique has been used since the 1950's to characterize molecular motion in a variety of systems, in particular it has been extensively used by the polymer community [7--9]. Besides being a well established experimental technique, advances in capacitance bridge design and sensitivity allow for the application of dielectric spectroscopy to systems containing relatively small numbers of molecules. This is particularly useful for the research presented on self-assembled monolayer systems, where techniques such as dynamical mechanical analysis (DMA) could not be used.

For dielectric spectroscopy, the material of interest is inserted as the dielectric in a capacitor (or at least, a component of the dielectric) and the properties of this capacitor -- capacitance (C) and dissipation factor (tan(δ), also referred to as the loss tangent) -- are measured as a function of the applied alternating field frequency and sample temperature. As the rate of molecular motion is altered, as dictated by the available thermal energy (which in our case is controlled by tuning the system temperature) and intrinsic barrier to that motion, so is the molecules contribution to the capacitance and dissipation factor. This is the basis of dielectric spectroscopy and a detailed explanation of why this occurs along with a corresponding theoretical framework will be given in this section. Note, this technique relies on the molecules ability to interact with an applied electric field and therefore, some type of permanent dipole must be present.

Before delving into the mathematical derivations, it is beneficial to provide a cursory examination of how the molecular motion may present itself in both the capacitance and dissipation factor. Capacitance is proportional to the polarization of the system; that is, how many dipoles are aligned in the direction of some applied electric field. The concept of loss is less familiar. Technically, the dissipation factor, tan(δ), measures the phase angle between the applied voltage and the measured current. For an ideal capacitor there is no loss; that is, the current will be exactly 90° out of phase to the voltage. A real capacitor, however, contains resistive or lossy components that will change this phase difference.

As this technique is a measurement of molecular motion, it is important to note that within the systems we study, there is no “free” molecular motion. By “free” motion we mean something like Brownian motion; in translational Brownian motion all positions have the same energy and thus a particle moves randomly, sampling many locations. In the rotational equivalent, a molecule would randomly sample all angles or orientations. In our work, all rotations (the most important type of motion in the systems under study) are constrained by a potential energy surface with wells and barriers (see Figure 2.1). In order to reorient, the molecular group must undergo a thermally-activated hopping event to overcome the barrier and transition between two neighboring wells.

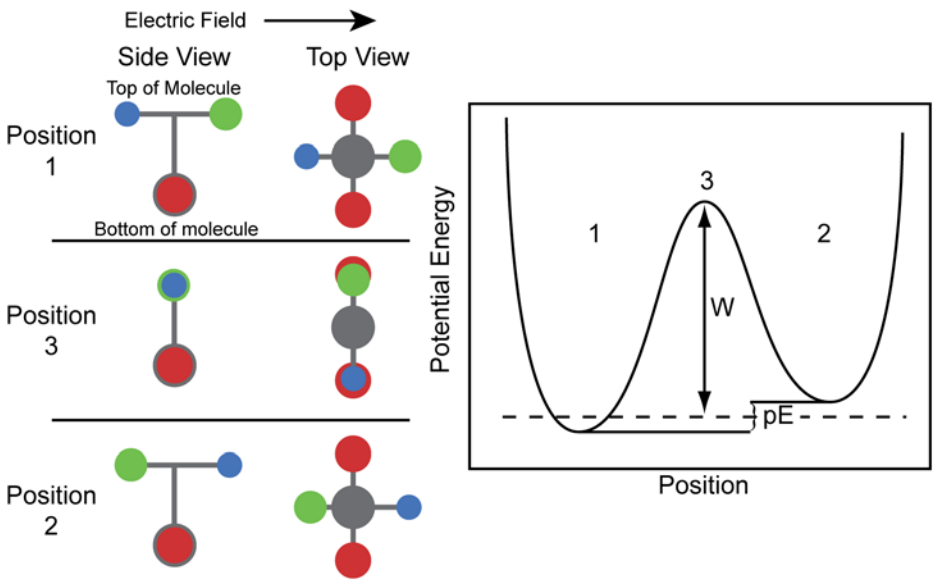

Figure 2.1: Illustration of molecular orientations with corresponding potential energy graph.

The theoretical derivations presented in section 2.2 assume a potential barrier to the molecular motion as described above, in this case a double potential well as illustrated in Figure 2.1. The essentials of the calculation remain the same for any multi-welled potential. The reorientation of the molecule, and as such the dipole moment, will only occur in instances where there is enough energy available to overcome this barrier, i.e. this is a classical treatment where tunneling is not included. The common reference to this type of motion is thermally activated hopping. The energies of most concern in this system are the interaction energy between the dipoles and the electric field (μE), the thermal energy (kT),

and the energy of the potential well (*W*). The relation of the energies typically follow *pE* (4-8 $x10^{-4}$ kcal/mol) <kT (0.2-0.8 kcal/mol) <<W (3-10 kcal/mol).

Based on these energy scales, the effect of the applied electric field is to slightly perturb the system so that the positions where the molecular dipole is aligned (counter-aligned) with the electric field are slightly lower (higher) in energy. This is in contrast to the driven regime, in which field-dipole interaction energy is on the order of the barrier to motion and thus the electric field causes the motion. In the work presented here, the dipole-electric field coupling serves only the highlight the *innate thermal motion*, which is present with or without the electric field.

In addition to the energies of the system there are two frequencies of importance: the frequency of the applied electric field (ω_E), and the frequency of the thermally activated hopping (ω_m). In our measurements, we set ω_E and tune ω_m by adjusting the temperature of the system. As the thermal energy of the system is increased the relation between these two frequencies will be in one of three regimes: $\omega_m < \omega_E$, $\omega_m \approx \omega_E$, and $\omega_m > \omega_E$. These three regimes will manifest themselves in both the capacitance and the dissipation factor of the sample. Figure 2.2 illustrates the general shape for both of these measurements.

At low temperatures, the molecules have little available thermal energy in comparison to size of the barrier to motion. In this case, the applied electric field is alternating mush faster than the thermally-activated hopping of the molecules (and associated reorientation of the dipoles) and as a result, the molecules do not contribute to either the capacitance or the

dissipation factor. At the other extreme, high temperatures, the molecules now have enough energy to change position at a rate comparable to that of the applied electric field frequency. In this regime, the molecules act as an almost ideal dielectric, and thus again do not contribute to the dissipation factor. However, as the molecules are now able to quickly respond to the field, they will contribute to the capacitance of the system. In between these two regimes, the molecular hopping rate and the rate of the alternating electric field will be similar, allowing the molecules to respond to the field, rather imperfectly. Because the response is imperfect, the capacitive current will vary from the ideal 90° phase shift from the voltage. In summary, we thus expect a step in capacitance and the corresponding peak in the dissipation factor to occur when the relaxation rate of the molecules equals the frequency of the applied electric field. This is, again, illustrated in Figure 2.2.

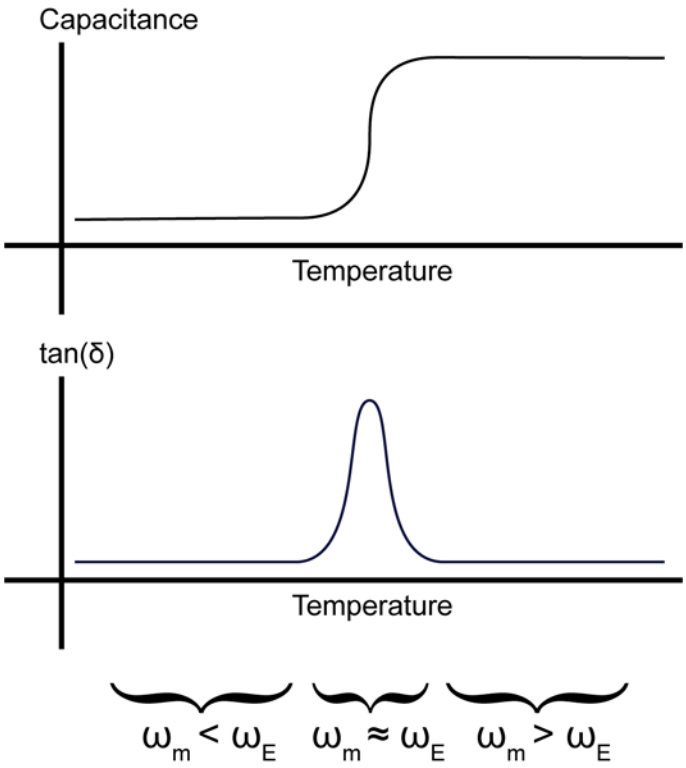

Figure 2.2: Illustration of capacitance and dissipation factor versus temperature

2.1- Equivalent circuit model

The simplest method of deriving the capacitance and dissipation factor is to solve an equivalent circuit, in which each of the circuit elements represents some characteristic of the real samples under measurement. In this case, all capacitive components (including that the substrate and the surrounding air or vacuum) other than the molecules are represented by one capacitor (C_0) and the molecules under measurement by a second capacitor C_m (the subscript m is to designate that this quantity represents the capacitance of the molecules of interest)

and a resistor R arranged in series together. This reflects both the charge storage (polarization) ability of the molecules (in C_m) and their dissipative nature (in R). In addition, RC is the characteristic response time for the molecular system. This molecular element pair is arranged in parallel with C_0, as both the molecules and the other elements of the capacitor (air, substrate) experience the same voltage drop. The circuit diagram is shown in Figure 2.3. Using Kirchhoff's laws two differential equations may be determined:

$$Q_0 = C_0 V \tag{2.1}$$

$$RC_m \frac{dQ_m}{dt} + Q_m = C_m V. \tag{2.2}$$

Combining the two equations results in

$$RC_m \frac{dQ_m}{dt} + Q_m + Q_0 = C_m V + C_0 V. \tag{2.3}$$

Rearranging of the equation and using $Q=Q_m+Q_0$ allows Eq. 2.3 to be written as

$$\tau \frac{dQ}{dt} = -Q + (C_m + C_0)V + \tau C_0 \frac{dV}{dt} \tag{2.4}$$

where $\tau = RC_m$. The solution to Eq. 2.4 may be found by substituting the complex voltage $V = V_i e^{-i\omega t}$ and complex charge $Q = Q_i e^{-i\omega t}$ and solving for the capacitance C=Q/V. The complex capacitance is then

$$C^* = \frac{C_0 + C_m - i\omega\tau C_0}{1 - i\omega\tau} = C_0 + \frac{C_m}{1 - i\omega\tau} \quad (2.5)$$

The real and imaginary parts of the capacitance are,

$$C' = C_0 + \frac{C_m}{1 + \omega^2\tau^2}$$
$$C'' = \frac{C_m\omega\tau}{1 + \omega^2\tau^2} \quad (2.6)$$

with the dissipation factor

$$\tan\delta = \frac{C''}{C'} = \frac{C_m}{C_0}\frac{\omega\tau}{1 + \omega^2\tau^2} \quad (2.7)$$

under the limit $C_m \ll C_0$. Equation 2.5, and subsequent forms derived there from, is known as the Debye equation. This derivation may be found in Daniel's Dielectric Relaxation [10].

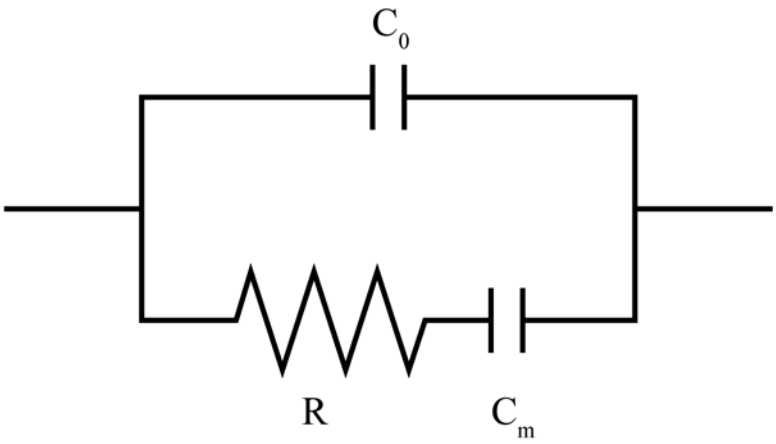

Figure 2.3: Equivalent circuit diagram. Here C_0 represents the capacitive components other than the molecules. The molecules are represented by the capacitor, resistor pair, C_m and R.

In our experimental set up, the observable quantities come from equations 2.6 (*C'*) and 2.7, and the limits of these equations can be examined in comparison to the general line shapes found in Figure 2.2. Beginning with the real part of the capacitance (top equation in 2.6), at low temperatures τ (which represents the average relaxation time of the molecules) will be large in comparison to $1/\omega$. This results in the C_m term being small and $C' \cong C_0$. Thus, the molecules are not contributing to the capacitance. As the temperature increases, τ will decrease and at some temperature $\omega\tau = 1$ and $C' \cong C_0 + \frac{C_m}{2}$. Further increases in the temperature result in τ continuing to decrease and $C' \cong C_0 + C_m$, resulting in the capacitance step seen in Figure 2.2. Using the same relations between ω and τ and examining equation 2.7 for tan(δ), at low temperatures $\tan\delta \cong \frac{C_m}{C_0}\frac{1}{\omega\tau}$ where $\frac{1}{\omega\tau}$ will be a small number. Thus tan(δ) is small or zero at low temperatures. Where $\omega\tau = 1$ the dissipation factor will be

$\tan(\delta) \cong \frac{C_m}{C_0}\frac{1}{2}$, and at high temperatures $\tan\delta \cong \frac{C_m}{C_0}\omega\tau$, with $\omega\tau$ being small in comparison to ½. Thus one advantage of the tan(δ) measurement is that it manifests a peak at $\omega\tau = 1$ surrounded by regions where tan(δ) is almost zero at high and low temperatures. As we shall see later, the presence of other relaxations and of ionic conductivity (which, if present, increases exponentially with temperature) complicate this simple picture. These limits are presented in Table 2.1. and correspond to the regions depicted in Figure 2.2.

Table 2.1: Approximations of the capacitance and dissipation factor for low, moderate, and high temperature regimes.

	Low Temperature $\tau \gg \omega$	Moderate Temperature $\omega\tau = 1$	High Temperature $\tau \ll \omega$
Real part of Capacitance $C' = C_0 + \frac{C_m}{1+\omega^2\tau^2}$	$C' \cong C_0$	$C' \cong C_0 + \frac{C_m}{2}$	$C' \cong C_0 + C_m$
Dissipation Factor $\tan\delta = \frac{C_m}{C_0}\frac{\omega\tau}{1+\omega^2\tau^2}$	$\tan\delta \cong \frac{C_m}{C_0}\frac{1}{\omega\tau}$	$\tan\delta \cong \frac{C_m}{C_0}\frac{1}{2}$	$\tan\delta \cong \frac{C_m}{C_0}\omega\tau$

2.2-Molecular Formulation of Debye Model

While the equivalent circuit model is useful and quickly arrives at the much relied upon Debye formula, it lacks any direct connection to molecular components. It is

advantageous, then, to derive the Debye equation from a molecular standpoint. Additional sources for the following derivation include Daniel's Dielectric Relaxation [10] and Frölich's Theory of Dielectrics [11]. The derivation begins with the static electric field of a capacitor in vacuum,

$$E = 4\pi\sigma_0, \tag{2.8}$$

where σ_0 is the charge density per area on the capacitor plates. If a dielectric is inserted into the capacitor, the charge is altered and now equal to

$$\sigma = \epsilon_m \sigma_0, \tag{2.9}$$

where ϵ_m is the dielectric constant (the subscript m is maintained from the previous derivation as experimentally the dielectric inserted is the molecules being measured). This leads to the displacement field

$$D = 4\pi\sigma = \epsilon_m E = E + 4\pi P \text{ where } P = \sigma - \sigma_0. \tag{2.10}$$

In the above equation *E* is the electric field and *P* is the polarization density (referred to as polarization for the remainder of this discussion). Using Eq. 2.10 the dielectric constant can be defined in terms of the polarization *P* resulting in

$$\epsilon_m - 1 = \frac{4\pi P}{E}. \tag{2.11}$$

Before examining the time dependence it is prudent to further examine Eq. 2.11 and distinguish between types of polarizations. Possible polarizations to consider may be classified into the following groups: electronic, ionic, and motion of permanent dipoles. Electronic polarization is the displacement of the electrons in an atom and typically occurs at frequencies (> 10^{12} Hz) far above those typically utilized in electrical measurements. Our measurements are in the 100 Hz to 20 kHz range. Ionic polarization is found in ion containing materials which under the influence of an electric field will displace the ion position resulting in a net polarization for the material. This process is much slower than electronic polarization. The motion of permanent dipoles is the type of polarization studied in this thesis and is a result of the reorientation of permanent dipoles in a material. As electronic polarization can always be present and assuming that all materials of interest will also contain permanent dipoles (though excluding ionic polarization) Eq. 2.11 may be rewritten as

$$\epsilon_m - 1 = \frac{4\pi}{E}(P_D + P_\infty) \text{ with } \epsilon_\infty - 1 = \frac{4\pi P_\infty}{E}. \quad (2.12)$$

In the above equation P_D is the dipolar polarization and P_∞ the electronic or optical polarization.

The response of a material system to a time dependent electric field can be determined by assuming that the rate by which the time dependent polarization approaches equilibrium is proportional to the distance from equilibrium, resulting in

$$\tau \frac{dP(t)}{dt} = P_{static} - P(t) \qquad (2.13)$$

This is a standard assumption for any process relaxing towards equilibrium, and is derived from the physical argument in the next paragraph. Applying Eq. 2.13 to the dipolar polarization gives

$$\tau \frac{dP_D}{dt} + P_D(t) = (\epsilon_m - \epsilon_\infty) \frac{E(t)}{4\pi} \qquad (2.14)$$

For a periodic electric field (using Eq. 2.12) the solution to Eq. 2.14 is

$$P_D = Ke^{-\frac{1}{\tau}} + \frac{1}{4\pi} \frac{\epsilon_m - \epsilon_\infty}{1 + i\omega\tau} E_0 e^{i\omega t}, \qquad (2.15)$$

with *K* being an initial polarization if present. Thus, the polarization at any given time consists of the initial polarization, which will be scrambled after an average time τ, and the 2nd term which reflects the response to the applied electric field. The 1st term in Eq. 2.15 decays with time and for an alternating electric field may be reasonably dropped to focus on the 2nd term only. For this case the complex dielectric constant is defined as

$$\epsilon^* - \epsilon_\infty = 4\pi \frac{P_D^*}{E^*} = \frac{\epsilon_m - \epsilon_\infty}{1 + i\omega\tau} \tag{2.16}$$

Separating Eq. 2.16 into the real and imaginary components result in

$$\begin{aligned} \epsilon' &= \epsilon_\infty + \frac{\epsilon_m - \epsilon_\infty}{1 + \omega^2\tau^2} \\ \epsilon'' &= (\epsilon_m - \epsilon_\infty)\frac{\omega\tau}{1 + \omega^2\tau^2} \end{aligned} . \tag{2.17}$$

The dissipation factor may be defined in terms of the dielectric constant as

$$\tan\delta = \frac{C''}{C'} = \frac{\chi''}{\chi'} = \frac{\epsilon''}{\epsilon'} = \frac{(\epsilon_m - \epsilon_\infty)\omega\tau}{\epsilon_m + \epsilon_\infty\omega^2\tau^2}, \tag{2.18}$$

obtaining the same form as Eq. 2.7.

Physically, we can understand these results as follow. In the molecular derivation above, the relaxation time τ, which represents the observable response time of the entire system, can be connected to our previous model of molecular groups hopping between wells on a potential surface. Consider a collection of molecules, *N*, each constrained by a double potential well with locations 1 and 2 (Figure 2.1). Microscopically these molecules are affected by thermal fluctuations from the local environment. As such, the molecule will on occasion have sufficient energy to overcome the barrier from location 1 to location 2 and vice versa, resulting in a change in direction of the molecule's dipole. This hopping or

transition rate can be quantified via transition-state theory (TST), which examines rates for any physical system where two stable equilibriums are separated by a potential barrier, which can be overcome via thermal fluctuations. For instance, one well could represent the energy of the reactants and the other the energy of the products for a chemical reaction. Though TST was developed, using statistical mechanics, to, in part, examine the rates of chemical reactions, these rates can be successfully applied to other transitional processes where a free energy barrier exists, such as molecular hopping between wells.

The rate equation developed by Eyring [12],

$$k = \frac{k_b T}{h} \exp\left(-\frac{\Delta G^{\ddagger}}{RT}\right), \tag{2.19}$$

will serve as the basis for the rate equation used in this work. In the Eyring equation k is the rate of the process, k_b is the Boltzmann constant, h is Plank's constant, T the temperature, R the gas constant, and $\Delta G^{\ddagger}$ is the Gibbs free energy of activation; where $\Delta G^{\ddagger} = \Delta H - T\Delta S = \Delta E + p\Delta V - T\Delta S$ with ΔE the change in internal energy, ΔV the change in volume, and ΔS the change in entropy. In applying Eq. 2.19 to molecular reorientation some simplifications can be made. First the linear temperature dependence in the pre-factor, $\frac{k_b T}{h}$, will not be as significant over our experimental range (10K-400K) as the dependence in the exponential term; an order of magnitude difference in the pre-factor vs. tens to hundreds of orders of magnitudes for the exponential term. For this reason the pre-factor will be approximated as a

temperature independent constant, ω_0. This is a common approximation. Secondly, the exponential term can be simplified by examining the Gibbs free energy. For our physical system the two wells represent a molecule which has reoriented by 180°. Whereas in a chemical reaction, the volume could change dramatically, due to a phase change, volume changes will be minimal for a simple molecular reorientation. Similarly, for a chemical reaction, the total entropy of the system can also be significantly altered (again by phase transitions) or due to the change in the number of species (two small molecules becoming a larger molecule). There should be no change in entropy, however, for a randomly reorienting system of molecules. (Providing that the molecules are non-interacting as we have assumed here. We discuss this issue later in Section 2.3.) For these reasons $\Delta G^{\ddagger} \cong \Delta E$, and in subsequent equations ΔE will be referred to as W relating to the previous notation for the barrier to motion. Making the approximations to Eq. 2.19 results in the Arrhenius equation

$$\frac{1}{\tau} = \omega_0 \exp\left(-\frac{W}{k_b T}\right), \tag{2.20}$$

where W is the potential barrier, k_b the Boltzmann constant, T the temperature, and ω_0 is the attempt frequency. The attempt frequency represents the motion of the molecule near the potential minima and can be considered rate of tries or “attempts” being made to overcome the potential barrier. In the harmonic oscillator approximation, this is the oscillation frequency near the bottom of the potential well.

Eq. 2.20 must be modified to account for the applied electric field, which is not necessarily in the direction of the dipole, and also to account for any innate asymmetry of the two potential that may exist. For the moment, we assume a single dipole with a well-defined angle to the field. The hopping rates are now

$$1/\tau_{12} = \omega_0 \exp\left(\frac{-W + \frac{B}{2} - pE\cos\theta}{kT}\right)$$
$$1/\tau_{21} = \omega_0 \exp\left(\frac{-W - \frac{B}{2} + pE\cos\theta}{kT}\right) \quad (2.21)$$

where θ is the angle between the electric field E and the dipole moment p and B is an intrinsic asymmetry (if present) between the two potential wells. $1/\tau_{ij}$ is the rate of hopping from well i to well j. From a master equation approach, the change in the number of dipoles in well 1 will consist of the dipoles transitioning from well 2 to 1 minus those transitioning from well 1 to 2:

$$\frac{dN_1}{dt} = -N_1/\tau_{12} + N_2/\tau_{21}. \quad (2.22)$$

In addition,

$$\frac{dN_1}{dt} = -\frac{dN_2}{dt} \quad (2.23)$$

because $\frac{dN}{dt} = 0$ where $N = N_1 + N_2$. Equivalently,

$$N_1/\tau_{12} = N_2/\tau_{21} \text{ with } N_1 + N_2 = N. \quad (2.24)$$

Eq. 2.23 and Eq. 2.24 give the result

$$\frac{d(N_1 - N_2)}{dt} = 2\frac{dN_1}{dt}. \quad (2.25)$$

The quantity N_1-N_2 is important because it is related to the polarization. The definition of the polarization is $P = (\eta_1 - \eta_2)p\cos(\theta)$, where $p\cos(\theta)$ is the projection of the dipole along (or against) the electric field and η_1-η_2 counts the net number of dipoles per volume along the field (as the polarization is a per volume quantity, η is used in place of N which was defined as the number of dipoles, not the number per volume). Using Eq. 2.22, and this definition, Eq. 2.25 can be rewritten as

$$\frac{1}{2p\cos(\theta)}\frac{dP}{dt} = -\frac{\eta_1}{\tau_{12}} + \frac{\eta_2}{\tau_{21}}. \quad (2.26)$$

As a reminder, the relaxation time of the entire system's polarization, τ, is a combination of the τ_{ij} hopping rates. It is this relationship that will first be examined. To do so Eq. 2.26 must be manipulated into the form of Eq. 2.13 in order to identify the system relaxation time, τ, in terms of the molecular hopping rates. For the moment the full forms of

the hopping rates will not be introduced so as to make the derivation easier to read and follow. Proceeding from Eq. 2.26, and using the relationship $\eta=\eta_1+\eta_2$ results in

$$\begin{aligned}\frac{1}{2p\cos(\theta)}\frac{dP}{dt} &= -(\eta-\eta_2)\left(\frac{1}{\tau_{12}}\right)+\eta_2\left(\frac{1}{\tau_{21}}\right).\\ \frac{1}{2p\cos(\theta)}\frac{dP}{dt} &= -\eta_1\left(\frac{1}{\tau_{12}}\right)+(\eta-\eta_1)\left(\frac{1}{\tau_{21}}\right).\end{aligned} \tag{2.27}$$

Again for clarity, the $1/\tau_{ij}$ terms will be replaced by ω_{ij} and care should be taken to not confuse these terms with the electric field frequency ω which will be later introduced into these equations. Continuing by adding the two above equations

$$\frac{1}{p\cos(\theta)}\frac{dP}{dt} = \eta(\omega_{21}-\omega_{12})+(\omega_{21}+\omega_{12})(\eta_2-\eta_1), \tag{2.28}$$

and dividing by the sum of the hopping rates so the polarization term may be recovered on the right hand side of the equation results in

$$\frac{1}{p\cos(\theta)}\frac{1}{\omega_{21}+\omega_{12}}\frac{dP}{dt} = \frac{\eta(\omega_{21}-\omega_{12})}{\omega_{21}+\omega_{12}}-\frac{(\eta_1-\eta_2)(\omega_{21}+\omega_{12})}{\omega_{21}+\omega_{12}}. \tag{2.29}$$

Multiplying by the dipole component we arrive at

$$\frac{1}{\omega_{21}+\omega_{12}}\frac{dP}{dt} = p\cos(\theta)\frac{\eta(\omega_{21}-\omega_{12})}{\omega_{21}+\omega_{12}}-P. \tag{2.30}$$

Comparison with Eq. 2.13 shows the relaxation time for the system to be $\tau = \frac{1}{\omega_{21}+\omega_{12}}$, and the static polarization to be $p\cos(\theta)\frac{\eta(\omega_{21}-\omega_{12})}{\omega_{21}+\omega_{12}}$.

The static polarization will be addressed shortly, but we first examine the relaxation time by substituting the full forms of the hopping frequencies,

$$\tau = \frac{1}{\omega_0 \exp\left(\frac{-W+\frac{B}{2}-pE\cos\theta}{kT}\right)+\omega_0 \exp\left(\frac{-W-\frac{B}{2}+pE\cos\theta}{kT}\right)}. \quad (2.31)$$

With factoring common terms,

$$\tau = \frac{1}{\omega_0 \exp\left(-\frac{W}{kT}\right)}\frac{1}{\exp\left(\frac{\frac{B}{2}-pE\cos\theta}{kT}\right)+\exp\left(\frac{-\frac{B}{2}+pE\cos\theta}{kT}\right)}. \quad (2.32)$$

Before proceeding to derive the polarization it is important to examine the system relaxation time. As mentioned, Eq. 2.32 is the observable relaxation time of the system which is related to the molecular hopping rates. This is an important distinction as τ is the direct observable, not the molecular hopping rates (though, as will be shown, in most experimental cases they will be close), and as such the above sentence and Eq. 2.32 merits further scrutiny.

We first examine the case where the hopping rates between the two wells are equal ($\tau_{12}=\tau_{21}=\tau_0$) by setting $B=0$ and $E=0$ resulting in

$$\tau = \frac{1}{2\omega_0 \exp\left(-\frac{W}{kT}\right)} = \frac{\tau_h}{2}. \qquad (2.33)$$

Again, τ is the relaxation time of the system and τ_h is the hopping time. In this case, the relaxation time is one half of the hopping time, which is now equal to the Arrhenius equation (Eq. 2.20). This would be the experimentally observed relaxation time for the system's polarization upon application of an electric field.

This relaxation time of the system (the response of the whole system to a stimulus) is equal to the hopping time of the individual molecules (within a factor of two), which makes sense because it is only through reorientation of individual molecules that the system can respond to the stimulus. Note that earlier, in discussing polarization mechanisms, we assume that the molecules cannot move and that no ions are present, which is consistent with our experimental systems. Thus the only possible response to an electric field is electronic polarization (which we have factored out) and dipolar reorientation. In this derivation, the stimulus is the application of an electric field, and thus the response is a polarization. However, such a connection between τ and hopping rates will hold for any characteristic response that arises from a difference in the population of the two potential wells.

If we now release the constraint that the electric field is zero (still leaving the innate asymmetry aside)

$$\tau = \frac{1}{\omega_0 \exp\left(-\frac{W}{kT}\right)} \frac{1}{\exp\left(\frac{-pE\cos\theta}{kT}\right) + \exp\left(\frac{+pE\cos\theta}{kT}\right)}. \quad (2.34)$$

As is the case for our experiments, we can consider that $pE\cos(\theta) \ll kT$ and the relaxation time can be approximated as

$$\tau \cong \frac{1}{\omega_0 \exp\left(-\frac{W}{kT}\right)} \frac{1}{2}. \quad (2.35)$$

The ½ is a result of a Taylor series expansion of the *E* dependent term about zero. In this approximation we have recovered the same relaxation time as when the electric field is equal to zero. This indicates that to the first order, our electric field does not influence the hopping rate of the molecules. In this sense it is a non-perturbative probe of the innate dynamics of the system enabling (through the generation of an experimentally measureable, but very small polarization) detection of the dynamics of the system without altering them. Note that this would not be true if *pE* was a larger quantity; in particular if *pE* were large enough (similar to *W*), the electric field would first perturb and then dominate the dynamics of the system.

Next, setting *E=0* we can examine the asymmetry term with

$$\tau = \frac{1}{\omega_0 \exp\left(-\frac{W}{kT}\right)} \frac{1}{\exp\left(\frac{-B}{2kT}\right) + \exp\left(\frac{+B}{2kT}\right)}. \quad (2.36)$$

This equation can also be written as $1/(\omega_{12} + \omega_{21})$. For any significant *B* (larger than a few *kT*) it is obvious that ω_{12} will not be close to ω_{21}. Thus hopping out of the higher energy well, which now has a reduced barrier, will be much faster than hopping out of the lower energy well, which now has an enhanced barrier. The *B* containing terms in Eq. 2.36 can be expressed as $\operatorname{sech}\left(\frac{B}{2kT}\right)$ which affects the total observable polarization as discussed below. The illustration in Figure 2.4 shows a potential with a large asymmetry and in this case the hopping from 1 to 2 will be much slower than from 2 to 1. In the situation where *B=2W* (a very extreme case) the relaxation time of the system is now

$$\tau = \frac{1}{\omega_0 \left(\exp\left(-\frac{2W}{kT}\right) + 1\right)}. \quad (2.37)$$

Comparison with Eq. 2.34, where *B=0* and *E=0*, results in $\tau_{B=2W} < \tau_{B=0}$. This means that the dynamics are significantly faster (lower τ values) when asymmetry is present, reflecting the lower effective barrier (hopping from the higher energy well). In the regime where the two wells differ significantly in energy, $\tau = \frac{1}{\omega_{21}+\omega_{12}}$ becomes $\tau = 1/\omega_{fast}$ where $1/\omega_{fast}$ is the highest rate hopping process. The system is dominated by the fastest hopping.

It is important to note that as the asymmetry between the wells increases, the hopping rate from the lower well becomes much slower than the hopping to the lower from the upper. In other words, the population tends to pool in the lower energy well. This is consistent with Boltzmann statistics. If a perturbation pushes additional population in to the higher well, the system will relax quickly from the much higher energy state. From an experimental perspective, such significant well asymmetry dramatically decreases the magnitude of the polarization (discussed in detail on pg. 32). Thus, as the well asymmetry increases the molecules become non-responsive and the ability to observe the dynamics experimentally is lost.

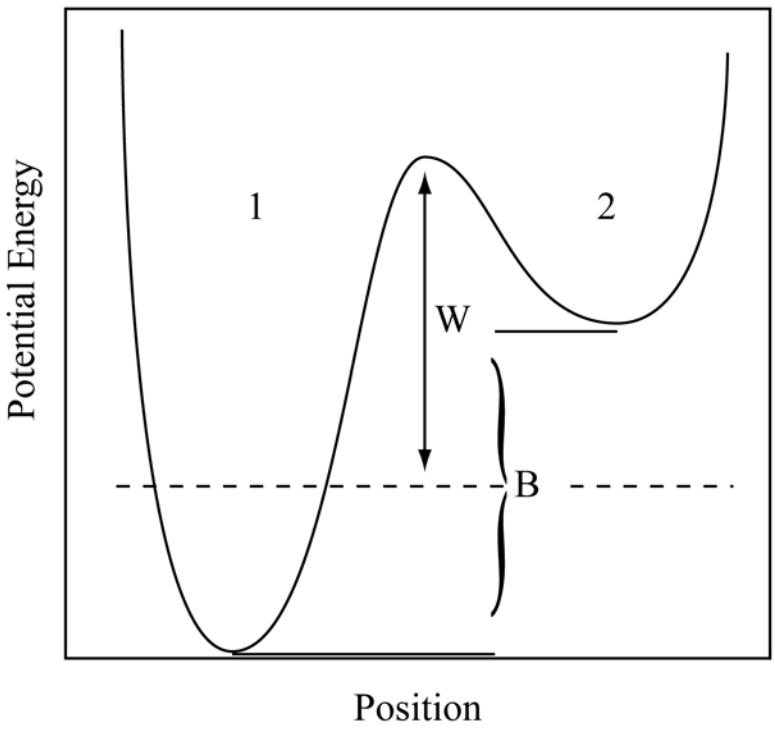

Figure 2.4: Illustration of the double potential well with a high asymmetry (B=W for this illustration).

To quantify the effects discussed above we will further examine the polarization and beginning from Eq. 2.30

$$P = p\cos(\theta)\frac{\eta(\omega_{21} - \omega_{12})}{\omega_{21} + \omega_{12}} = \eta p\cos(\theta)\tanh\left(\frac{\frac{B}{2} - p\cos(\theta)E}{kT}\right) \quad (2.38)$$

The hyperbolic tangent in the above equation serves to represent an important physical result. For simplicity, if B=0 then $P = \eta p\cos(\theta)\tanh\left(\frac{-p\cos(\theta)E}{kT}\right)$. As the strength of the electric field increases so will the polarization. At small values of E/kT (approximation shown below) the response in the polarization will be linear to an increase in the electric field. However, if E becomes very large the polarization saturates and $P = \eta\cos(\theta)$. At this point, all dipoles are generally aligned with the field and thus further field increases result in little increase in polarization. In our work, we are far from this limit; in this case, pE would be large. That is, the electric field would no longer be probing the dynamics of the system, but instead driving them. The pE/kT term in hyperbolic tangent term is worth discussion. Random thermal motion (as quantified by kT) will generally fight against the alignment of the dipole with the electric field. Thus as kT increases the maximum possible polarization decreases. In the saturation regime, as pE increases, the polarization increases slightly as the quantity pE/kT further increases. In the linear regime, discussed below, this term pE/nkT, where n is a numerical factor, depending on the dimensionality of the system, is referred to as the Curie factor, from its first use in paramagnetic system (rather than the paraelectric system under study here).

Applying the approximation that $pE\cos(\theta) \ll kT$ results in

$$P = \eta p\cos(\theta)\left(\tanh\left(\frac{B}{2kT}\right) - \frac{p\cos(\theta)E}{kT}\,\mathrm{sech}^2\left(\frac{B}{2kT}\right)\right). \qquad (2.39)$$

The *cos(θ)* term was first introduced with the assumption of all dipoles in the system having the same angle to (or 180° from) the electric field. This is not consistent with our experimental system where the molecules are randomly oriented with respect to the field. These terms would be important for an ordered dipolar system, such as a ferroelectric. If this constraint is released and dipoles can be in any orientation (uniformly distributed), an average polarization in the direction of the electric field can be calculated by averaging over the solid angle (*sin(θ)dθdφ*). Before altering Eq. 2.39 the two terms should be examined. The hyperbolic tangent represents a non-responsive (to the electric field) term due to the innate asymmetry in the potential. This will go away after averaging, since each of these preferred dipolar positions is in a random direction and thus it leads to no net polarization. The second term will remain present and is the dipolar response to the applied field. In this second term there is a hyperbolic secant factor of the potential asymmetry. As the asymmetry increases it serves to reduce this second term and thus the polarization, as discussed in the previous paragraph. While this second term is being reduced the first non-responsive term gets larger, however as stated this goes away upon angular averaging. After averaging over orientation, the polarization is

$$P = \frac{\eta p^2 E}{3kT}\operatorname{sech}^2\left(\frac{B}{2kT}\right). \quad (2.40)$$

The factor *pE/3kT* introduced in this approximation is known as the Curie factor, as discussed above.

One more correction needs to be made before solving Eq. 2.30. As a final detail, we can also consider that the electric field experienced by the dipoles will be screened by the surrounding material. This is a classical correction. Consider the electric field in the space between dipoles as

$$E_i = E + \frac{4\pi}{3}P, \tag{2.41}$$

where E is the applied electric field and $\frac{4\pi}{3}P$ is contribution from the local field for a spherical volume around a dipole.

Now defining $P_s = P_D + P_\infty = (\alpha_D + \alpha_\infty)E_i$ where α_D and α_∞ are the dipolar and optical polarizabilities respectfully, and using Eq. 2.12,

$$\frac{\epsilon_m - 1}{\epsilon_m + 2} = \frac{4\pi}{3}(\alpha_D + \alpha_\infty). \tag{2.42}$$

Rearranging the above equation results in

$$\epsilon_m - 1 = \frac{\epsilon_m + 2}{3}\ 4\pi\frac{P_s}{E_i}, \tag{2.43}$$

which is equivalent to Eq. 2.11 for the modified electric field by a factor of $\frac{\epsilon_m+2}{3}$. This factor can then be brought into equation 2.30 as

$$\tau\frac{dP}{dt}=\frac{\epsilon_m+2}{3}\frac{\eta p^2 E}{3kT}\operatorname{sech}^2\left(\frac{B}{2kT}\right)-P, \tag{2.44}$$

Where the derived static polarization 2.40 has been included with the factor from 2.43 and again τ is the system relaxation rate and P is the polarization.

Following the same derivation from Eq. 2.11 with an alternating electric field the complex dielectric constant is

$$\epsilon^*=\frac{\epsilon_m+2}{3}\frac{\eta p^2 E}{3kT}\operatorname{sech}^2\left(\frac{B}{2kT}\right)\frac{1}{1+i\omega\tau}+\epsilon_\infty, \tag{2.45}$$

recalling that ε_m is the dielectric constant with the optical component represented by

ε_∞. As well, ω is the frequency of the applied field and τ is the relaxation time of the system. To relate back to the equivalent circuit derivation the real and imaginary parts are put in terms of the capacitance as,

$$\begin{aligned} C' &= C_0+\frac{\epsilon_m+2}{3}\frac{\eta p^2 E}{3kT}\operatorname{sech}^2\left(\frac{B}{2kT}\right)\frac{1}{1+\omega^2\tau^2} \\ C'' &= \frac{\epsilon_m+2}{3}\frac{\eta p^2 E}{3kT}\operatorname{sech}^2\left(\frac{B}{2kT}\right)\frac{\omega\tau}{1+\omega^2\tau^2} \end{aligned} \tag{2.46}$$

which is equivalent to 2.6 with

$$C_m = \frac{\epsilon_r + 2}{3}\frac{\eta p^2 E}{3kT}\ \mathrm{sech}^2\left(\frac{B}{2kT}\right). \quad (2.47)$$

When analyzing data Eq. 2.47 is a primary tool. To review, the first fraction reflects the screening of the electric field by the surrounding dipoles, which is derived for a three-dimensional system, where each dipole is surrounded by other dipoles. This term is generally less important in two-dimensional systems. The second term includes the number density of molecules (η) and the size of the dipole moment (p), each of which should increase C_m. In addition, the second fraction includes the term *pE/3kT*, which resulted from approximating the hyperbolic tangent to the limit $pE \ll kT$. This is the Curie factor discussed above, and reflects the balance between random thermal motion and the tendency of the dipole to align with the electric field. Finally the last fraction reflects the suppression of polarization when the innate well asymmetry is present. In this case, the molecules are less likely to respond to the electric field (or alternatively, return to equilibrium very quickly). As before the dissipation factor can now be calculated to be

$$\tan\delta = \frac{1}{C_0}\frac{\epsilon_r + 2}{3}\frac{\eta p^2 E}{3kT}\ \mathrm{sech}^2\left(\frac{B}{2kT}\right)\frac{\omega\tau}{1+\omega^2\tau^2} = \frac{C_m}{C_0}\frac{\omega\tau}{1+\omega^2\tau^2}. \quad (2.48)$$

2.3- Non-Arrhenius Dynamics

Thus far in our discussion we have assumed known barriers on a known potential surface, and determined relaxation rates from these quantities. However, this is exactly the opposite of the experimental procedure, whereby experimentally observed rates ($1/\tau$) must be extrapolated to determine parameters of the potential, such as barriers. In experimental practice, the Arrhenius equation (Eq. 2.17) is the most frequently used relaxation rate and works well for systems in which interactions are small. None of the theory above dealt with the more complex case where the motion of neighboring dipoles are correlated by some type of interaction. If interactions are significant, a rate equation other than Arrhenius (and so the temperature dependence) should be chosen. Failure to do so will result in an erroneous interpretation of the parameters present in the rate equation. This section will introduce two additional rate equations that better describe interacting systems as well as an introduction to the community's standard presentation of relaxation rate data. The later is done in an effort to better illustrate the differences in different rate equation and to prepare the reader for data presented later in this thesis and the body of literature related to dielectric spectroscopy should they undertake further investigation.

Before an alternative to the Arrhenius equation is used one must decide if an alternative should be used. The attempt frequency, ω_0, holds an important place as a heuristic determination of the presence or absence of interacting effects and as such its value can be used as a good initial indicator for which rate equation or group of equations might be best

applied. In other words, as discussed below, it is experimentally useful to compare the observed attempt frequency to known values. Previous discussion of the relaxation rate as derived by Eyring resulted in an attempt frequency of

$$\omega_0 = \frac{k_b T}{h} \qquad (2.49)$$

with temperature T, Boltzmann factor k_b, and Plank's constant h. A thorough derivation of the Eyring equation can be found in his 1935 publication [5]. Using statistical mechanics and including translational, vibrational, and rotational degrees of freedom, Eyring examined the general form of the relaxation rate as well as rates for example situations. In all cases, part of a normal coordinate velocity term is present as a multiplicative factor, namely k_bT/h, regardless of the system for which the rate was calculated. As mentioned, the linear temperature dependence in the pre-factor is typically not applied to dielectric spectroscopy and ω_0 is approximated to be $1x10^{14}$ rad/sec. As a reference $\frac{k_b(100K)}{h} \sim 2 \times 10^{12}$ rad/sec. The attempt frequency can also be calculated in other ways, for instance, by using the harmonic oscillator approximation and determining an effective spring constant for a particular potential surface. In this case, $\omega_0 = \sqrt{(k/I)}$ where k is the effective rate constant. Regardless of the calculation, ω_0 falls in the range of 10^{11} to 10^{14} rad/sec. This result can be interpreted as a limit on how fast a molecular group can reorient due to thermally activated hopping. For instance, in examining the Arrhenius equation, at the highest possible temperatures $\omega=\omega_0$.

This is an important result in that analysis resulting in attempt frequencies that deviate (particularly that are higher) from the expected and correct attempt frequency should not be mistakenly interpreted as a physical increase in the attempt frequency. Rather some other interpretation should be applied to recover the correct attempt frequency. For example, no molecule can have an attempt frequency of say, 10^{60} rad/sec. When this is observed, some "intervention" must occur; either a determination that the rate equation under use in inappropriate (and replacement with a more appropriate form) or an interpretation of the observed attempt frequency as resulting from multiple effects. Below, we discuss situations in which unphysical apparent attempt frequencies are observed, and then two "interventions" that help to correctly interpret these results.

The Vogel-Fulcher-Tammann (VFT) equation [13--15] was developed to characterize cooperative relaxations associated with a glass transition. The VFT equation is

$$\frac{1}{\tau} = \omega_0 \exp\left(-\frac{B}{T - T_0}\right); \ln(\frac{1}{\tau}) = \ln(\omega_0) - \frac{B}{T - T_0}, \quad (2.50)$$

where T_0 is a reference temperature and B is an activation energy. T_0 is a critical temperature, below which the free volume is approximately zero [16]. With the reference temperature and activation energy the glass transition temperature, T_g, can be calculated by extrapolating the VFT equation to τ = 100 seconds [17]. Additionally, glasses are often classified by their fragility which is quantified by the steepness index m and can be calculated once T_g is found as [18]

$$m = \left.\frac{d(\log(\tau))}{d(T_g/T)}\right|_{T_g=T}. \qquad (2.51)$$

In general, *m* increases with the level of cooperativity. The primary difference between the Arrhenius and VFT forms is that the barrier for the VFT changes as the temperature is altered. This means that as the temperature is lowered, dynamics will slow more dramatically because not only is the thermal energy decreasing, at the same time the barrier is increasing. This enhanced barrier to motion reflects the growing constraint on the rotating entity as interactions increase. In fitting with the VFT form, the attempt frequency (~$1x10^{14}$ rad/sec) is assumed leaving *B* and T_0 as parameters to be determined.

Now let us examine how the VFT form compares to the Arrhenius rate and discuss under what circumstances it may be properly applied. Figure 2.5 is an Arrhenius plot of example data generated using the Arrhenius and VFT rate equations. Relaxation rate data are typically plotted in the Arrhenius form; the natural log of the relaxation rate, *ln(ω)*, against inverse temperatue *(1/T)*. For our experiments, the applied electric field frequency (ω) is equal to the inverse of the system relaxation rate ($1/\tau$) when there is a peak in the dissipation factor, that is, $\omega\tau=1$. This relation results in the Arrhenius equation producing a straight line the VFT will have some amount of curvature. Experimentally our frequency range is limited to the approximate area of the grey shaded box in Figure 2.5. In this frequency range, the ability to distinguish between a linear plot and one with some amount of curvature is

reduced. However, if a linear fit is inappropriately applied (see the dashed line in Figure 2.5) the result will be one of a high attempt frequency. Additionally, the activation energy from the erroneous linear fit in Figure 2.6 will be raised. This is an indication that the linear or Arrhenius relationship is not accurately describing the relaxation and an alternative such as VFT should be used.

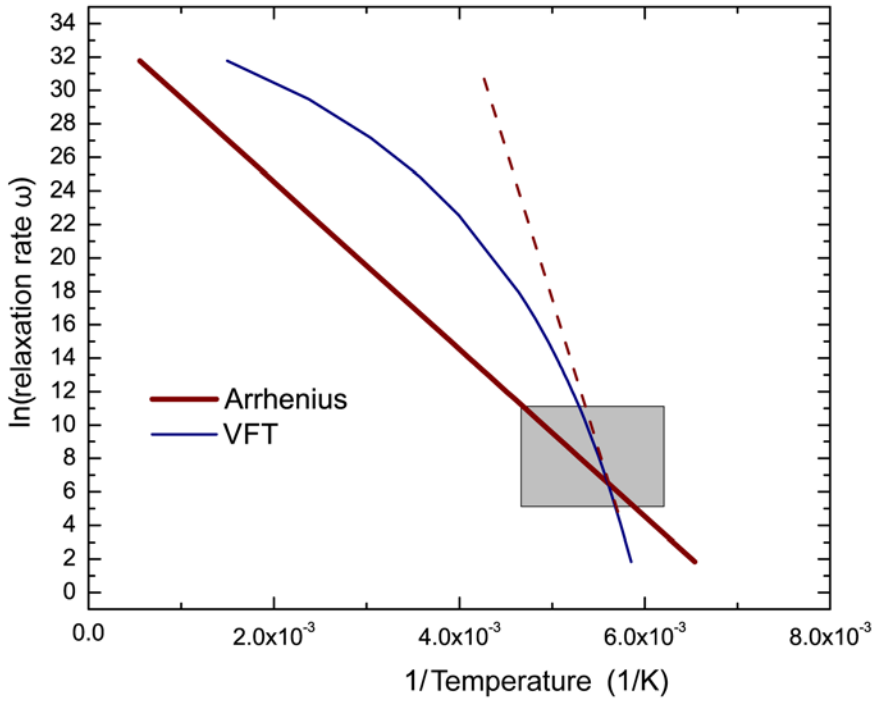

Figure 2.5: Plot of Arrhenius and VFT curves. The dashed line is an Arrhenius fitting of VFT type curve in our experimental range. The height of the grey box indicates the frequency range experimentally available.

The VFT equation was developed for, and is most applicable to, characterizing relaxations associated with the glass transition; however, there are non-glassy yet still interacting systems. In such a case, the Arrhenius form can also be used (albeit in a heuristic way) to characterize interacting systems. Starkweather [19] related the Arrhenius, $\omega = A\exp\left(-\frac{E_a}{RT}\right)$, and Eyring, $\omega = \frac{kT}{h}\exp\left(-\frac{\Delta H}{RT}\right)\exp\left(\frac{\Delta S}{R}\right)$, equations, and compared them with experimental data on a wide variety of systems. Earlier it was stated that the in the absence of a change in entropy the Eyring equation reduced to the Arrhenius equation. Starkweather expounded on this idea by equating the two equations even with an entropy change. Consequently, Starkweather was able to derive an expression for the activation energy for a relaxation occurring at a specific temperature and frequency,

$$E_a = RT\left[1 + \ln\left(\frac{k}{h}\right) + \ln\left(\frac{T}{\omega}\right)\right] + T\Delta S. \qquad (2.52)$$

The first term in the above equation is only dependent on the temperature and frequency of an observed relaxation and as such should always be present. From Eq. 2.52 we see that for any positive change in entropy the activation energy also increases. That is, when $\Delta S=0$, Eq. 2.52 represents an effective minimum in the activation energy. Essentially this equation connects the temperature where a relaxation is measured and the resultant barrier obtained from a simple Arrhenius fit, with again ω_0=kT/h. As a reminder S is the difference in entropy between the two states represented by the two potential well in Figure 2.1. Starkweather's

interpretation is that comparison of experimentally measured activation energies to this minimum can give insight as to the type of motion taking place. In particular, Starkweather characterized relaxations resulting in activation energies equal or close to the minimum as non-cooperative, an example being reorientation of methyl groups. In this case, as discussed above, ΔS should be =0, as these are local motions with no significant interactions with neighboring molecules. Relating to the discussion above, in these non-interacting systems, the application of the Arrhenius equation is appropriate, and the attempt frequency is physical. For cooperative motion, of which glass transitions are a large subset, the change in entropy is no longer equal to zero. Returning to the rate equation we have

$$\frac{1}{\tau} = \omega_0 \exp\left(\frac{-\Delta H + T\Delta S}{kT}\right) \qquad (2.53)$$

where ω_0 is the attempt frequency, -ΔH+ΔS is the free energy of activation, and to keep with previous forms of the rate equations the Boltzmann constant, k, is used. Expanding the exponential gives,

$$\frac{1}{\tau} = \omega_0 \exp\left(\frac{\Delta S}{k}\right) \exp\left(\frac{-\Delta H}{kT}\right). \qquad (2.54)$$

The entropy term in the above equation is not temperature dependent, resulting in an observed activation energy and attempt frequency (combining the first two terms) that is

artificially high. Remember these are quantities calculated from the experimental data typically from an Arrhenius plot with, in this case,

$$\ln(\omega) = \ln(\omega_0) + \frac{\Delta S}{k} - \frac{\Delta H}{kT}. \quad (2.55)$$

The slope of such a plot no longer corresponds to the physical activation energy (as it will now be too large without the entropy term) and the intercept now includes the entropy term resulting in an unphysical high attempt frequency.

Chapter 3-Experimental Methods and Apparatus

Chapter 3 of this thesis examines the experimental methods and apparatus utilized in this research as well as a description of the two molecular systems measured. As mentioned, with dielectric spectroscopy the materials of interest are inserted as the dielectric in some type of capacitor. Section 3.1 describes the electrode configuration, or capacitor, that we utilized for all dielectric measurements presented. Both the electrode geometry and production procedure are discussed. This is followed by a description of the experimental systems utilized. Section 3.3 presents the molecular systems measured as well as the general growth procedure for the self-assembled monolayers. The last section, 3.4, briefly introduces techniques used to characterize certain aspects of the self-assembled monolayers, such as thickness.

3.1- Interdigitated Electrodes

Dielectric measurements of all samples were performed using an interdigitated electrode (IDE) configuration. IDEs are capacitors that are co-planar to the substrate so that the direction of the electric field between the capacitor plates is parallel to the surface, as opposed to perpendicular as in the case of a “sandwich” type electrode (Figure 3.1). Additionally, allows for a long meander path, path along the capacitor “plates” (see Figure 3.1), in a small area.

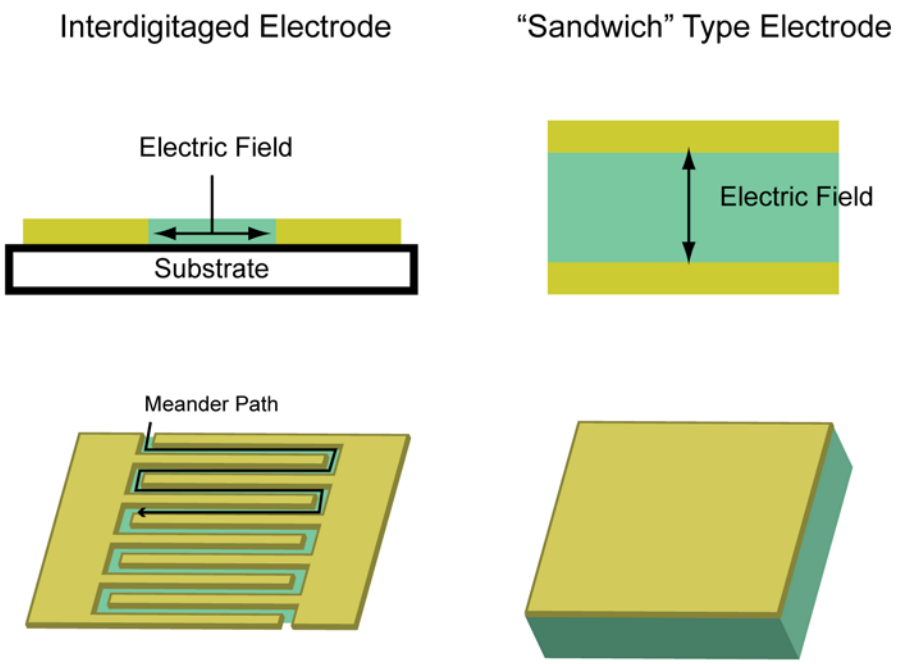

Figure 3.1: Illustrations of an interdigitated electrode (bottom left) and a parallel plate or “sandwich” electrode (bottom right). Additionally, side views of an interdigitated electrode (top left) and sandwich electrode (top right) with a double arrow indicated the direction of the electric field.

There are both advantages and disadvantages to this type of electrode configuration. The main advantage is that an IDE allows dielectric measurements of extremely small quantities of surface attached molecules, specifically monolayer and sub-monolayer collections of molecules. For these types of samples, a sandwich type electrode becomes impractical as the dielectric layers (i.e. the film of molecules under measurement) are less than or on the order of tens of angstroms in thickness and the possibility of shorting contact between two electrode pads becomes very likely. For the IDE configuration, one must be more concerned

with fringing electric fields that are more complicated than for the sandwich electrode. However these fringing fields can also be taken advantage of: beyond measuring the monolayer samples grown between the fingers, much thicker bulk samples can be placed on top of the electrode. Then the fringing fields can be utilized to measure dielectric loss within the bulk volume by the IDE configuration, as shown in Figure 3.4 below.

Interdigitated electrodes (IDEs) were fabricated by near-UV photolithography. Single and double layer lift-off procedures were both utilized. Lift-off lithography (in which metals are deposited onto patterned photoresist and then released by a solvent, see Figure 3.2) was chosen rather than etching (in which the metal is deposited first followed by a resist and then metal etchants are used to reveal the desired pattern) in order to minimize surface alteration during the lithographic process. As variations in the substrate surface may potentially affect the self-assembled monolayer growth, lift-off lithography provided the safest method in terms of preserving the substrate surface characteristics. The substrates used for these experiments were fused silica. The equipment and chemicals used for IDE fabrication were: Quintel Q-6000 mask aligner, KW and Laurell Technologies spin processor, home-built thermal evaporator, Shipley S1818 positive photoresist, LOR 1A lift-off resist (used as a precursor in bi-layer lift-off), MF-319 resist developer, and 1165 resist stripper. All lithographic chemicals were obtained from Microchem.

The following lithographic procedure was used for these experiments. A combination of an UV-ozone surface decontaminator and alcohol solvents are used to clean the substrates.

The substrates are then dried on a hot-plate (200º C for 5 minutes) and allowed to cool to room temperature before proceeding. Photoresist is applied by a commercial spin processor and soft-baked for one minute at 115º C. Again, after allowing to cool, samples are placed in the mask aligner, covered with the appropriate mask, and exposed to a mercury lamp light source. The photoresist is next developed to create the desired pattern. Finally, chromium (~ 175 Å) and gold (~ 1000 Å) were thermally evaporated onto the samples under high vacuum and then the samples are placed in a solvent bath (the stripping process takes from 5-15 minutes with acetone) to complete the lift-off process.

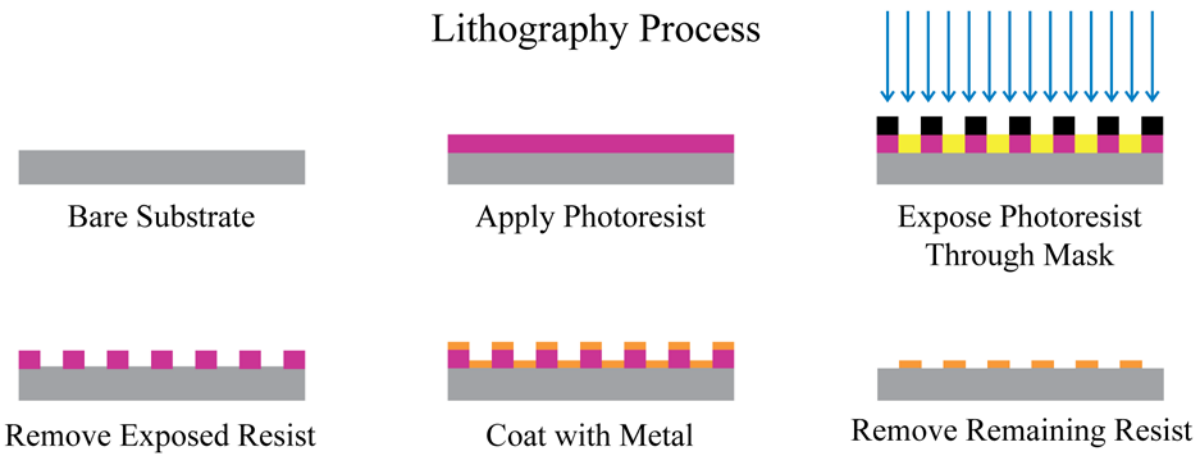

Figure 3.2: Illustration of the lithography process for making interdigitated electrodes. The procedure begins at the top left and proceeds right continuing from left to right for the bottom row of illustrations.

As dielectric spectroscopy is a capacitive measurement, it is important to know the spatial configuration of the electric field present for a given electrode configuration. Because we are utilizing both fringe and "between-plate" electric fields, it is useful to understand the variation, in magnitude and direction, of the fringe field with position. Our monolayer thin film samples are less than 20Å in height, compared to the 700-1000Å height of the electrodes; and the spacing between the electrodes is much greater than either of these distances. For bulk samples placed on top of the IDE, it is necessary to know the significant penetration depth of the electric field into the samples to be aware of what material is contributing to the dielectric spectra. An approximated derivation of the electric potential by Otter was used to calculate the electric field of the IDEs used and is presented here [20]. The IDE and coordinate system used in the derivation is illustrated in Figure 3.3. It is assumed that the IDE thickness is much less than the other characteristic dimensions of the electrode and the number of fingers is large. The assumptions are reasonable for the IDEs used in these experiments as the thickness is ~ 0.1 μm with the spacing (*s*) and width (*w*) equal to 10 μm. For the IDEs used the number of fingers is fifty-two with a length of 1 mm.

Placing the origin of the idealized interdigitated electrode between two electrode fingers, gives the Fourier series

$$V(x,y) = \sum_{n=1}^{\infty} B_n \sin\left(\frac{(2n-1)\pi x}{a}\right) \exp\left(-\frac{(2n-1)\pi |y|}{a}\right), \quad (3.1)$$

as a reasonable potential function form. In the above equation x and y are the position (see Figure 3.3 for coordinate system used) and a is the periodicity, $a = s + w$. To obtain the

Fourier coefficients it is assumed that the potential at $y = 0$ is equal to that of two semi-infinite plates,

$$V(x,y) = \frac{2V_0}{\pi}\,\mathrm{Re}\left[\arcsin\left(\frac{x+iy}{s/2}\right)\right]. \tag{3.2}$$

With these assumptions the coefficients are calculated to be,

$$B_n = \frac{4V_0}{(2n-1)\pi} J_0\left(\frac{(2n-1)\pi s}{2a}\right) \tag{3.3}$$

where J_0 is the zeroth Bessel function of the first kind. Substituting Eq. 3.2 into Eq. 3.1 gives the solution,

$$\begin{aligned} V(x,y) = \frac{4V_0}{\pi}\sum_{n=1}^{\infty}\frac{1}{(2n-1)} J_0\left(\frac{(2n-1)\pi s}{2a}\right) \\ \times \sin\left(\frac{(2n-1)\pi x}{a}\right)\exp\left(-\frac{(2n-1)\pi|y|}{a}\right) \end{aligned}. \tag{3.4}$$

From the potential, the electric field can be found with $\vec{E} = -\vec{\nabla}\Phi_E$. Completing this calculation results in an electric field of,

$$E_x = \frac{4V_0}{a}\sum_{n=1}^{\infty} J_0\left(\frac{(2n-1)\pi s}{2a}\right)\cos\left(\frac{(2n-1)\pi x}{a}\right) \times \exp\left(-\frac{(2n-1)\pi|y|}{a}\right)$$

$$E_y = \frac{-4V_0}{a}\sum_{n=1}^{\infty} J_0\left(\frac{(2n-1)\pi s}{2a}\right)\sin\left(\frac{(2n-1)\pi x}{a}\right) \times \exp\left(-\frac{(2n-1)\pi|y|}{a}\right) \quad (3.5)$$

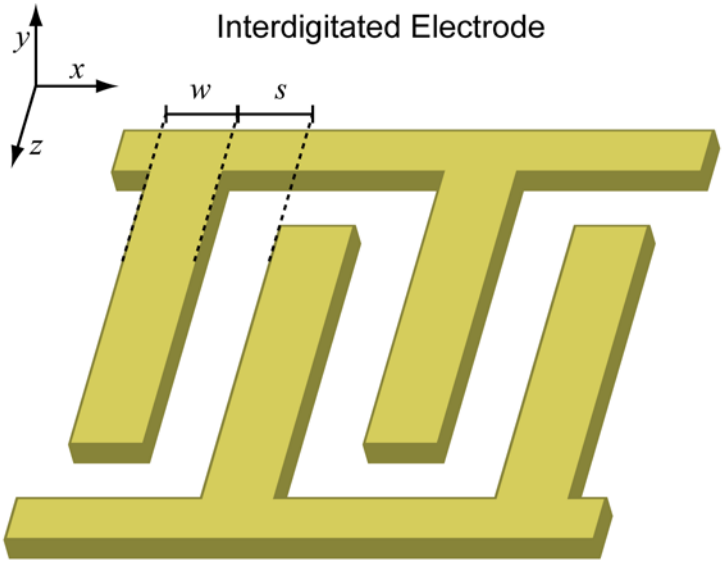

Figure 3.3: Interdigitated electrode illustration including the width (w), spacing (s), and coordinate system used in the electric field calculation.

Figure 3.4 shows the electric field in the xy-plane with the color scale indicating magnitude and the arrow direction. Figure 3.5 plots just the magnitude of the electric field versus the distance above the electrode at the x=0 location (the center of a finger pair). For both figures the first 500 terms in the summations were calculated. An appropriate limit on the electric field required to observe a dielectric relaxation with the equipment used can be calculated from the observed applied voltage for the monolayer system. For that system, an applied potential of less that 5V (peak to peak) becomes problematic in being able to observe the dielectric relaxation. This minimum experimentally required voltage corresponds to an electric field of ~$7x10^5$ V/m in between the electrode fingers. This value of the electric field equivalently corresponds to a penetration depth above the IDE of ~ $1x10^{-5}$ m. This is represented by the horizontal line in Figure 3.5.

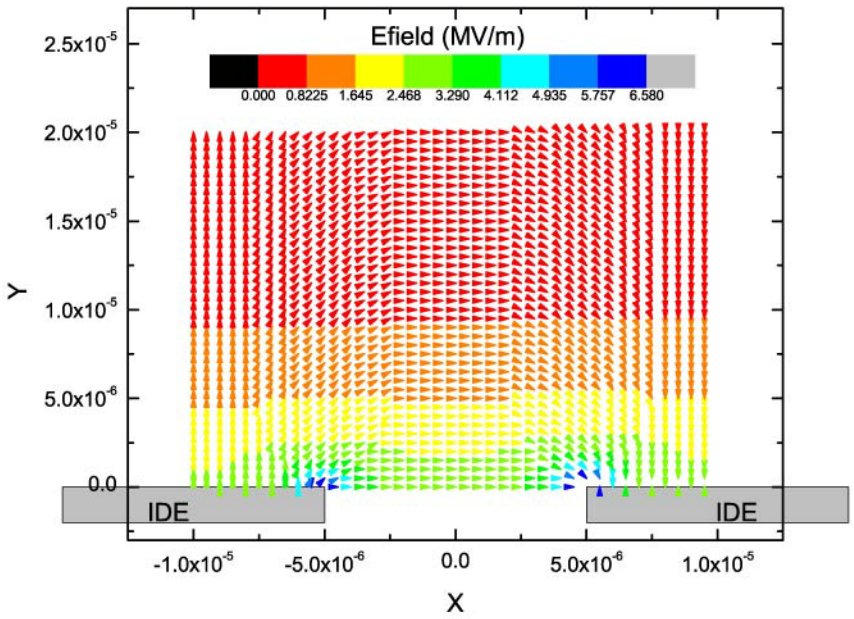

Figure 3.4: Interdigitated electric field in the xy-plane above the IDE. The arrors indicate the direction and magnitude of the electric field by the color map at the top of the graph

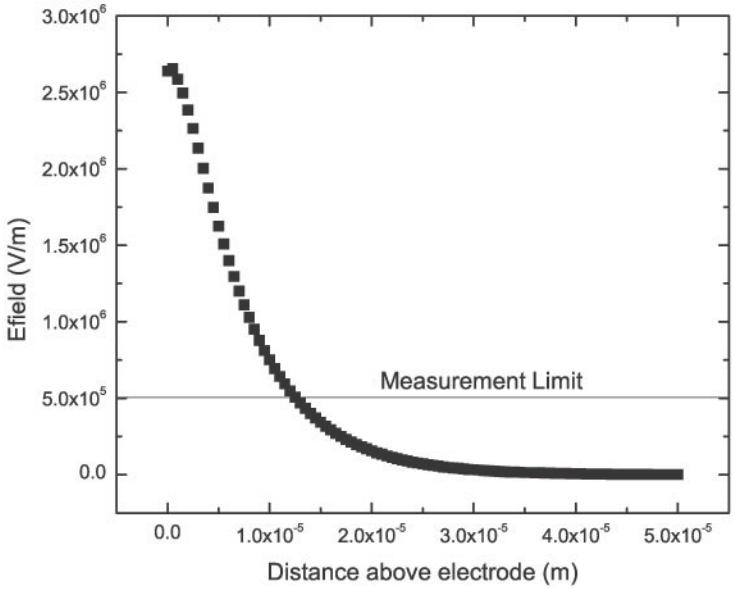

Figure 3.5: Magnitude of the electric field at the location x=0 (center of a finger pair) as a function of the distance above the electrode.

3.2 -Experimental Systems

Two high-vacuum cryogenic systems were used to carry out the experiments included in this dissertation. The arrangement of the two systems will be briefly discussed. The two systems will be referred to as the "prober", as it used physical probes to make electrical contact, and the "chamber", this system has a larger vacuum chamber. Pictures of the systems may be found in Figure 3.6 and Figure 3.7. High-vacuum systems were used to reduce any possible dielectric contaminants, water being the most prevalent. The presence of water can give rise to many problems when performing a very sensitive dielectric measurement. Water can: increase the overall background of the dielectric measurements, have many innate dielectric relaxations that may impede the ability to distinguish the dielectric signature of the molecules of interest, and alter the molecular interaction and possible dynamics available. Because of this the systems used were evacuated to pressures $\leq 10^{-7}$ torr. Both systems used turbo molecular pumps backed by scroll roughing pumps providing a dry vacuum system. With a more open design and larger pumps the chamber typically indicates a lower vacuum than the prober (10^{-7}-10^{-8} torr for the chamber vs. 10^{-6}-10^{-7} torr for the prober) though placement of the gauge in the prober system is not ideal for measuring the vacuum at the sample stage.

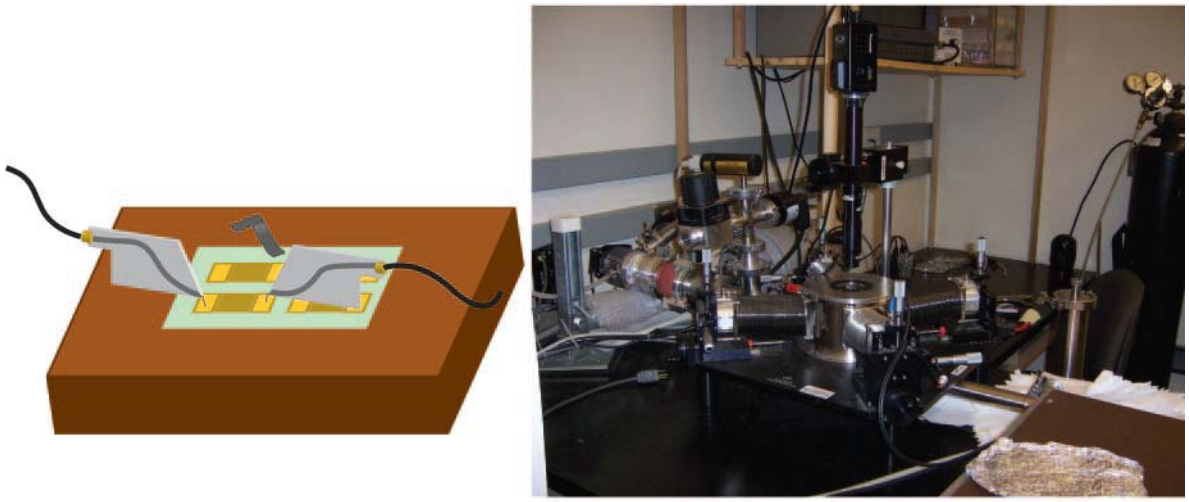

Figure 3.6: Picture of prober system and illustration of sample stage. Metal clips are used to clamp the substrate to the stage and the probes (grey trapezoids) are attached to positional manipulators (not illustrated) and used to make non-permanent electrical contact to the sample.

Temperature control in the systems was carried out by using cryogens and small resistive heaters attached to the sample stages. Depending on the desired temperature range, either liquid nitrogen (allowing temperatures down to ~ 80K) or liquid helium (~6K) was used to cool the samples. A LakeShore temperature controller was used control the temperature of the sample to within a few hundredths of a degree. Liquid helium was typically reserved for the chamber system as it had a greater cooling efficiency and consumed cryogens more moderately.

Each system had a sample stage that housed stage clips to hold the sample in place, heaters and diodes for controlling/monitoring the temperature, and electrical feedthroughs to enable the sensitive dielectric measurement. The prober system used small probes attached to manipulators to make electrical contact to the selected IDE. Non-permanent contact was made between the probe and IDE pads. This system allows the probes to be moved while the chamber remains under vacuum, and enabling multiple electrodes on a single substrate, or on different side-by-side mounted substrates, to be probed and subsequently measured without reopening to atmosphere. The chamber system required permanent contacts to perform the dielectric measurements. Contacts are made to the substrate using silver paint.

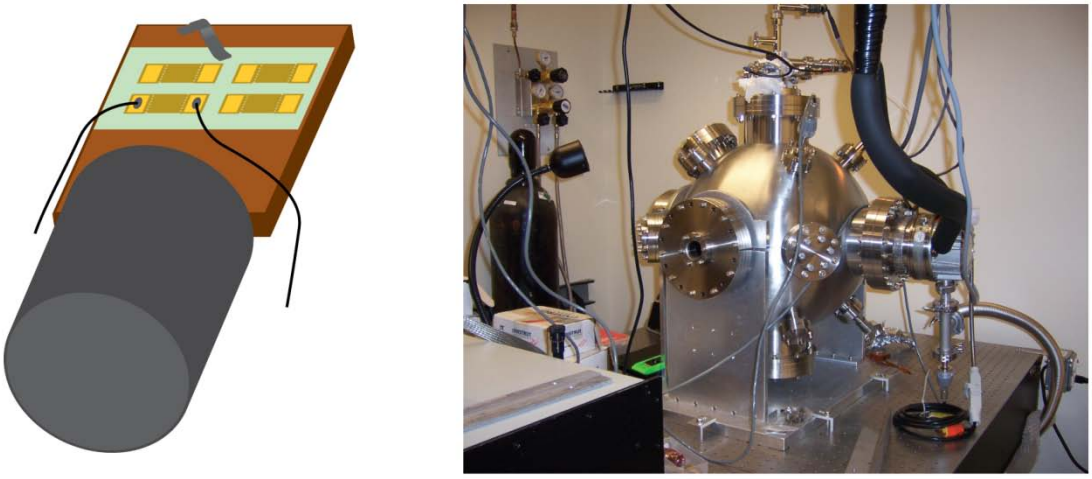

Figure 3.7: Picture of chamber system and illustration of sample stage. Again metal clips are used to secure the substrate to the sample stage, however, the cold head configuration for the chamber system uses permanent contacts (as indicated by the black wires) using silver epoxy.

Capacitance and dielectric loss measurements were made using an Andeen-Hagerling 2700A or 2500A bridge. These are ultra-precision capacitance bridges with a limited frequency range. The 2500A may only apply an alternating potential at 1 kHz. The 2700A is able to supply a number of frequencies in the 50 Hz to 20 kHz range. The AH 2700A is a ratio transformer bridge and a simplified bridge circuit is seen in Figure 3.8. In addition to the sine wave generator the other main components are the ratio transformer and temperature controlled fused-silica reference capacitor. As indicated by the manual, legs 1 and 2 in the circuit diagram have multiple taps to select precisely defined voltages to drive legs 3 and 4. A microprocessor in the unit selects taps1 and 2 as well as C_0 and R_0 to minimize the voltage at the detector. Leg 3 houses the reference capacitors while leg 4 contains the unknown impedance, or sample to be measured. The detector can detect the in-phase voltage and quadrature voltages with respect to the generator voltage. The microprocessor performs the calculation of the measured quantities C_x and R_x where C_x/C_0 is the ratio of the voltage on tap1 to tap2 and R_x/R_0 is the ratio of tap 2 to 1. More information on general bridge theory may be found in the text by Thomas and Clarke [21].

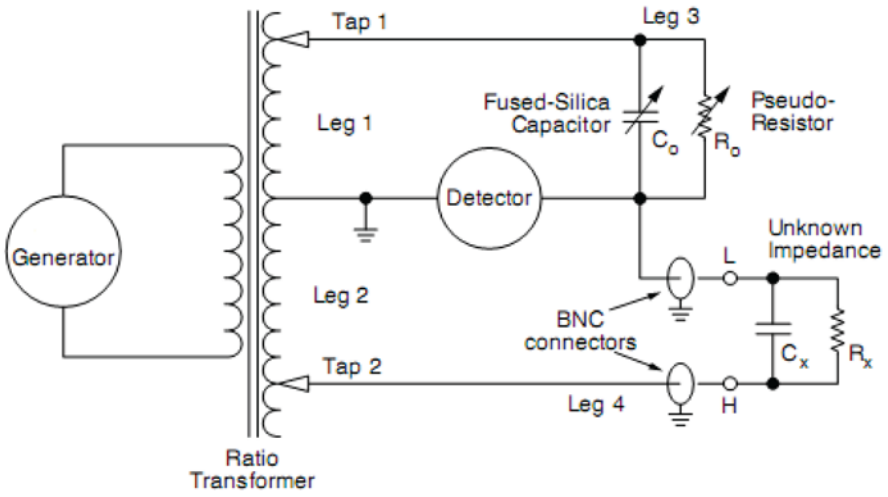

Figure 3.8: Simplified circuit diagram of the AH 2700A bridge. (copied from the AH 2700A manual)

3.3- Film growth and sample preparation

The self-assembled monolayers (SAMs) investigated in this research all utilize silane chemistry to attach to a surface, which for our experiments is fused (amorphous) silica (SiO_2). The molecules studied are chlorosilanes having one to three chlorines bound to a silicon atom that serve as reactive “feet” for possible surface attachment. To measure the dynamics of self-assembled monolayers with dielectric spectroscopy some insulating substrate must be chosen. Fused silica was chosen because it is well characterized, having a single innate dielectric relaxation well below those observed for the molecules studied, and an establish attachment chemistry. In this case, the attachment sites for fused silica are the hydroxyl

groups (-OH) located at the surface. The top portion of the silanes consist of a carbon chain of varying length and in some cases a dipolar terminating group. Drawings of these molecules are shown in Figure 3.9. The growth of silane SAMs depend on both the silane structure and the deposition conditions. Silanes will react with the surface hydroxyl groups creating Si-O-Si bonds between the molecule and the substrate with hydrochloric acid (HCl) as a product. In the presence of water, trichlorosilanes (three reactive feet) can also cross-link creating Si-O-Si bonds between molecules. In the case of trichlorosilanes, it is not likely for all three reactive feet to be surface attached. The average surface hydroxyl density for fused silica is approximately one per 20 $Å^2$ which is similar to the footprint of the trichlorosilanes [22]. For this reason, full trichlorosilane monolayers will likely include cross-linking between molecules. Trichlorosilanes can also polymerize in solution if water is present. The monochlorosilianes may also bond to each other in solution, though the resulting dimers cannot covalently bond to the surface. These growth trends should be taken into consideration as different sample preparations can alter the molecular dynamics.

The SAMs are formed in our lab by either vapor or solution deposition of commercially available molecules. Films used for dielectric measurements are grown onto fused-silica substrates pre-patterned with interdigitated electrodes (see Section 3.1). Solution depositions proceed from placing the electrode in toluene after which the molecules added. Solutions are typically prepared with a volume ratio of 1:1,000 silane to toluene. Additionally, substrates are placed face-down (either by tilting against the side of the vessel or placement on top of a stand) in the pre-silanated deposition vessel to help prevent any

polymerized silanes from attaching to the surface. In both solution and vapor depositions, pyrex deposition vessels are exposed to trimethylchlorosilane to prevent the silanes in subsequent solutions from attaching to the vessel as opposed to the substrate. Vapor depositions were conducted at elevated temperatures in an over at atmosphere. Diagrams of the deposition vessels and substrate placement are in Figure 3.10. The oven temperature is typically around 90º C. The deposition vessel and substrate are placed in the oven prior to the deposition for a sufficient amount of time so as to reach the oven temperature. Afterwards, the neat silanes are deposited onto the surface of the deposition vessel.

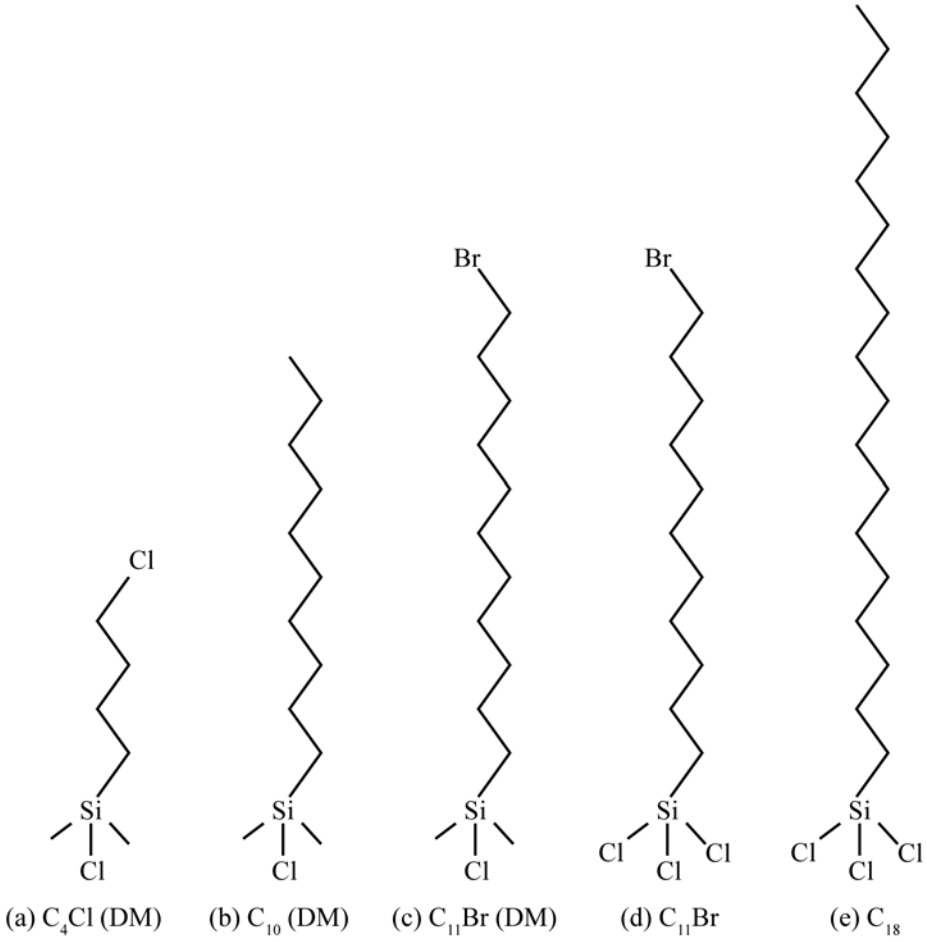

Figure 3.9: Depictions of the molecules used to form the monolayers.
(a) chlorobutyldimethylchlorosilane (C4Cl (DM)), (b) n-decyldimethylchlorosilane (C10 (DM)), (c) 11-bromoundecyldimethylchlorosilane (C11Br (DM)), (d) 11-bromoundecyltrichlorosilane (C11Br), and (e) octadecyltrichlorosilane (C18).

The molecule coverage for both deposition types is controlled by deposition time. For trichlorosilanes available coverages range from very low coverage sub-monolayers through multi-layered films. The monochlorosilanes are limited to around 50% and lower coverages

due to the bulky methyl groups. The two deposition techniques do tend towards different growth mechanisms. Solution depositions, of both types of chlorosilanes, exhibit island formation with areas of high local density. Vapor depositions, however, do not appear to have island formation and cover the substrate more uniformly. The growth characteristics of the mono- and trichlorosilanes are additionally discussed in Chapter 5.

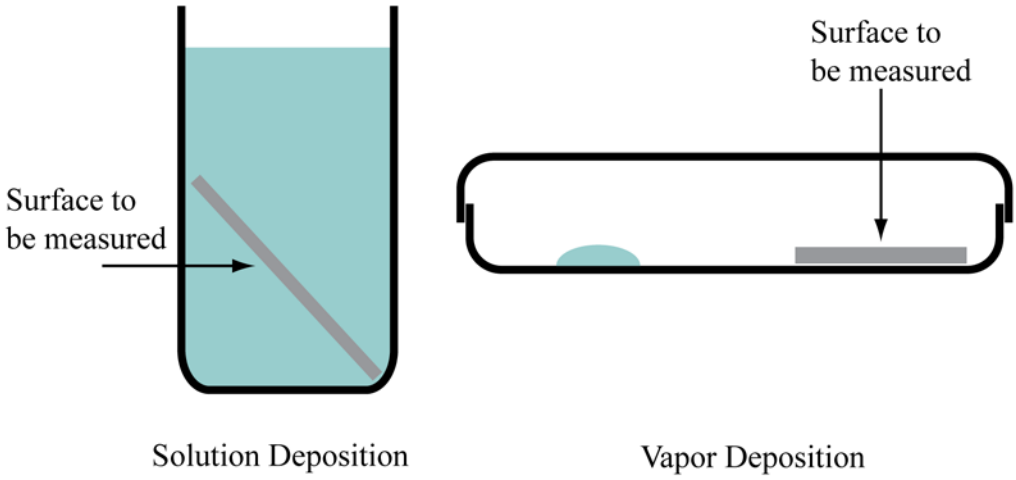

Figure 3.10: Illustration of the deposition set-up for solution phase and vapor phase depositions. The unlabled shaded regions (blue) are the chemical solutions and the black lines represent the deposition vessels.

The second system under study were polymeric materials (these being the responsive surfaces introduced in Chapter 1) of modified poly(vinyl-methylsiloxane) (PVMS) networks. The synthesis of these polymers was not conducted by our group, but our collaborator in this project Dr. Jan Genzer. The synthesis process will not be presented here (detailed reports of

the synthesis have been published [6,23]) however the polymer structure will be discussed. The polymer networks consist of PVMS groups cross-linked by tetraethoxysilane (TEOS) which are then modified by the addition of merkaptoalkanol side-chains to the vinyl group. The chemical structures for each are depicted in Figure 3.12. The chemical formula of the side-chains used to modify the PVMS is S-$(CH_2)_n$-OH with n=2,6, and 11. In addition to the modified PVMS, polydimethylsiloxane (PDMS) was studied which is similar to the PVMS in structure with an additional methyl group in place of the vinyl.

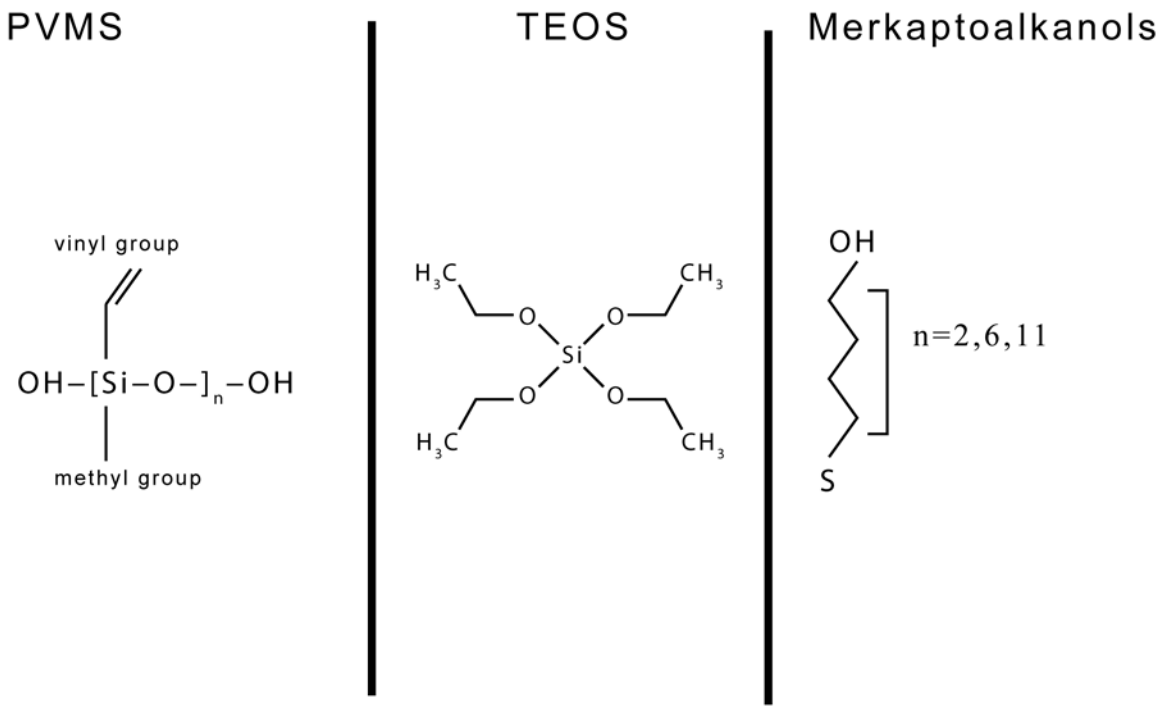

Figure 3.11: Chemical structures of the siloxane networks PVMS and PDMS, the cross-linker TEOS, and the Merkaptoalkanol side-chain modifiers.

After the polymer networks are synthesized they are cast into thick films (thickness is on the order of a few millimeters). For the dielectric measurements, small portions are cut from the films and placed directly on the interdigitated electrode.

3.4- Film characterization

Supplementing the dielectric spectroscopy, ellipsometry and contact angle were used to characterize the self-assembled monolayers. Discussion of the results from these characterizations is included in later chapters. These techniques provided information concerning the film coverage and morphology and brief descriptions of each technique will follow. Ellipsometry was used to determine the SAM thickness and corresponding coverage. The ellipsometer used was a Rudolph AUTO EL automatic ellipsometer, and is a single wavelength ellipsometer using a He-Ne laser. Ellipsometry measures the change in the light's polarization after reflection. From the polarization change and the indices of refraction, the film thickness is determined.

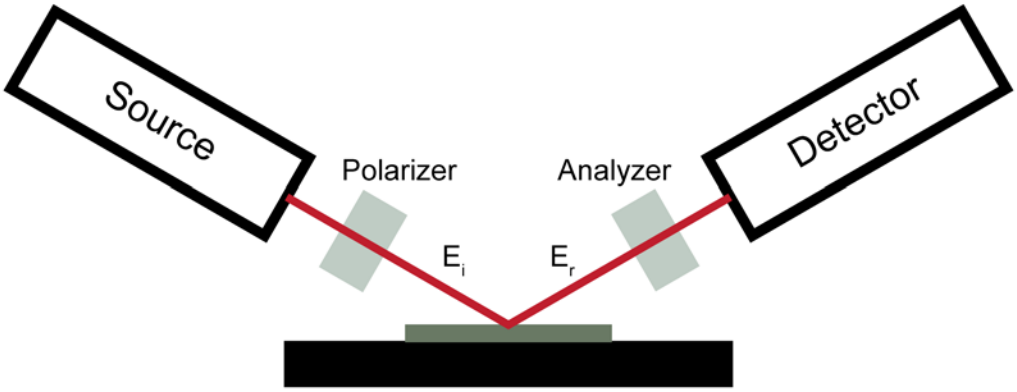

Figure 3.12: Simple illustration of an ellipsometer. The light source (a He-Ne laser in our case) is polarized and reflected off the sample surface. The light then passes through an analyzer and then the detector.

Water contact angle measurements were also performed as an additional characterization of SAM coverage. A droplet of deionized water is place on the surface and a picture is taken. From the picture, the angle at which the water meets the surface is determined. For our systems, the contact angle is an indication of film coverage and quality as this quantity will vary based on how the molecules are oriented on the surface due to differences in the innate contact angle of the substrate and molecules attached. The contact angle for the SAMs is also a function of their terminating group. Example contact angle pictures are in Figure 3.14.

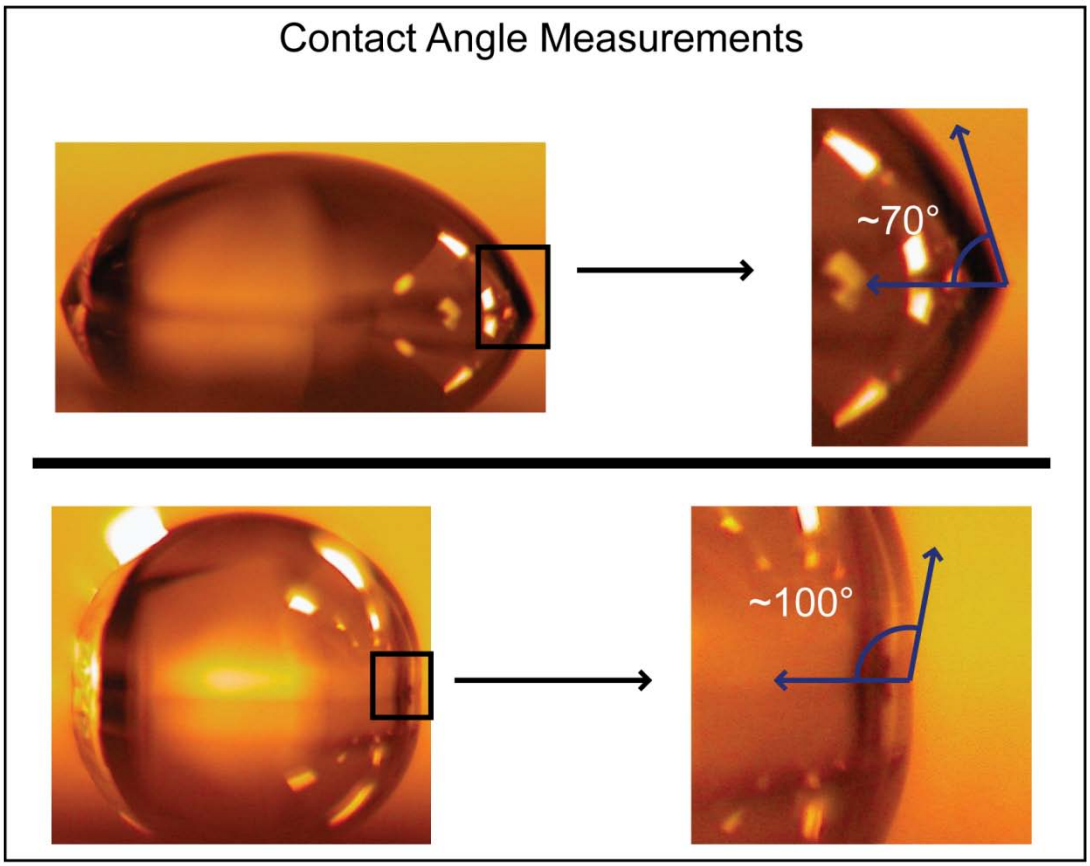

Figure 3.13: Example pictures used to determine the contact angle. The example on the bottom is more hydrophobic than that on the top.

Chapter 4- Dynamics in functional silicone elastomer networks

4.1-Introduction

As mentioned, the polymer system studied exhibits a change in its surface wetting properties with exposure to different media, water versus air. In general, materials of this type respond to external stimuli with an alteration of their physical and/or chemical properties including wettability, color, or size with the microscopic origin commonly a conformal change in the molecular structure. These are often referred to as stimuli-responsive materials [24,25]. In general, materials of this type respond to external stimuli with an alteration of their physical and/or chemical properties including wettability, color, or size as the result of a microscopic change, such as a conformal change in the molecular structure. The chemical structure and composition determines what stimuli (external electric field, exposure to light, pH, temperature, etc.) will lead to a response in the material. Applications such as microfluidics and separation media could potentially benefit from the multifunctional nature of stimuli-responsive materials and much interest in this area has been reported [24--26]. Modified poly(vinyl methylsiloxane) PVMS networks consisting of linear PVMS, a cross-linker and substituted side-chains (as described in section 3.3) are the stimuli-responsive materials studied. Previous work by the Genzer group characterized this material's change in wettability as a response to the hydrophobicity of the surrounding media

[6,23]. This change is a result of reorientation (flipping at the surface) of the side groups in the material which have different hydrophobicities.

The aim of this work was to observe and characterize the available dynamics in the PVMS networks, how these dynamics are altered by the introduction of different side-chains, and (in collaboration with Jan Genzer) correlate the macroscopic response and microscopic dynamics. As this thesis is primarily concerned with microscopic dynamics, the bulk of this chapter will be examining the dynamics, as determined by dielectric spectroscopy, for four polymer networks, listed in Table 4.1.

Table 4.1: Names and descriptions of polymers studied.

Polymer Name	Description
PVMS	siloxane backbone with one methyl and one vinyl (-CH=CH_2) side group per monomer
PVMS-S-$(CH_2)_2$-OH	siloxane backbone with one methyl and one –C_2S-$(CH_2)_2$-OH side group
PVMS-S-$(CH_2)_6$-OH	siloxane backbone with one methyl and one –C_2S-$(CH_2)_6$-OH side group
PVMS-S-$(CH_2)_{11}$-OH	siloxane backbone with one methyl and one –C_2S-$(CH_2)_{11}$-OH side group

However, summarizing statements of the macroscopic characterization carried out by Dr. Jan Genzer's group are included throughout the text in addition to Table 4.2 which qualitatively summarizes the wetting stimuli-response results. The results in Table 4.2 were concluded by measuring the dynamic contact angle (DCA) for PVMS network and describe the materials change in contact angle upon exposure to deionized water [23].

Table 4.2: Qualitative results of dynamic contact angle measurements for PVMS, PVMS-S-(CH2)2-OH, PVMS-S-(CH2)6-OH, and PVMS-S-(CH2)11-OH [16,17].

Polymer Network	Response Time	Response Amplitude
PVMS	Fastest in contact angle change	Smallest change in contact angle
PVMS-S-$(CH_2)_2$-OH	Slower than PVMS	Much larger change in contact angle than PVMS
PVMS-S-$(CH_2)_6$-OH	Slower than PVMS but approximately equal to PVMS-S-$(CH_2)_2$-OH	Change is again larger than PVMS though slightly smaller than PVMS-S-$(CH_2)_2$-OH
PVMS-S-$(CH_2)_{11}$-OH	Slowest; largest response time	Initial response closer to that of the PVMS, however repeated cycling of the contact angle measurement resulted in a quickly diminishing response amplitude

4.2-PVMS

For unmodified cross-linked PVMS, the dissipation factor showed a sharp peak, the peak location being the temperature where the molecular motion is occurring as the same rate as the applied electric field, located from 145 K to 155 K for 0.1 Hz and 20 kHz respectively. The dissipation factor and capacitance for data at 10 kHz is shown in Figure 4.1. Additionally, a subset of the multifrequency data in Figure 4.2 shows the slow dispersal of the relaxation.

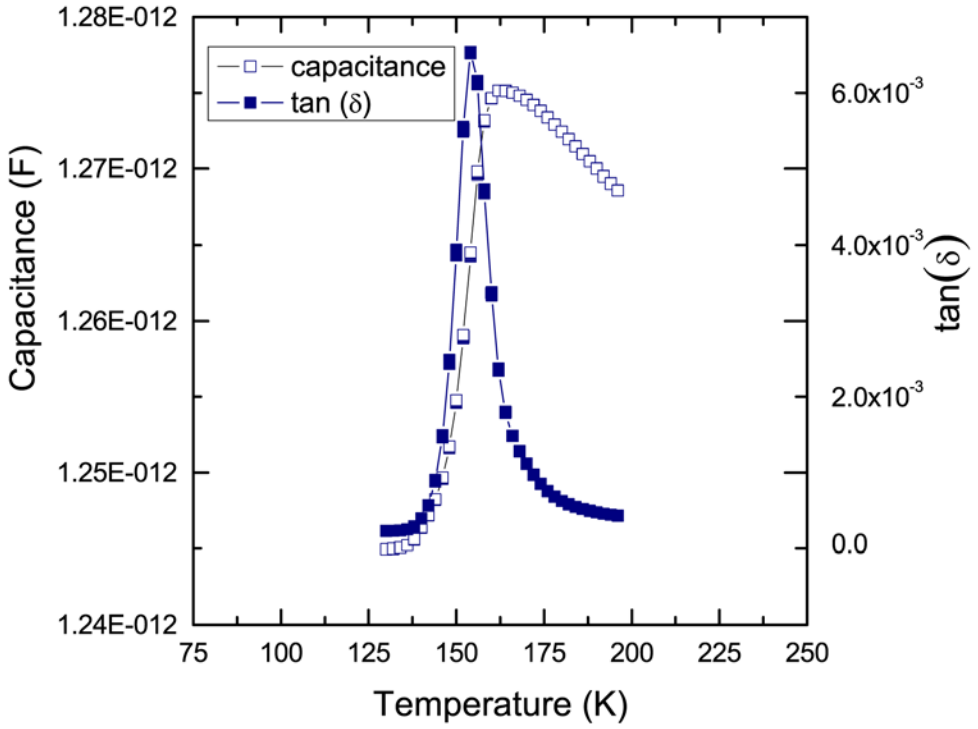

Figure 4.1: Capacitance (open squares) and dissipation factor (filled squares) at an applied field frequency of 10 kHz for PVMS. A single relaxation is present around 155 K.

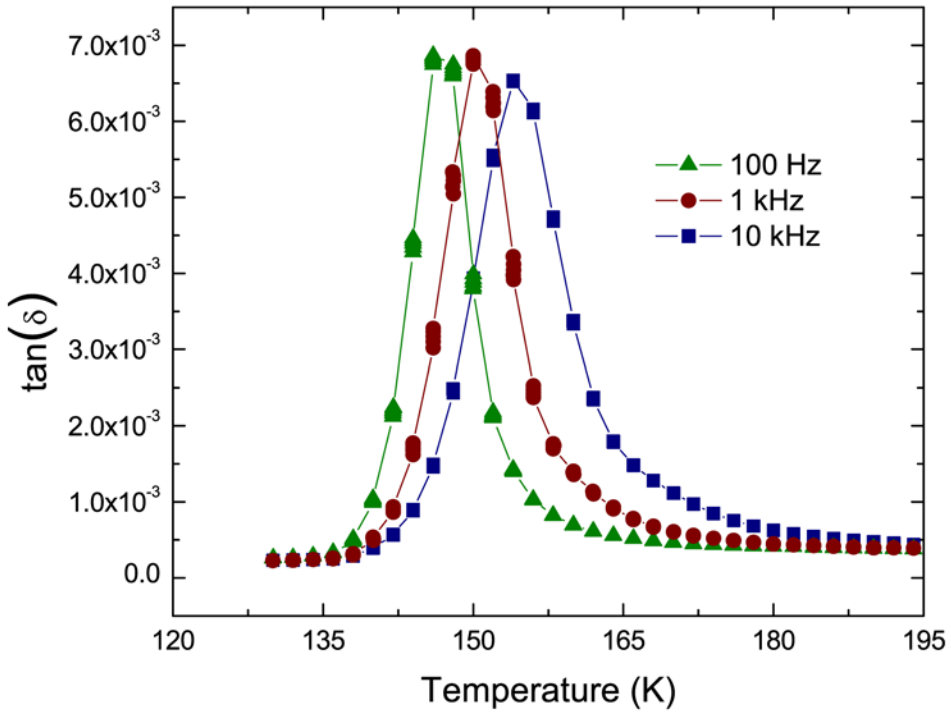

Figure 4.2: Dissipation factor for PVMS at multiple frequencies: 100 Hz (triangles), 1 kHz (circles), and 10 kHz (squares).

The peak location data is shown in Figure 4.3. An Arrhenius fit (Eq. 2.17) of the peak location data produced non-physical results (with an apparent attempt frequency of ~ $1x10^{40}$ rad/sec) however a VFT fit (Eq. 2.50) was successfully applied. Calculation of the glass transition temperature (T_g) by extrapolating the VFT fit to a τ=100 s resulted in $T_g = 137^{+5}_{-10}$ K. Linear PVMS has a reported T_g of 143 K [27], thus the crosslinking does not appear to have altered the glass transition temperature. As with the wetting characteristics the PVMS data will serve as the base of comparison for the modified PVMS networks. The dielectric

data appears to correspond well with the fast wetting response in that a moderately low glass transition was observed and reasonably explains why the small side groups are able to flip at the surface quickly. The lower response amplitude in the wetting data (Table 4.2) as compared to the other shorter chain PVMS networks is contributable to the difference in the hydrophobicity of the vinyl group vs. the –OH group present in the later materials.

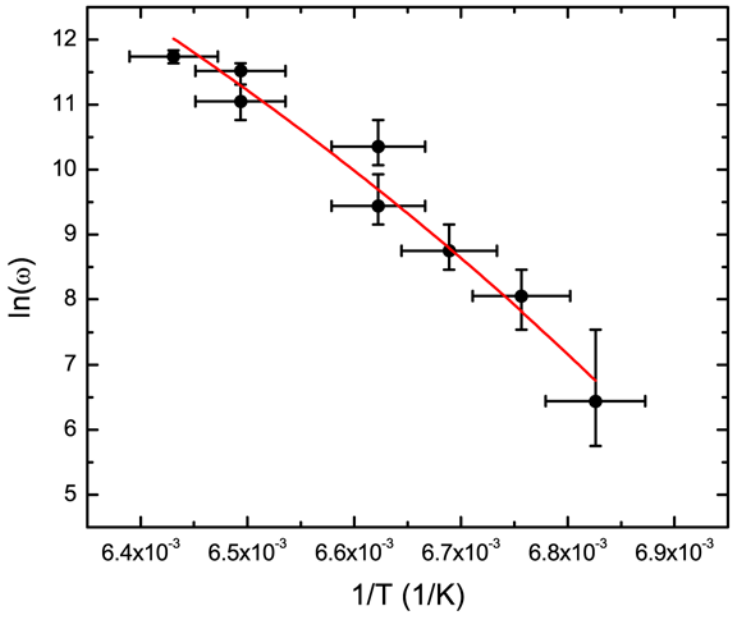

Figure 4.3: Arrhenius plot for PVMS. The natural log of the field frequency is plotted against the inverse peak location temperature. The red line corresponds to a VFT fit of the data.

4.3- PVMS-S-$(CH_2)_2$-OH

This next molecule is similar to the PVMS, but with the S-$(CH)_2$-OH side group substituted for the vinyl side group. The most obvious difference in the dielectric data when

adding the S-$(CH)_2$-OH side group is a secondary relaxation (see Figure 4.4). The lower, smaller peak is located from 180 K to 210 K for frequencies of 100 Hz to 5 kHz. At frequencies beyond that the dispersion of the peak shifts it into the range of the higher temperature relaxation and cannot be clearly distinguished (see Figure 4.5). The high temperature, large amplitude peak occurs at 240K to 250K for 100 Hz to 20 kHz. At the higher frequencies the dispersion of the peak is less than the temperature resolution of this data. Relaxations from a strongly interacting system or “glassy” type relaxations often result in dynamics that change rapidly with temperature. The unmodified PVMS glass transition relaxation in the previous section showed a similar dispersal behavior though at a much lower temperature.

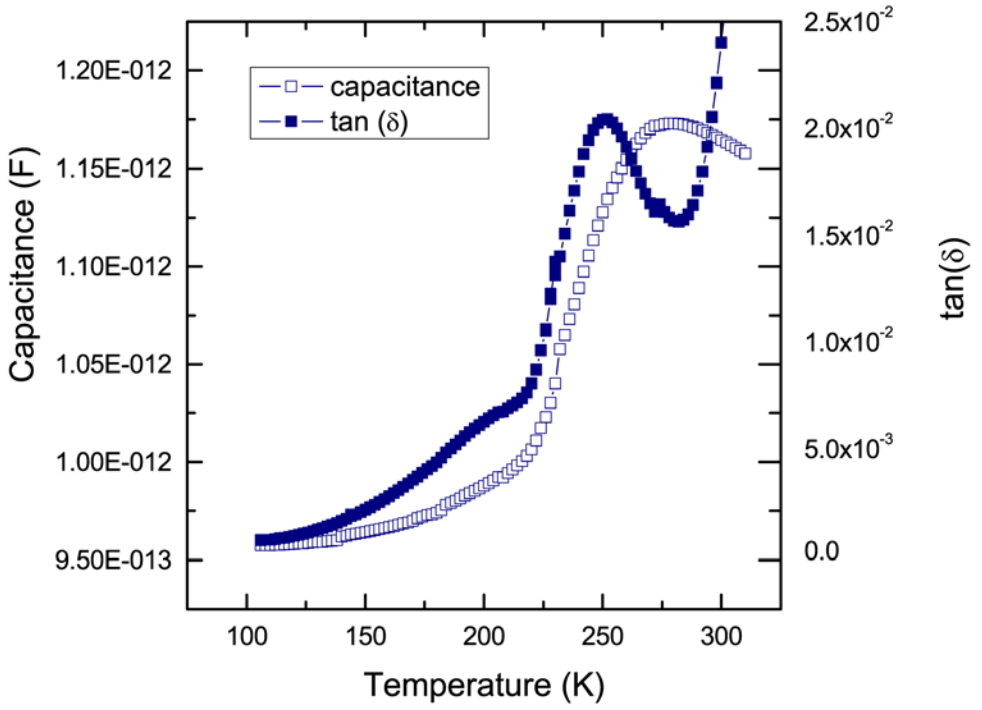

Figure 4.4: Capacitance and dissipation factor for PVMS-S-$(CH_2)_2$-OH at 10 kHz. Two relaxations are observed at ~250 K and ~ 190 K for this data.

The Arrhenius plot for the lower relaxation, Figure 4.6, resulted in a straight line which after being fit with the Arrhenius equation had an apparent attempt frequency of ~10^{16} rad/sec. and a barrier of 10.9 ± 0.8 kcal/mol. The slightly higher apparent attempt frequency indicates some level of interaction present. Starkweather analysis can be applied to investigate the degree of interaction between the side chains. The apparent attempt frequency from the Arrhenius fit corresponds to an entropy change of ΔS = 60 ± 10 J/mol/K. This consistent with there being some interaction, though much lower than that typically associated with backbone glass transitions. There exists a well-known local (γ) relaxation in

the 120-150K range (for 100 Hz) that is associated with alkyl side groups [28,29]. Though the exact nature of the relaxation is still debated, it is mostly independent of the backbone structure. The barriers observed for this γ relaxation in the above temperature range are 6-7 kcal/mol. However, this relaxation has been observed at higher temperature (larger barriers) when substituted polar groups such as -C≡N [30], -OH [31], or $–CF_2H$ [32] are present. This is attributed to interaction between the terminal groups. Our results are consistent with this relaxation and conclude that the low temperature relaxation is most likely (or very similar to) the γ relaxation.

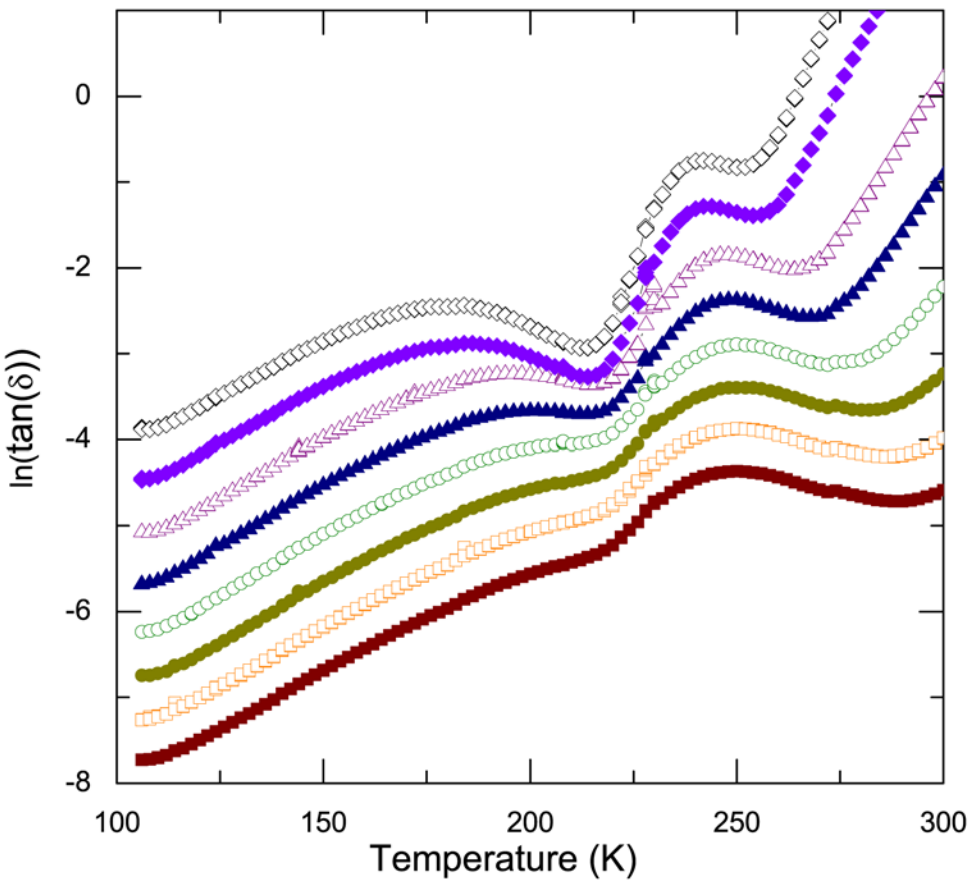

Figure 4.5: Natural log of the dissipation factor vs. temperature for PVMS-S-$(CH_2)_2$-OH. The natural log was used to easily see the low temperature relaxation which has a much smaller amplitude than the high temperature relaxation. Additionally, an arbitrary y-axis offset was applied to each data set to make the individual relaxation more distinguishable. Data shown are for frequencies: 100 Hz (open diamonds), 200 Hz (filled diamonds), 1 kHz (open triangles), 2 kHz (filled triangles), 5 kHz (open circles), 10 kHz (filled circles), 16 kHz (open squares), and 20 kHz (filled squares).

The higher temperate peak Arrhenius plot, Figure 4.6, resulted in an apparent attempt frequency of ~ 10^{100} rad/sec when an Arrhenius fit was applied. This is indicative of a highly interacting relaxation and consistent with this relaxation being the glass transition. Because

of this VFT analysis was applied and resulted in a $T_g = 226^{+6}_{-10}$ K which is almost 100 K above that of the PVMS. Recalling the summary of the dynamic contact angle data in the introduction, while the amplitude of the contact angle change is larger for the PVMS-S-$(CH_2)_2$-OH, attributable to the –OH terminal group, the response time was slower than that of the PVMS. This is consistent with increase in the glass transition as at room temperature the PVMS-S-$(CH_2)_2$-OH less flexible than the PVMS.

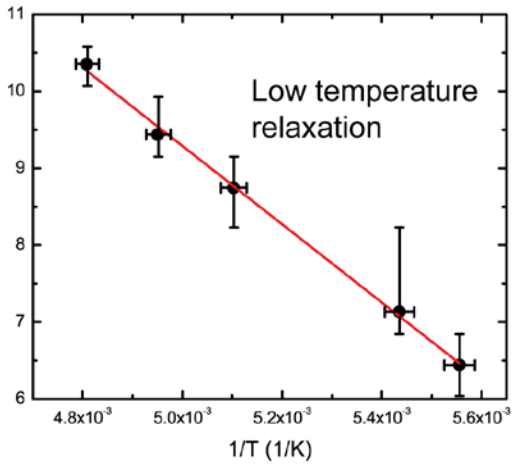

Figure 4.6: Arrhenius plot for low temperature relaxation. The red line corresponds to the Arrhenius fit.

4.4- PVMS-S-$(CH_2)_6$-OH

Introduction of the longer six-carbon side group again resulted in two peaks, though the low temperature peak is only readily seen in the lower frequencies. The low temperature, smaller amplitude peak can be seen at 100 Hz (Figure 4.8), but above 500 Hz it begins

shifting into the higher temperature peak, though partially reemerges at the highest frequencies. As with the PVMS-S-$(CH_2)_2$-OH, a there is second higher temperature peak and it is located around 240 K. For the higher frequencies the two peaks are still merged but two distinct features are observable and result in a somewhat split peak. The higher temperature peak position ranges from 245 K to 270 K for 100 Hz – 20 kHz which is very similar to the high temperature peak in PVMS-S-$(CH_2)_2$-OH.

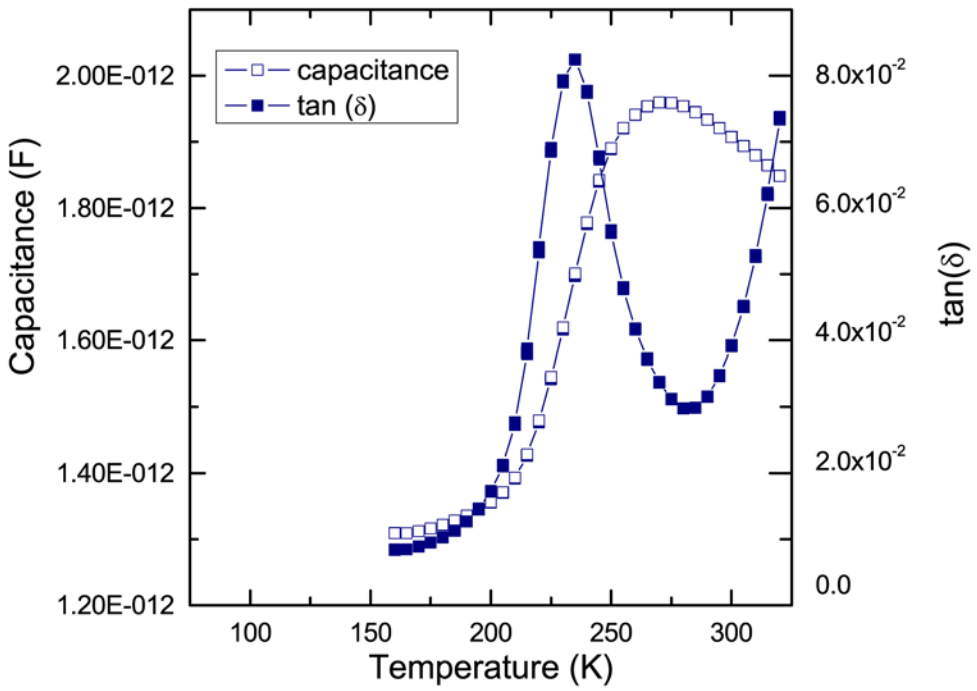

Figure 4.7: Capacitance and dissipation factor plots for PVMS-S-$(CH_2)_6$-OH at 10 kHz. At this frequency only the high temperature relaxation is distinguishable.

The low temperature relaxation peak's position could only be reasonably determined for a few frequencies (Figure 4.9). The Arrhenius plot of the available data did appear to result in a straight line, and from this limited data we conclude that the side chain relaxation is very similar to that of the PVMS-S-$(CH_2)_2$-OH but will refrain from quantifying the relaxation. VFT analysis was applied to the high temperature relaxation with a calculated T_g of 220^{+12}_{-29} K. This value overlaps with the glass transition temperature for PVMS-S-$(CH_2)_2$-OH and is assigned as such for the PVMS-S-$(CH_2)_6$-OH network.

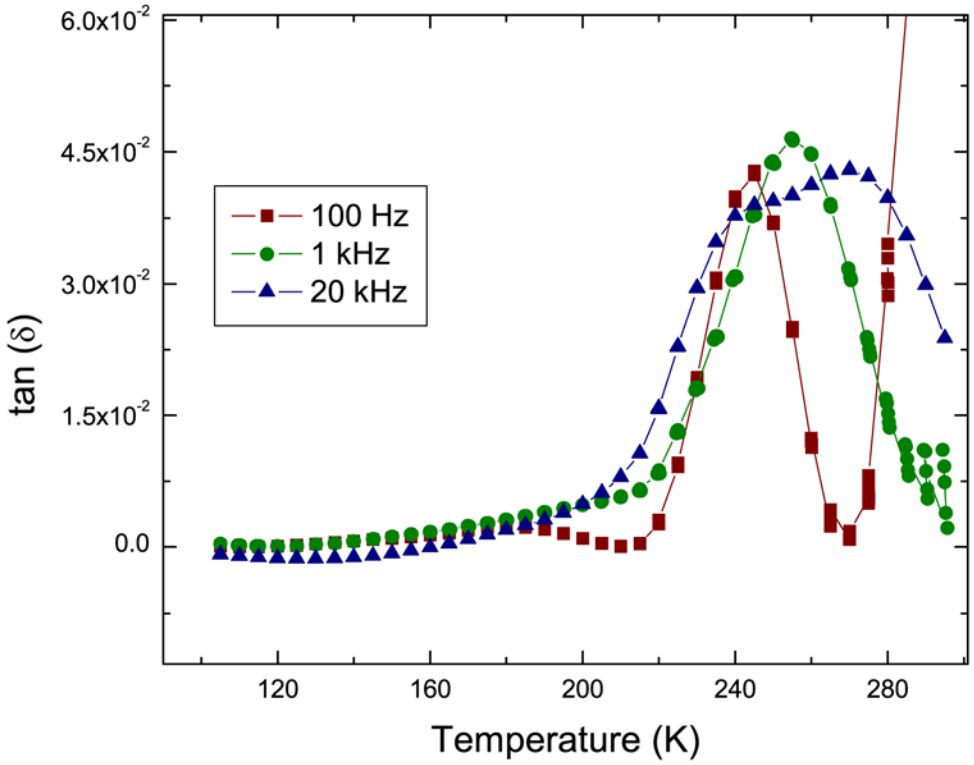

Figure 4.8: Subset of the dissipation factor data for PVMS-S-$(CH_2)_6$-OH at 100 Hz (squares), 1 kHz (circles), and 20 kHz (triangles). In the 100 Hz curve two relaxations are clearly seen at ~180K and ~ 240K. At 1 kHz the lower relaxation has shifted up into the higher relaxation (located at ~255 K) and is not readily seen. The 20 kHz data shows a split-peak structure with two peak temperatures at ~240K and ~270K.

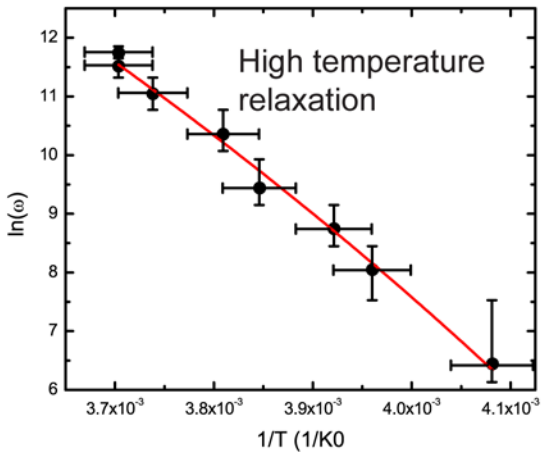

Figure 4.9: Arrhenius plot for the high temperature relaxations. The line (red) is the VFT fit of the data.

4.5- PVMS-S-$(CH_2)_{11}$-OH

As with the other modified PVMS networks, this one also displayed two relaxations in the dielectric data (Figure 4.10). The lower temperature relaxation is present at 200 K to 230 K for 100 Hz to 20 kHz. This is slightly higher than the corresponding relaxation in the shorter side chains. The Arrhenius fit (Figure 4.12) of this relaxation indicated much more interaction than the previous samples with an apparent attempt frequency of ~10^{20} rad/sec and an effective barrier of 16 ± 0.8 kcal/mol. Calculated from Starkweather analysis, ΔS = 115 ± 32 J/mol/K compared to the ΔS of 60 J/mol/K for PVMS-S-$(CH_2)_2$-OH. It is

reasonable to say the PVMS-S-$(CH_2)_{11}$-OH side chains are significantly more interacting than either of the other modified PVMS networks. This is consistent with observations that the PVMS-S-$(CH_2)_{11}$-OH is semi-crystalline [6,23].An additional point of interest is that the amplitude of the side chain relaxation increased with the peak temperature (Figure 4.11), which was not observed for either PVMS-S-$(CH_2)_2$-OH or PVMS-S-$(CH_2)_6$-OH. This behavior can be a result of the number of units participating in the relaxation increasing with temperature. This could occur if only the amorphous regions are contributing to the dielectric relaxation and as the temperature is changing so is the amount of molecules in an amorphous versus crystalline region.

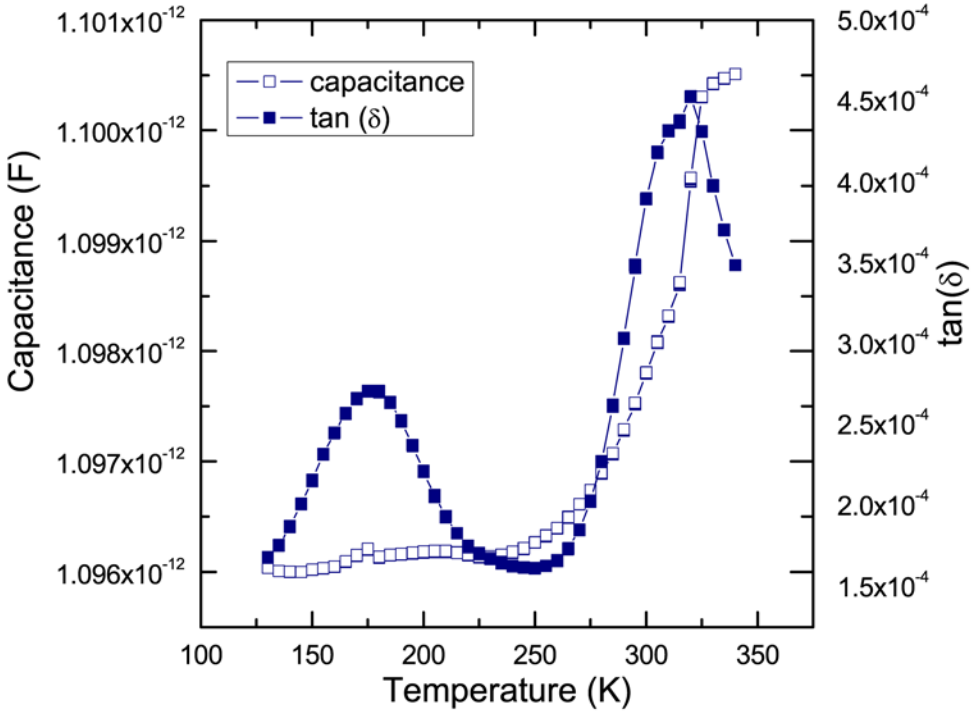

Figure 4.10: Capacitance and dissipation factor for PVMS-S-$(CH_2)_{11}$-OH at 10 kHz. Two relaxations are present at ~175K and ~310K.

A high temperature relaxation was observed at 300-320K. This is consistent with the melting temperature of this material. Most samples did not show a peak associated with the glass transition, though a few, particularly ones that were measured after being held in ambient conditions for approximately a year after fabrication, exhibited a high temperature relaxation lower than the observed melting. This relaxation, occurring from 282 K – 287 K (320 Hz – 20 kHz), did correspond with a glass transition resulting in a T_g in the 270 K – 290 K range. This assignment was confirmed by dynamical mechanical analysis and differential scanning

calorimetry. A lack of reproducibility observed for PVMS-S-$(CH_2)_{11}$-OH as compared to the $(CH_2)_2$ and $(CH_2)_6$ variants is likely due to the semi-crystalline nature of the material. These results are again consistent with the dynamic contact angle in that the response of the PVMS-S-$(CH_2)_{11}$-OH was the slowest of the polymers studied.

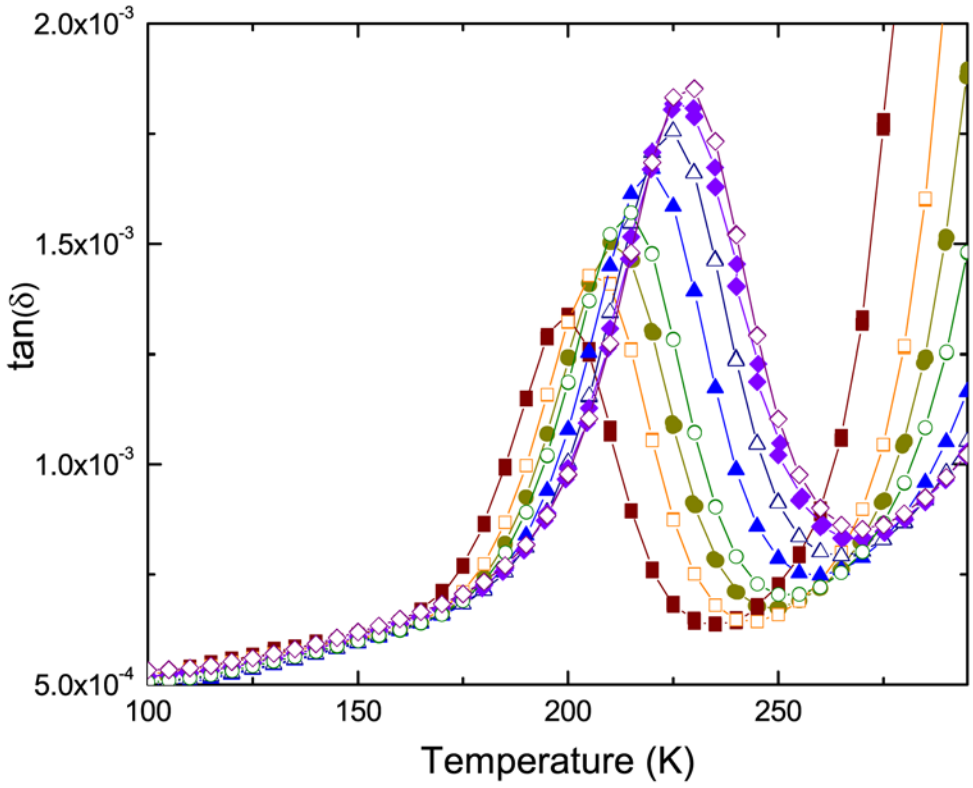

Figure 4.11: Dissipation factor for the low temperature relaxation in PVMS-S-$(CH_2)_{11}$-OH at multiple frequencies: 100 Hz (filled squares), 500 Hz (open squares), 1 kHz (filled circles), 2 kHz (open circles), 5 kHz (filled triangles), 10 kHz (open triangles), 16 kHz (filled diamonds), 20 kHz (open diamonds).

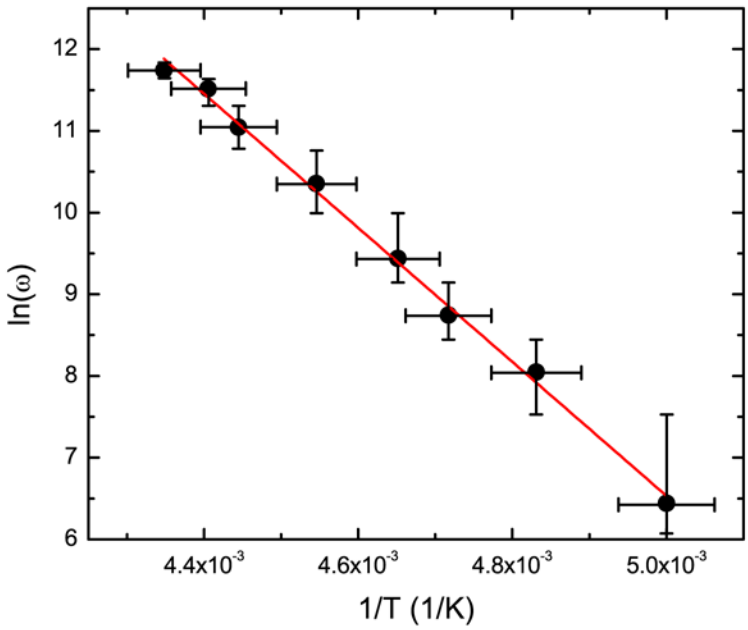

Figure 4.12: Arrhenius plot for the low temperature relaxation in PVMS-S-$(CH_2)_{11}$-OH. The red line is an Arrhenius fit of the data.

4.6-Conclusions

The primary result in substituting the different side groups was to change the glass transition temperature as the different groups constrained the siloxane backbone to different degrees. The macroscopic response summarized in table 4.2 depends on the side group's ability to reorient through the PVMS network. The change in responsiveness appears then to be indicative of network's change in flexibility. Significant side group interactions result in an increase in the glass transition temperature and exhibit a slow macroscopic response time. Systems with lower side group interaction have response times that are closer to the

unmodified PVMS. In summary, the unmodified PVMS showed the fastest macroscopic response time and had the lowest glass transition temperature with no visible side group relaxation. PVMS-S-$(CH_2)_2$-OH and PVMS-S-$(CH_2)_6$-OH have similar macroscopic response time with PVMS-S-$(CH_2)_6$-OH slower than PVMS-S-$(CH_2)_2$-OH and both slower than PVMS. Accordingly the glass transition temperatures for both are higher than PVMS with PVMS-S-$(CH_2)_6$-OH being slightly higher than PVMS-S-$(CH_2)_2$-OH. Both samples displayed an additional relaxation from the side groups and it is this side group interaction that contributes to increasing the glass transition temperature. PVMS-S-$(CH_2)_{11}$-OH had the slowest macroscopic response time as well as the highest glass transition, when visible. Side group relaxations were also observed for PVMS-S-$(CH_2)_{11}$-OH with more significant interactions than either the PVMS-S-$(CH_2)_6$-OH or PVMS-S-$(CH_2)_2$-OH. These dynamical conclusions were confirmed by both dynamical mechanical analysis and differential scanning calorimetry. These results are outside the scope of this thesis, though they are pending publication.

Chapter 5-Dynamics in Self-assembled Monolayers

5.1-Introduction

Self-assembled monolayers (SAMs) are well established systems for scientific and technological investigations due to their ease of preparation, physical robustness, and facile ability to controllably modify chemical properties of surfaces. A brief sampling of the diverse applications for which SAMs have been utilized include creation of new molecular devices [33], lithographic patterning [34,35], reduction of friction, alteration of surface wetting (*i.e.*, hydrophobic vs. hydrophilic), corrosion protection, light-activated switching [36], and acting as an interfacial layer in biological applications [37] as well as stationary phases for shape recognition in liquid chromatography [38--40]. SAMs are also utilized in surface modification of metal nanoparticles, enhancing the particles' solubility and preventing aggregation into larger metal clusters [41,42]. Nanoparticle-monolayer systems are referred to as 3D SAMs and have been used in previous studies of molecular dynamics within monolayers as the increased surface area provides higher signal size, although structural and dynamic properties may differ from planar 2D SAMs, where molecular attachment occurs onto flat surfaces. The observed dynamics within planar SAMs are the focus in this chapter.

The two most commonly utilized covalently-bound SAMs are those created by utilizing thiol-based or silane-based chemistry, with the sulfur (silicon) headgroup forming the chemical linkage to the appropriate metallized (hydroxylated) surface, an alkyl carbon-

chain with varying available lengths, and an application specific, functionalized chemical group at the end of the chain. Siloxane monolayers may be fabricated with or without cross-linking; furthermore, they generally exhibit a lower level of order than their thiol counterparts. Extensive previously published work on high density alkylsiloxane and alkanethiol films indicate that the film ordering increases with chain length due to enhanced intermolecular interactions. These interactions can also lead to growth via island formation (particularly from solution phase). When shorter length chains (< 5 carbon-chain length) are used, or at dilute coverage for short and long chains, a more disordered film results; disordered monolayers are often described as "liquid-like" in contrast with the more ordered "solid-like" structures. Deposition temperature and technique also affect film order with lower temperature, solution phase samples typically the most ordered, and high temperature, vapor-phase depositions significantly more disordered.

Research on SAMs has usually focused on mechanisms of growth and procedures for optimization, having the implied goal to generate full coverage, monolayer films, with alkanethiols on Au(111) regarded as the archetype of an ordered (near crystalline) 2D SAM [43,44]. In contrast, in this thesis, we study dynamics within monolayers with varying intermolecular interactions (due either to molecular structure or density), degree of ordering, and molecular structure. As discussed previously, out substrate acts as a means to physically constrain the collection of molecules under study. The attachment point of each molecule cannot move, and the overall molecular density is experimentally fixed, while retaining significant conformational freedom (particularly at low densities). This experimental design,

combined with the highly sensitive technique employed, enables observation of the interplay of intramolecular, intermolecular, and molecule-substrate interactions in determining resultant molecular dynamics. Such basic understanding of the possible motions of molecular assemblies on surfaces remains an important area of nanoscale scientific focus, both for development of new technologies [4] and further expanding fundamental knowledge, which connects the morphological structure and motional behavior of the bound molecules on the microscopic level to the overall physical properties of the resultant film at the macroscopic scale. Furthermore, these experiments enable future manipulation of molecular dynamics, for instance, by introduction of strong molecule-molecule interactions that could result in previously unexplored phase transitions within this quasi-two dimensional environment.

In this research, we utilize alkyl terminated monolayers in order to connect with previous dynamics studies of alkanes, including plastic crystal phases within solid alkanes [45], relaxations within polymers with an alkane backbone [16,46], and the dynamics of phase separated, alkyl-side-chain containing polymers [47]. Thus, the presence, absence, modification, or creation of new or previously observed dielectric relaxations within a SAM reveals how the local environment, including restriction of the molecular center-of-mass and arrangement on a planar surface influences the motional possibilities of this most basic hydrocarbon structure. As discussed, we make use of silane chemistry, as siloxane monolayers may be fabricated with or without cross-linking, which provides increased flexibility to create variation in film structure and chain-to-chain interactions. Vapor-phase depositions at high temperature are utilized as a solvent-free mechanism to produce dilute,

homogeneous films without island formation. Beginning with these dilute, disordered structures, the transition to a dense, more ordered monolayer, and the associated changes in dynamics, can be systematically observed. In particular, we observe an interacting relaxation in alkylsiloxane monolayers with varying chain length from 4 to 18 carbons, and densities varying from 10% to multilayer coverage. The relaxation occurs in the same location and disperses with frequency in a similar manner to polyethylene-like glass transitions observed in polymers with phase-segregated alkyl-side-chains. At higher density, a localized relaxation, which has Arrhenius dynamics, is observed, consistent with a previous report utilizing a 3D approach [48], and assigned to a similar local motion within polyethylene (PE).

Myriad characterization techniques have been applied to SAMs [43], such as scanning tunneling microscopy (STM), atomic force microscopy (AFM), nuclear magnetic resonance (NMR), neutron scattering, infrared spectroscopy, differential scanning calorimetry (DSC), as well as various forms of electron and X-ray spectroscopy. One challenge in studying 2D SAMs is the intrinsically small signal size due to the implicit monolayer nature of the system, thus few standard characterization techniques are sufficiently sensitive, and alternative approaches must be developed [42]. In particular, techniques such as NMR, DSC, and transmission infrared spectroscopy have usually only been applied to 3D SAMs with subsequent enhanced signal size. Furthermore, while molecular scale samples can be observed with scanning probe techniques, these techniques

provide primarily quasi-static data. Thus it is highly technically challenging to observe *dynamical* processes within 2D SAMs.

We employ our low frequency dielectric relaxation spectroscopy approach to observe molecular motion within well-characterized self-assemblies of surface-bound molecules attached to planar non-conducting substrates. By utilizing alkyls with an explicit dipole moment from a substituted terminal group or the small induced dipoles near the siloxane terminus, the alkyl chains are rendered dielectrically active.

As discussed in detail previously, dielectric spectroscopy measures the ability of dipolar objects within a sample to reorient in response to an applied electric field, by creating an observable electrical polarization, as a function of field frequency and sample temperature. In the most common "broadband" approach, a sample is placed between two macroscopic metal plate electrodes (previously referred to as "sandwich" type electrodes) and subjected to a wide range of frequencies (from 10^{-5} to 10^{7} Hz) at a single, fixed temperature, typically near ambient. Our technique differs from this method in two important ways. First, in order to increase sensitivity, a relatively narrow band of frequencies, centered about 1 kHz, is primarily used, wherein low-loss fused silica reference capacitors are available. Second, as a replacement for the macroscopic dual electrode configuration, basic lithographic patterning is used to create an array of interdigitated planar electrodes, restricted to a single flat substrate. The subsequent 2D SAMs are grown on the insulating surface in the regions between the metal electrodes. As mentioned, this technique is particularly

appropriate for these ultra-thin film measurements as the relative height of the electrodes versus the thickness of the monolayer results in a near-parallel electric field at the substrate surface. In addition, the fringing electric field penetrates into the spatial regions above and below the electrode plane. As noted earlier, this experimental technique can also be usefully applied to dynamical measurements of free standing, thin polymer films (or bulk samples, see Chapter 4), wherein confinement and surface induced effects to alter the observed glass transition temperature have been reported. This scheme has been used previously by Horansky el. al. to observe molecular rotors in a short, mixed monolayer film [49] and artificial molecular rotors in three-dimensional arrays [50,51].

5.2 Sample preparation

Organosilane monolayer film samples of varying coverage, alkyl chain length, and structure, were grown by either vapor- or solution-phase depositions onto the planar electrodes. Gold interdigitated electrodes on fused silica substrates, with 26 1 mm long finger pairs with equal spacing and width of 10 μm, were fabricated using standard uv-lithography. Alkyldimethylchlorosilanes with one reactive group for attachment to the surface and chain lengths of four to eleven carbon atoms are discussed in this thesis.

In particular, chlorobutyldimethylchlorosilane (C_4Cl (DM)), n-decyldimethylchlorosilane (C_{10}(DM)), and 11-bromoundecyldimethylchlorosilane (C_{11}Br(DM)) were utilized. Alkyltrichlorosilanes, which have three reactive groups and thus can form cross-linked films, with eleven, 11-bromoundecyltrichlorosilane (C_{11}Br), or

eighteen, octadecyltrichlorosilane (C_{18}), carbon atom chains were also utilized. Shorter chain molecules (trimethylchlorosilane TMS, chloromethyldimethylchlorosilane C_1Cl(DM), n-propyldimethylchlorosilane C_3(DM), and 3-cyanopropyldimethylchlorosilane $C_3C{\equiv}N$(DM)) were also measured as controls and will be discussed in more detail in a future report. Molecules were purchased from Sigma Aldrich (C_{18}) or Gelest and used without further purification. Prior to film growth, the sample planar electrode and a silicon test wafer were twice cleaned in a UV surface decontaminator for 30 minutes (exposed to oxygen for the first 10 minutes), rinsed with deionized water, and dried with nitrogen. Vapor-deposited films of C_{10}(DM), C_{11}Br(DM), C_{11}Br, and C_{18} were obtained by uniformly heating a covered, pre-silanated, pyrex deposition vessel containing the electrode and wafer to 90 °C for 30 minutes to reach thermal equilibrium. 20 μL of molecules were then added to the vessel and the film growth proceeded for a specified time interval. C_4Cl(DM) vapor-depositions followed the same procedure, but were performed at room temperature in a nitrogen-purged dry box (< 2% relative humidity). Monolayer samples of C_{11}Br were also fabricated in solution phase by immersing the wafer and electrode in 20 mL of toluene at ambient temperature in the dry box, then adding 20 μL of molecules. Sample coverage could be tuned from extremely dilute (sub-monolayer) to a complete monolayer by adjusting the length of time of the specific deposition. After film growth, the samples and test wafers were rinsed with methanol or toluene, sonicated in methanol or toluene, rinsed again with purified water, and blown dry with nitrogen gas. We note that subsequent film thickness measurements, by ellipsometry, showed that the initial alcohol rinse is sufficient to remove the majority of physisorbed

molecules from the surface; the sonication and additional rinsing step did not further reduce measured film thickness.

The thickness of the sample films was inferred by measuring the appropriate silicon test wafer accompanying each sample, using a commercial null ellipsometer with a 70° incident angle. The organosilane films were considered to have approximately the same index of refraction as the native oxide layer of the silicon (~1.462 [52]). Typically, 6 data points were taken at different spatial locations on the surface of the silicon test wafer before and after the deposition; the averaged difference between the ellipsometry measurements determined the genuine film growth. The system displays an intrinsic overall resolution of ±1Å, which corresponds to a minimum coverage estimate error of ±5% for a ~20 Å tall molecular film. In addition to ellipsometry, water contact angle measurements determined the wettability of the coated surface and atomic force microscopy (AFM) measurements at ambient conditions, with image sizes of 5x5 μm or smaller, revealed surface topography.

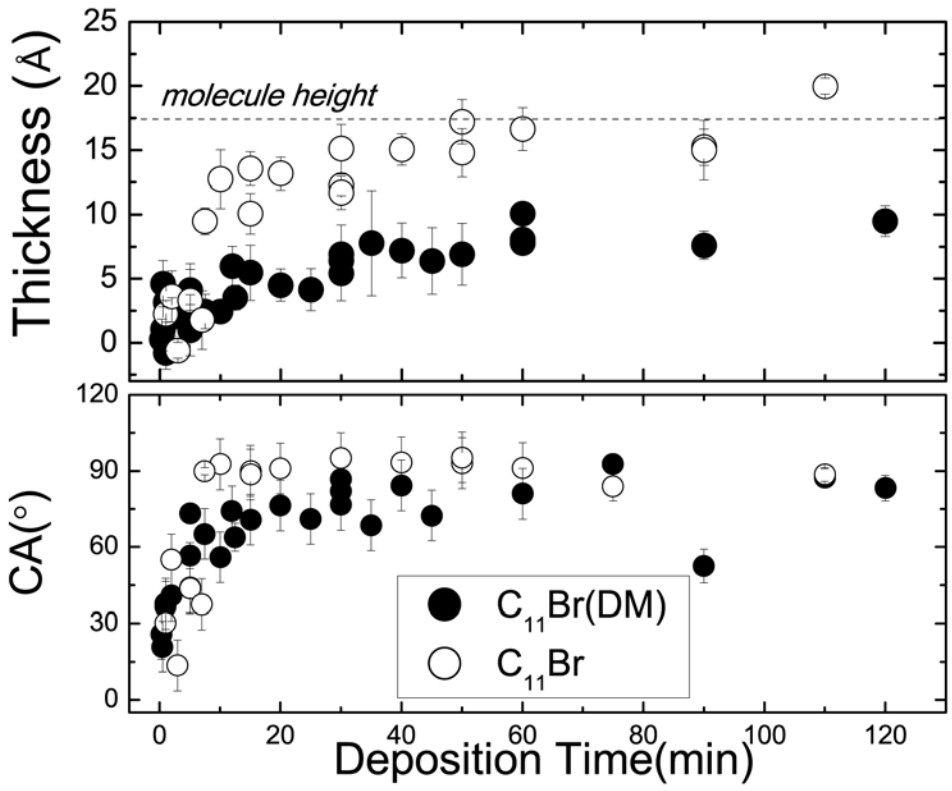

Figure 5.1: Comparison of vapor-deposited growth dynamics for monochlorosilane (C11Br(DM) and trichlorosilane (C11Br) molecules at 90 °C. (a) Ellipsometric measurements of film thickness versus time, where the labeled horizontal dashed line represents the maximum height of the molecule.

Figure 5.1 shows ellipsometry (upper (a)) and contact angle (lower (b)) measurements of vapor-deposition film growth curves for SAMs samples using precursor monochlorosilane C_{11}Br(DM) and trichlorosilane (C_{11}Br) molecules, respectively. (Figure 3.9 schematically depicts the structure of these molecules.) Literature value for the all-trans configuration height of the attached molecule is indicated by the horizontal dashed line in Fig. 5.1(a) [53].

As expected, alkylsiloxane monolayers fabricated from monochlorosilanes have a maximum coverage of ~55% of the all-trans molecular height due to steric hindrance of the methyl groups, whereas SAMs created from trichlorosilanes can form a complete coverage monolayer, which results in the full molecular height as measured by ellipsometry [53]. AFM measurements show a surface variation of ±2 Å on the native silica oxide layer formed on a blank silicon test wafer; subsequent measurements on sample test wafers for vapor-deposited alkyl siloxane films grown to varying coverage resulted in similar variation, suggesting that vapor-deposited films grow homogeneously to form the SAM film. Both visual and quantitative analysis of AFM images reveal a homogeneous surface with no features. This growth pattern is in contrast to solution phase depositions, which typically create SAMs by islanding mechanisms [43].

5.3-Dielectric Results and Discussion

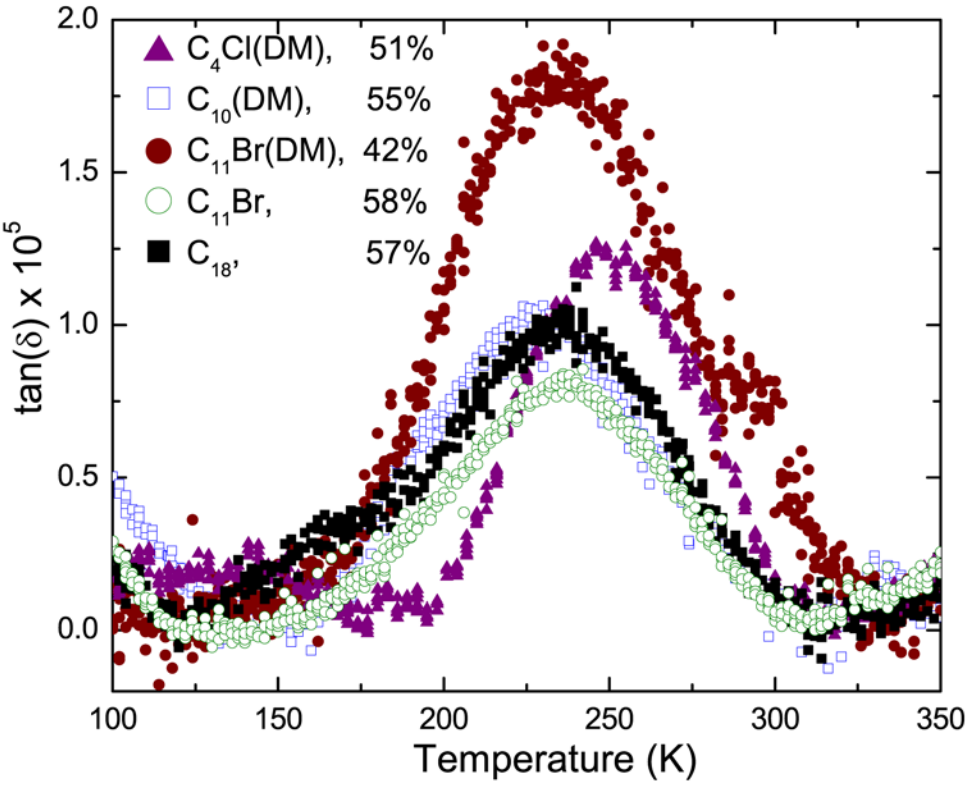

Figure 5.2: Varying the chain length: Films grown from molecules having 4-18 carbon atom chain lengths show a dielectric relaxation at ~235 K at 1 kHz measurement frequency: C_4Cl (purple triangles), C_{10}(DM) (black squares), $C_{11}Br$(DM) (red circles), $C_{11}Br$ (green circles), and C_{18} (blue squares). The error on coverage is ± 8%. Raw data points consisting of 5 measurements at each temperature are shown; resultant point error is typically smaller than the graphed data symbols size.

Figure 5.2 shows tan(δ) versus temperature for film samples vapor-grown at 90 °C with ~60% coverage or less**.** Each sample has had a linear background subtracted (slope < $5x10^{-8}$ tan(δ)/K) due to ionic conductivity. First, focusing on the result for $C_{11}Br$(DM) (solid circles), a dielectrically-active relaxation at ~235 K is evident. Aside from a well-known

feature due to the fused silica substrate [54] which appears at ~25 K (below the range displayed in Fig. 2), no additional relaxations are observed over the temperature span of 10-400 K, which is equivalent to a 0.5 to 60 kJ/mol range of barriers (assuming Arrhenius dynamics and $\omega_o = 10^{13}$ rad/s). The single sweep of a $C_{11}Br(DM)$ film shown is representative of ~20 samples and ~57 individual experimental measurements at 1 kHz frequency on SAM samples at densities < ~55% coverage measured over a period of six months. C, the capacitance due to the reorienting dipoles (Eq. 2.47) can be determined by fitting a superposition of Debye peaks (Eq. 2.7) to the observed data. Such an amplitude analysis shows that the size of the dielectric relaxation is in good agreement with the estimated coverage from ellipsometry giving an effective dipole moment of about 1.3 D, which falls between the estimates for an induced dipole near the siloxane linkage (~0.7 D) and the 1.8 D dipole expected for a bromomethyl group.

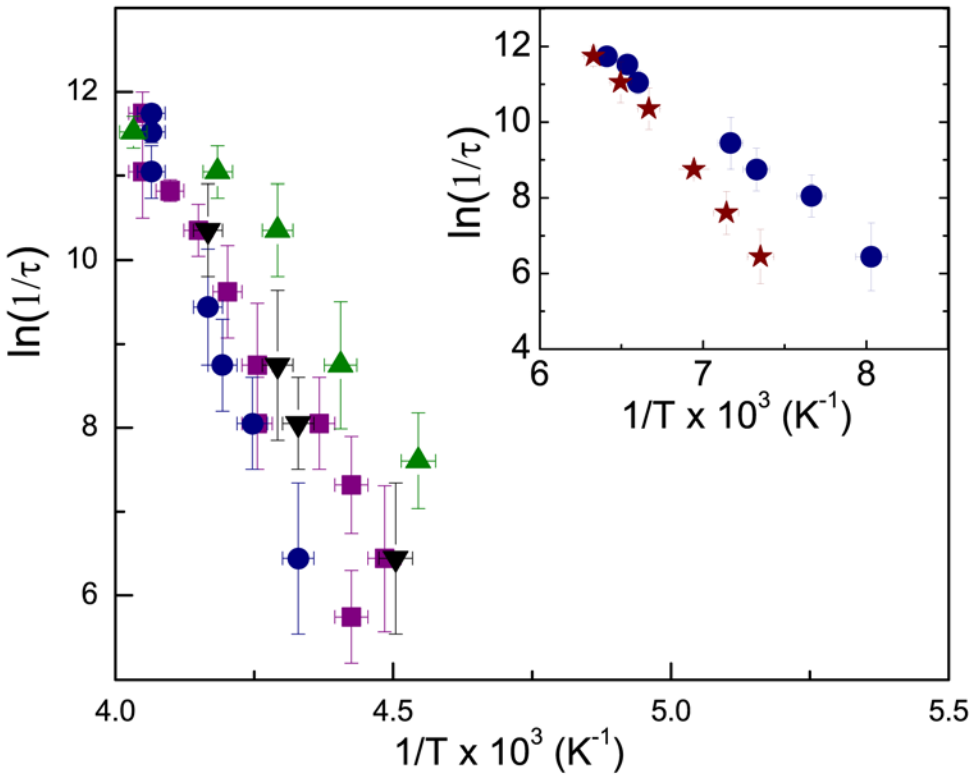

Figure 5.3: Arrhenius plot of ln(1/τ) versus (1/T). Data from the ~235 K interacting relaxation is plotted for $C_{11}Br$ (DM) samples of 19% (upright green triangles), 42% (purple squares), and 49% (inverted black triangles) coverage and a 99% coverage $C_{11}Br$ sample (blue circles). Inset: Corresponding ~150 K lower temperature relaxation from the 99% coverage $C_{11}Br$ sample (blue circles) and a 55% $C_{11}Br$ (DM) sample (red stars). The error in the coverage is ±8% for all samples.

The dynamics of the 235 K relaxation as a function of temperature for the same $C_{11}Br$(DM) sample are shown (purple squares) in Figure 5.3. Two other samples of similar coverage are also plotted. Fitting the data with an Arrhenius form yields an artificially high apparent attempt frequency $\ln(\omega_o)$ ~70, revealing a cooperative motion. A VFT analysis

yields a T_o of 136 K. Both the VFT and Arrhenius plots are virtually linear over the relatively narrow frequency range measured. Extrapolating the VFT fits yields T_g = 198 ± 12 K by averaging results from 12 samples on which multi-frequency measurement temperature sweeps were taken. The estimated steepness index, m, for this relaxation is 26 ± 7.

In order to most effectively elucidate the origin of this relaxation, low-density samples grown from other alkylsilane molecules with differing chain lengths were measured, the results of which are also shown in Figure 5.2. Samples in this sequence possessed chain lengths varying from 4 to 18 carbon atoms; in addition, both mono- and trichlorosilanes were utilized in order to create films both having and lacking the ability to cross-link. Most films in this survey were generated at elevated temperatures from vapor-phase, with the exception of C_4Cl(DM) as noted in Methods section following. Finally, molecules with and without an explicit terminal dipole were also investigated.

Previously, a broadband dielectric spectroscopy study of alkylsiloxane films, with and without explicit dipoles, grown on highly porous silica has been reported, concluding that the alkyl bonds closest to the silicon atom were polarized, resulting in a small net dipole and enabling the SAM to be dielectrically active [48]. We confirm this effect here by our observations shown in Figure 5.2, as both polar (explicit dipole) and nonpolar (no explicit dipole but an induced dipole near the siloxane linkage) films display a similar dielectric relaxation. In comparing signal size, C_{11}Br(DM), C_{11}Br, and C_{10}(DM) showed similar effective dipoles, which indicates that the dipole for the reorienting segments within the

$C_{11}Br$ samples may result from either an induced dipole near the surface (similar to that in the C_{10}(DM)) or the net effect of a permanent dipole (~1.8 D for a bromomethyl) counter-aligned with the induced dipole. C_{18} signal sizes were systematically smaller, at high coverage, than explicitly polar molecules; this may indicate a greater level of ordering, reducing the number of molecules free to reorient, or a smaller induced dipole in the C_{18} case. These observations with respect to amplitude are consistent with those previously reported [48]. In contrast to the longer chain films, samples with an alkyl chain less than four carbon atoms in length (TMS, C_1Cl(DM), C_3(DM), $C_3C{\equiv}N$(DM)) typically showed either no distinct relaxations, or relaxations significantly shifted toward lower temperature as compared with the relatively constant peak position of ~235 K observed in films composed of molecules with alkyl chains 4 - 18 carbon atoms in length. Relaxations in shorter films will be the subject of another detailed report. Although a careful examination of the data indicates subtle systematic changes in the dielectric spectra as a function of molecule type, dipole moment, coverage, preparation conditions, and thermal history, in this publication, we focus on the underlying *fundamental* relaxation common to all these *long* chain films. Considering measurement of all 22 samples of the various longer chain molecular species, T_g = 200 ± 11 K and m = 27 ± 7. We note that this collection of samples is heavily weighted towards the 11 carbon atom chain length due to the samples used.

Extensive research has been conducted on dynamics within polymers containing alkyl-side-chains, which shed light on the monolayer alkyl relaxations observed here. In particular, for alkyl-side-chain polymers, where the side-chains are phase separated, two

distinct glass transitions have been reported [47]. One glass transition is consistent with the backbone relaxation and thus specific to the polymer type; whereas the other has been assigned to cooperative motion of the alkyl chains themselves, having only a weak dependence on backbone type. The authors identified this relaxation as polyethylene-like (PE-like) and observed a change in T_g of this α_{PE} as a function of chain length, due to the change in the size of the phase segregated domains. The location of the α_{PE} relaxation was ~230-250 K in the 1 kHz to 10 kHz range for a C_{10} chain, which is consistent with our observations. As chain length decreased, the domain size became smaller, which was associated with a shift in T_g toward lower temperatures (faster dynamics) and a decrease in fragility. At C_4, the relaxation had Arrhenius dynamics (m = 16). For C_{11}, m was approximately 37 and approached the PE value of m ~50 at chain lengths greater than 16 carbons. PE is a semi-crystalline polymer and thus its T_g varies with degree of crystallinity; however the results from side-chain polymers are consistent with PE values of T_g = 190 K for amorphous PE and T_g = 260 K for amorphous regions bound by crystalline material [46].

These observations in polymers provide insight into the dynamics within the current system, and match well with dielectric relaxation peaks observed with C_4-C_{18} chain lengths; in particular, the estimated T_g for our films is consistent with that of amorphous polyethylene, with a similar steepness index as observed for the polyethylene-like glass transition within side-chain polymers. However, there are several distinct differences between our samples and the equivalent side-chain polymers or neat polyethylene. In SAMs samples, the substrate

is similar to an extremely rigid backbone in a polymer system. Unlike a linear polymer, the substrate does not bend to allow phase segregation and the molecules are constrained to a two-dimensional sheet. Phase segregation may occur if small islands of molecules were formed; however, the size of these islands would have to be on the order < 1 nm (a few molecules) in order to constrain the dynamics as seen in the polymer case. Thus phase segregation should play a reduced role. In limited studies we found that *m* increased with density, as expected when molecule-molecule interactions increase in the low density regime. On the other hand, an alkylsiloxane SAM is also quite different than bulk PE, because translational motion is strongly quenched from physical attachment to the surface. Thus, we do not expect to recover exactly the dynamics of either prototype system (alkyl-side-chain polymers or bulk PE). However, an analogous PE-like glass transition provides a reasonable hypothesis to explain these compelling dielectric observations.

As discussed above, most alkyl 2D SAMs reported in literature can be described as solid-like, having high density, usually close to the maximum packing density possible for alkyl chains of 18 $Å^2$ [55], and few gauche defects. These samples should be remarkably similar in nature to a single layer of a bulk alkane solid. Above the melting point of the alkane, densely packed samples become more liquid-like with the introduction of gauche defects at one or both ends of the chains. In order to create a liquid-like sample at room temperature, a lower density of molecules is necessary, allowing a significant number of gauche defects. Islanding, which depends on film deposition conditions and increases with chain length, must also be prevented. In fact, as discussed above, we specifically designed

our fabrication technique towards formation of liquid-like monolayers. This was accomplished by utilizing vapor-phase depositions at an elevated temperature, and using silanes with bulky dimethyl groups, in order to prevent effective packing. This was done in an effort to maximize the types of motional dynamics available to the alkyl chains. In order to display amorphous PE-like dynamics, the samples must be within the liquid-like regime, where chains are not ordered, at a distribution of tilt angles or in some manner lying down on the surface, and have a high density of gauche defects. In this environment, an ethyl group within the alkyl chain exists in a "soup" of other ethyl groups from neighboring chains, with little change in dynamics as a function of chain length. As discussed above, morphological studies support this assignment of our vapor-deposited films as liquid-like. In contrast, samples fabricated by room temperature solution phase deposition of $C_{11}Br$ exhibit island formation and display a shift in peak position toward lower temperatures and significant sharpening of the PE-like peak, not discussed in this thesis.

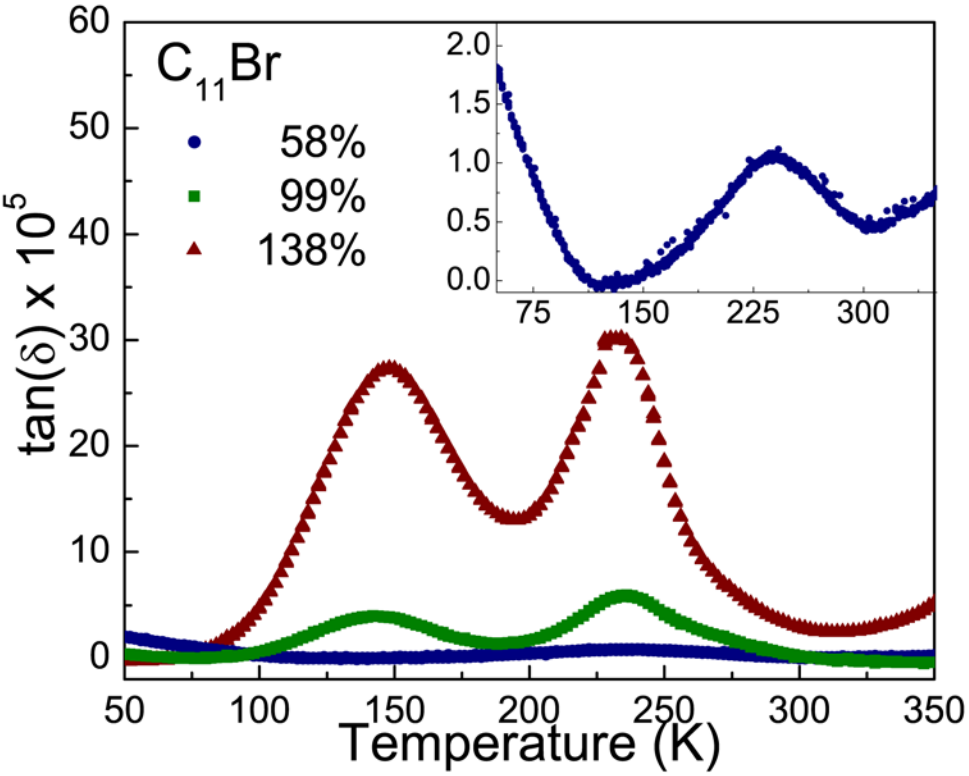

Figure 5.4: Varying the coverage for $C_{11}Br$ SAMs: Dielectric relaxation at 1 kHz for films at sub-monolayer (58%, blue circles), monolayer (99%, green squares), and slight multilayer (138%, red triangles) coverage. All films display a peak at ~235 K; as coverage increases, a second relaxation at ~150 K also appears. Inset: an expanded view of the 58% $C_{11}Br$ SAM showing only the ~ 235 K relaxation. Raw data points consisting of 5 measurements at each temperature are shown; resultant point error is typically smaller than the graphed data symbols size. The error in the coverage is ±8% for all samples.

In order to further explore the relaxations within alkyl SAMs, we measured film samples with higher surface coverage. Whereas the maximum coverage of alkyl monolayers fabricated from monochlorosilane precursor molecules is limited to ~55% [53], due to steric hindrance from the methyl groups, trichlorosilane molecules can obtain higher coverage and

potentially, a more ordered film. In general, for higher density coverage SAMs, including the highest density C_{11}Br(DM) obtained, a second relaxation at a lower temperature is observed. This relaxation was seen in C_{18}, C_{11}Br(DM), and C_{11}Br, at coverage > ~55%. Figure 4 shows a sequence of C_{11}Br SAMs grown from the vapor-phase above room temperature. For the lowest coverage (~58%), only the 235 K relaxation is seen (see inset, Figure 5.4). As coverage increases (~99%), the 235 K peak gains in amplitude and a second relaxation appears at ~150 K. Escalating coverage further to the range of slight multi-layering (average sample height 138% of an all trans-chain) results in no additional relaxations but increases the existing peak sizes. Figure 5.5 shows data for the 99% coverage sample at several frequencies to display shifting of the two peaks with frequency. This data is also expressed in the Arrhenius form in Figure 3. Unlike the interacting dynamics of the higher temperature relaxation, the ~150 K relaxation displayed Arrhenius dynamics, and a barrier E_b = 29.7 ± 3.8 kJ/mol, an average value resulting from 8 samples.

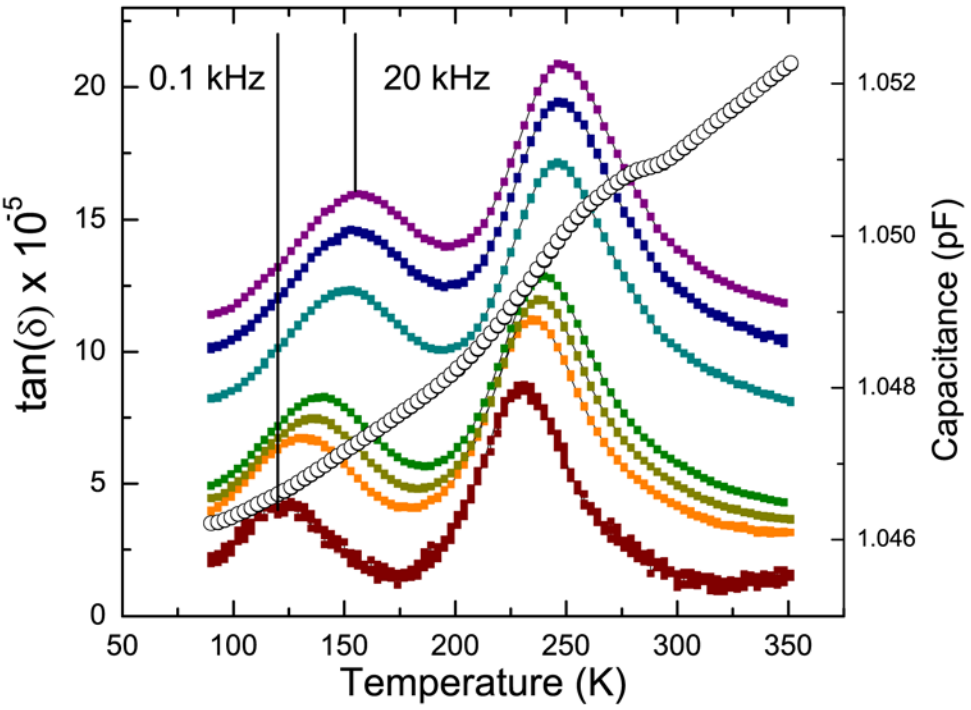

Figure 5.5: Dielectric spectroscopy of a full coverage (99%) $C_{11}Br$ SAM. Loss (left axis, tan(δ)) measured with applied frequencies of 0.1, 0.5, 1, 2, 10, 16, and 20 kHz as a function of sample temperature. Representative vertical lines at 0.1 and 20 kHz are drawn at each lower temperature maximum, respectively, to aid the eye in demonstrating the dispersive nature of the relaxation. Raw data points consisting of 5 measurements at each temperature are shown; resultant point error is typically smaller than the graphed data symbols size. The corresponding step-wise change is shown in the capacitance for 1 kHz (right axis (open circles)).

We compare our results in this coverage regime to a recent report of broadband dielectric relaxation spectroscopy on siloxane SAMs grown on porous glass powders [48]. In that work, samples of C_{18} fabricated by solution phase at relative coverage of 51-80% display a relaxation with effective activation energy of ~25 kJ/mol. The authors connect this

relaxation with the known γ processes in PE, such as trans-gauche reorientations and the rotation of short chain segments. Equivalent localized relaxations are also present in alkyl-side-chain polymers, with side-chains greater than four carbon-atoms in length, as was first reported in the early 1970's. In particular the γ relaxations in alkyl side-chain polymers follows Arrhenius dynamics and have barriers that range from 23 - 37 kJ/mol [28,56,57] consistent with our observations and those previously published [48].

5.4-Conclusions

In summary, we demonstrate the ability to observe dynamics within dilute chemisorbed monolayers via a novel dielectric spectroscopy approach with sufficient sensitivity to utilize the induced dipole in a functionalized alkyl chain as a marker of motion. Over a range of coverage from ~10% to slight multilayers, for molecules with chain lengths of 4 - 18 carbon atoms, and in the presence and absence of cross-linking, we observe a cooperative relaxation, which has the characteristics of a polyethylene-like glass transition. Samples for these studies were fabricated from vapor-phase at elevated temperature in order to deliberately generate liquid-like, disordered films. As coverage increases, a second, local relaxation, with similar dynamics and barrier to a γ relaxation in polyethylene is also observed. This relaxation may result from a reduction in the number of gauche defects as the packing density increases and chains are forced to straighten, providing four-carbon segments that are primarily in a trans configuration.

Chapter 6-Glassy dynamics in SAMs

6.1-Introduction

Alkylsiloxane monolayers consist of unsaturated hydrocarbon chains of varying length covalently bound to a flat substrate. The structure of the monolayers has a similarity to alkyl side-chain polymers in that the crosslinked bases (the siloxane) of the molecules form a sheet near the surface with the alkyl groups emerging from this quasi-two-dimensional backbone. Even without crosslinking, the rigid substrate supports the alkyl groups in an analogous fashion. Previous work has studied relaxations in alkyl-side chain containing polymers and concluded that a complex relaxation, associated with segregated regions of alkyl chains and relatively independent of the backbone type, was analogous to the glassy dynamics observed in polyethylene (PE) [47]. This relaxation was denoted as PE-like and the fragility was studied as a function of chain length, which alters the alkyl-chain domain size. We have previously observed a similar relaxation in alkyl monolayers (See Chapter 5).

As discussed previously, a key advantage of the monolayer system approach over conventional bulk samples is that the molecules' translational motion is suppressed by the covalent bond(s) to the surface and thus, the sample density can be explicitly varied via film growth to tune the monolayer coverage from highly dilute (area per molecule ~300 $Å^2$) to complete coverage (~ 20 $Å^2$ per molecule) . This is in contrast to temperature- dependent measurements of bulk polymer samples, where density changes occur spontaneously. The

goal of this study is to examine dynamics, particularly the PE-like relaxation, as a function of molecular density. Specifically, we wondered if we could observe a transition from Arrhenius-like dynamics at low coverage to glassy dynamics as the coverage increased, and if the fragility of the relaxation increased with density within the interacting regime. Although clearly, this relatively short-chain (eleven ethylene groups) system is not directly analogous to a much more complex glassy polymer, it may serve as a simplified experimental model to further scientific understanding of the glass transition in a similar wayas the transition from a plastic crystal to an orientational glass [5].

6.2- Sample preparation

Samples with variable sub-monolayer coverage were prepared using the organosilane precursor molecules of 11-bromoundecyldimethylchlorosilane (C_{11}Br(DM)) or 11-bromoundecyltrichlorosilane (C_{11}Br) (Gelest, Inc.), vapor deposited at 90°C onto flat fused silica substrates as discussed previously. Sample coverage was controlled by varying deposition time. The sample film thickness was taken as equal to that of a silicon test wafer placed in the deposition environment next to the sample as measured using a commercial null ellipsometer with a 70° incident angle. Coverage was estimated as the observed film thickness divided by the expected height of the all-trans conformation of the molecule, in this case 17.38Å [53]. The surface morphology of the film was further probed by water and squalane contact angle measurement and atomic force microscopy (AFM). Water contact angle measurements show a saturation curve similar to that obtained from ellipsometry,

while squalane contact angle measurements indicate that the alkyl-terminated films are highly disordered [58]. AFM measurements indicate that the vapor-phase deposited alkylsiloxane films grow uniformly (as opposed to via islanding mechanisms which typically occurs in solution-phase film deposition [43,58]). Surface roughness values, as measured by AFM, for sample films were typically identical to that of the blank substrate, less than ±2 Å.

Alkylsiloxane monolayers spontaneously form on hydroxylated surfaces, such as fused silica, via a condensation reaction [53]. C_{11}Br(DM) has only one reactive group, and thus will form a single bond to the surface via reaction with a surface OH group; C_{11}Br has three reactive groups and can crosslink by reacting with either a surface silanol or with neighboring molecules [52]. Due to the single available chemical bond attachment point, the C_{11}Br(DM) samples are unable to form multi-layer films. In addition, these molecules self-saturate at a maximum surface density of ~55% of the full coverage trichlorosilane monolayer, due to steric hindrance by the bulky methyl group [53]. In contrast, the C_{11}Br films can cross-link and span the complete range from extremely dilute to 100% full coverage regimes. Care is taken to avoid growth conditions that results in vertical polymerization (i.e., multi-layer formation).

6.3- Dielectric Results

Raw dielectric relaxation spectroscopy data versus temperature for C_{11}Br and C_{11}Br (DM) films of varying coverage taken at 1 kHz applied frequency are shown in Figure 6.1.

Varying the film surface density from low coverage (6.9%) to moderate coverage (65%) generally results in an increase in the measured tan (δ) peak amplitude, as well as a shift in peak location toward higher temperatures (which reflects slower dynamics within the film). The peak location (at 1 kHz) shifts from about 200 K to 240 K as coverage is increased from ~ 10% to 90%.

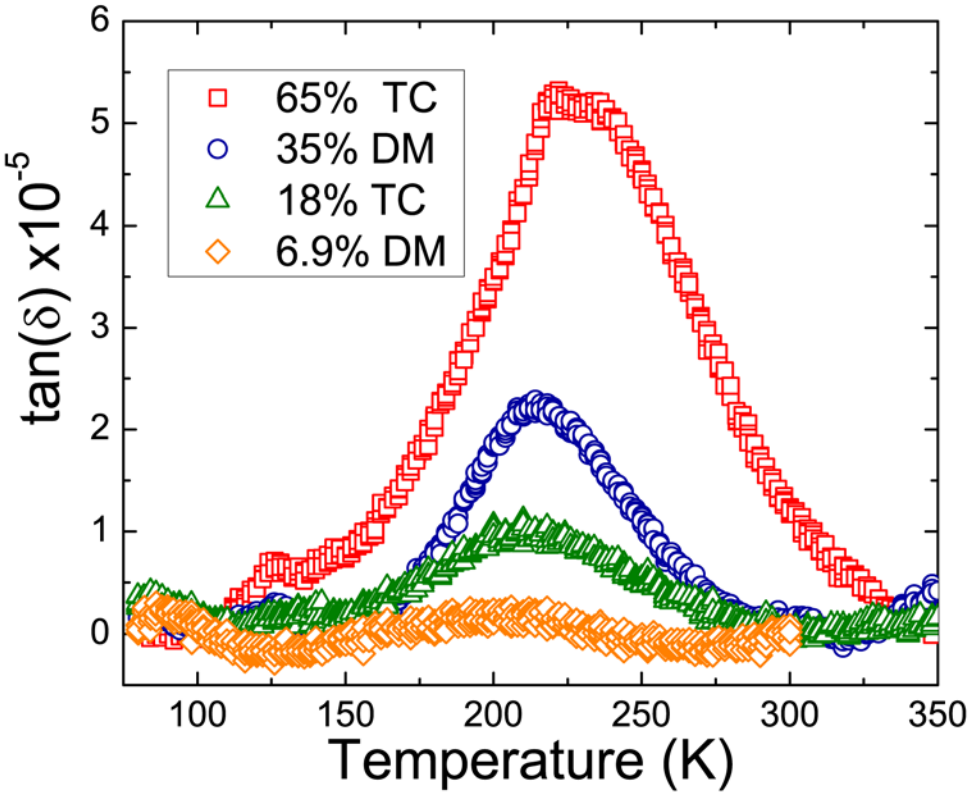

Figure 6.1: Dielectric spectra at 1 kHz for $C_{11}Br$ at 65% coverage (open squares), $C_{11}Br$ at 18% coverage (open triangles), $C_{11}Br$ (DM) at 35% coverage (open circles), and $C_{11}Br$ (DM) at 6.9% coverage (open diamonds). In the legend, TC designates trichloro (three feet) and DM designates dimethyl (single foot).

Arrhenius plots for C11-Br samples of density varying from ~ 5% - 99% are shown in Figure 6.2. The lowest density sample (<10% coverage) is consistent with a non-interacting Arrhenius behavior with a barrier of 9.4 ± 2.2 kcal/mol and a physical attempt frequency of ~10^{14} rad/sec. As the density increases (from red to blue), the center of the plot shifts to higher temperatures (lower 1/T), reflecting slower dynamics. Furthermore, the slope of the curve increases, which indicates a more dramatic change in dynamics with temperature. This, particularly observation of an artificially-high apparent attempt frequency, is generally an indication that the system exhibits cooperative motion and is more appropriately fit by VFT. As the density increases, we observe that the slope increases significantly, much more than expected from the temperature shift of the peak, indicating that the dynamics are both slowing and becoming more cooperative. We can quantify these observations by calculating the T_g (τ = 100 s) and *m*, steepness index, for each sample (Figure 6.3 and 6.4 respectively).

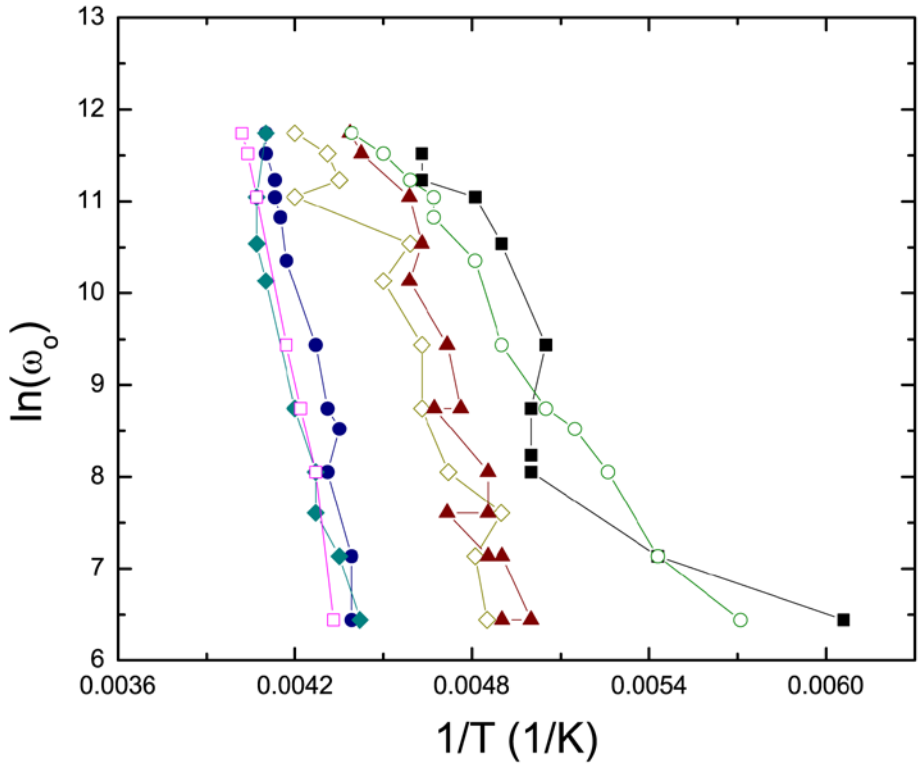

Figure 6.2: Arrhenius plot for $C_{11}Br$ samples of varying coverage: 5.5 % (filled squares), 41% (open circles), 75 % (filled triangles), 23 % (open diamonds), 63 % (filled circles), 99 % (open squares), and 78% (filled diamonds).

Calculating T (τ = 100 s) for all samples indicates an increasing trend with density, as shown in Figure 6.3. There are three important regions: At low coverage (<10%), the behavior is close to Arrhenius, with an apparent attempt frequency of < 10^{15} rad/sec. If fit with the VFT form T_o, the Vogel temperature is less than 20 K again indicating that we are not in a glassy regime. These points are not shown in Figure 6.3 as it is inappropriate to assign a T_g for such a relaxation however their T (τ = 100 s) = 120-140 K. As the density

increases (20-60%), we observe T_g values centered around 150-160 K, independent of coverage within our error values. Finally, as the density increases above 60%, we observe a transition to higher values with T_g = 210 K at the highest coverage.

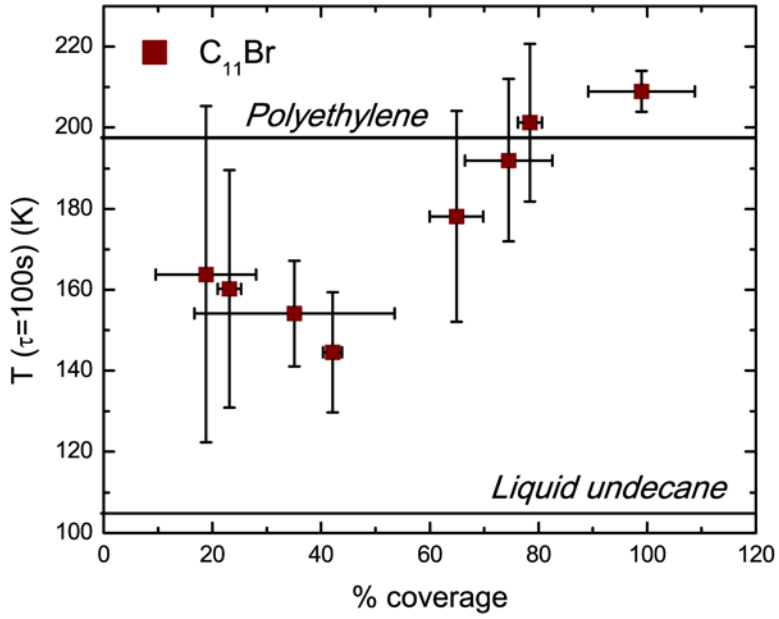

Figure 6.3: Glass transition temperature as determined by VFT fits for $C_{11}Br$. As a reference point the glass transition temperature for polyethylene and liquid undecane are indicated by their respectively labeled horizontal lines.

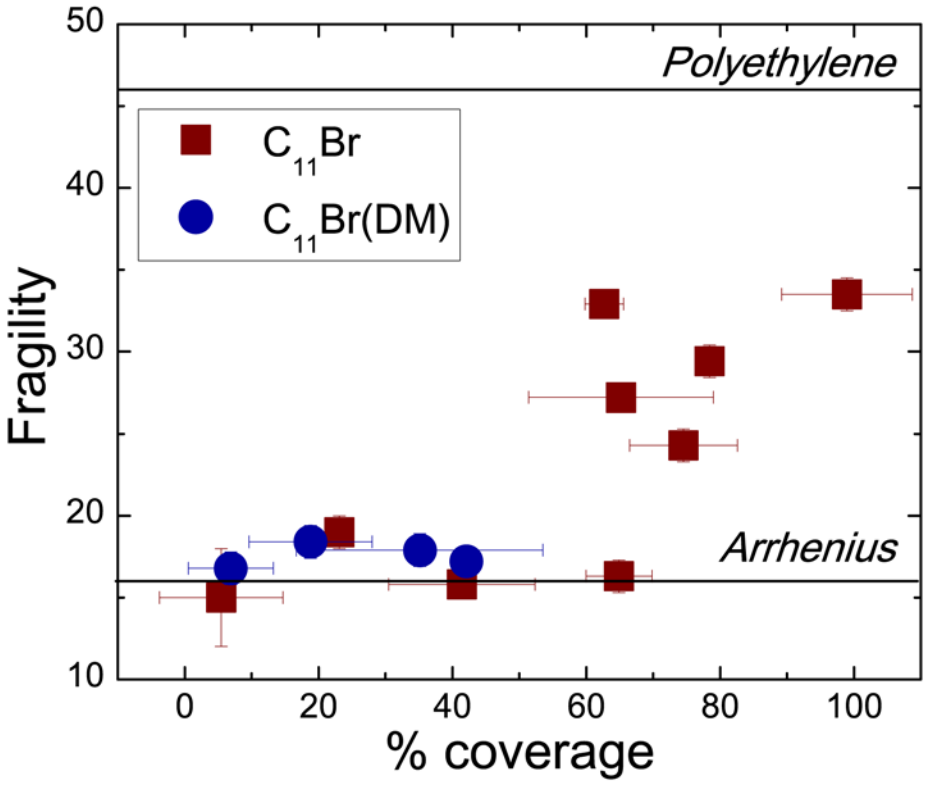

Figure 6.4: Plot of the fragility (m) for various densities of $C_{11}Br$ and $C_{11}Br$ (DM)

Higher coverage samples have T_g values near to that of polyethylene given in the literature (190 K, amorphous, 210 K, semicrystalline [59]. We note that the points at 65% and 75% each reflect two distinct samples. In both of these cases, one of the two samples exhibited behavior consistent with region 2 (T_g ~155 K), whereas the other, at similar coverage, had a significantly higher T_g and *m* (see below). This is an indication that rather than a smooth continuous increase, a somewhat discontinuous change occurs at 60-70% where the T_g of the system increases by ~50 K. The plot of fragility (Figure 6.4), shows a

similar trend. All samples below 50% show a low *m* (less than 20), which is consistent with either Arrhenius behavior or that of a strong glass. In the 50-70% range, switching between this state and much more cooperative relaxation is observed, and finally, above 80% all samples are clearly cooperative. Further insight into the mechanisms at play here can be gained from an examination of the full-width half maximum of each sample. Full-width half maximum analysis (Figure 6.5) indicates that with increasing film density, a more uniform distribution of energetic barriers is found within the film.

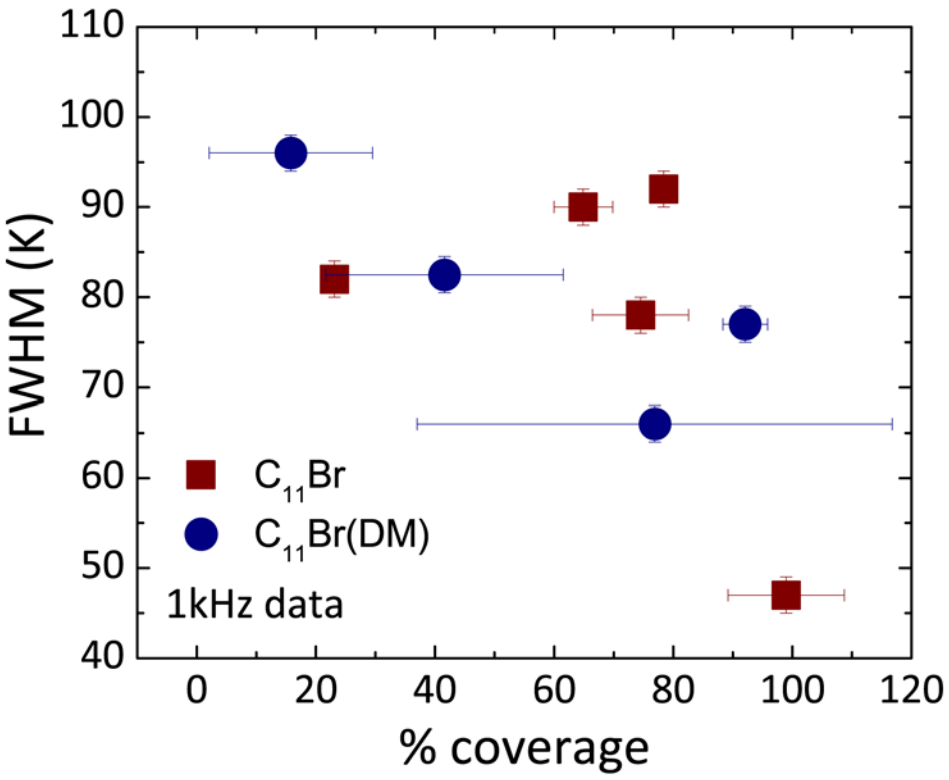

Figure 6.5: Full-width half maximum plot for $C_{11}Br$ and $C_{11}Br$ (DM) at 1 kHz. The x-axis in this plot designates relative coverage for the $C_{11}Br$ (DM) data. It is the percentage with respect to the maximum coverage obtainable for the $C_{11}Br$ which is ~ 55%. For $C_{11}Br$ the x-axis is the coverage as normally presented in this thesis as percent relative to the molecular height.

6.4-Discussion

Three factors influence the local density within the monolayer system: the number of molecules (measured here as the areal coverage), the average molecular tilt angle within the film, and the presence or absence of gauche defects, which will affect the packing within the

film. In this long chain system, at low density, the molecules, particularly the non-crosslinked $C_{11}Br$ (DM), are expect to have significant freedom to tilt with respect to the surface normal. Significant tilting would also enable neighboring molecules to interact, even at very low coverage. (For a coverage of 10%, the area per molecule is ~200 $Å^2$, yielding a center-center distance of 8 Å, similar to the length of the molecule). As areal coverage is increased, the system is likely to maintain local density by decreasing the tilt angle (bringing the molecules are close to normal). This "expandability", as described in the previous sentence, of the system will decrease as the density increases and we expect that local density should still be well-tied to areal coverage. For both types of molecules we find little change in the dynamics from ~10% to 60% areal coverage. This result may be specific to this system, due to the ability of the monolayer to maintain local density by decreasing the tilt angle.

The barrier obtained from the Arrhenius fits for samples with *m* ~16 varies from 9 kcal/mol to 11 kcal/mol. This level is higher than the activation energy associated with rotation about a single bond in polyethylene, which is ~14 kJ/mol= 3.3 kcal/mol [60]. There are two known relaxations in amorphous polyethylene. The first is a local (γ) relaxation, which exhibits Arrhenius dynamics with a barrier generally in the 6-7 kcal/mol range. This relaxation has extensively been observed in side-chain polymers [47] and by our group and others [48] within self-assembled monolayers, particularly above a sufficient density (>60%-70%) (see Chapter 5). The specific mechanism for this relaxation is still under debate within the community, however it is generally associated with coupled rotations (resulting in little or

no volume change) around the axis of the alkyl chain [28,29]. At 1 kHz, this relaxation appears at ~160 K. The second relaxation in amorphous PE is that associated with the glass transition, which occurs at a higher temperature and is strongly cooperative. In this experiment, we observe a relaxation that first occurs at ~200 K, at a higher temperature and barrier than the γ-like relaxation (indicating slower dynamics), and transitions upward in temperature, becoming more interacting, as the density increases, finally arriving at the temperature location of the αPE (PE is polyethylene) seen in side-chain polymers. At our highest density, the T_g of our monolayer system is similar to that of previously reported for PE [61]. These results are consistent with Boyd's computational study of polyethylene dynamics which showed a transition from Arrhenius dynamics to VFT dynamics when comparing an isolated chain to bulk PE [62]. Thus our system offers an experimental opportunity to explicitly observe the development of glassy dynamics as the density increases.

In general, theoretical studies have considered the polyethylene (or equivalently the PE-like) glass transition and the γ-relaxation to arise in different ways from the same basic trans-gauche rotation within the alkyl chain. Previously Beiner studied alkyl-side-chain polymers where the side chains were phase segregated in domains [47]. As chain length, and thus domain size decreased, he observed a transition from interacting to local behavior, and hypothesized that the system was extrapolating from the bulk glassy dynamics of polyethylene (at infinitely large domain size/chain length) to the local γ relaxation under

significant confinement (chains with less than 4 carbons). The role of chain length in Beiner's studies was to tune the confinement of the system or to limit the number of segments that could interact cooperatively. In the work reported here, we tune the degree of interaction by tuning the density. The density and confinement effects are different and thus we do not expect the same results as in Beiner's work. However we do also observe a transition from non-interacting to cooperative dynamics. In particular, our data are consistent with a picture where at low density the intrinsic barrier to rotation about a single bond is raised by extrinsic interactions with other molecules. The barrier we observe for low density is slightly higher than that of the γ-PE relaxation, which only occurs at higher density (See Chapter 5). As the density increases, motion of molecular segments becomes more difficult (raising the barrier) and more cooperative (requiring correlated motion between neighboring groups). At the highest densities an additional peak at the location of the γ-PE is also observed. This could represent a subset of the segments that previously contributed to the α-PE, which are now constrained by local density (essentially a splitting of the original peak). Alternatively, the γ-PE could results from single bond rotations (which would be lower in temperature than our most common temperature range) which subsequently increase in barrier with density, and now are visible in our spectrum. This issue is under further study in our laboratory.

Both the *m* and T (τ = 100 s) analysis indicate that the SAM becomes *more interacting* as the overall density is increased. The fragility also indicates that this is not primarily due to crystallization within the film at higher density, as the effect of this physical

morphological change would actually *lower* the fragility [63] by acting to confine the remaining amorphous regions between crystalline domains.

In our system, the steepness index, *m*, undergoes a transition from ~16-20 to ~35 beginning at ~60% areal coverage. This is a transition from a strong to a fragile glass. Our current data is insufficient to definitively distinguish between a sigmoidal shape where the fragility saturates as a particular value or a linear increase without limit, if the density could be further increased. Although as we discussed above, the specific location of 60% areal density may reflect the ability of our monolayers to maintain density by decreasing tilt angle, we nonetheless point out that in a random continuum percolation model (such as has been previously applied to glassy systems [64]) percolation occurs at 60-70% in a two-dimensional system. From a percolation perspective, at this point the objects in the system become connected.

6.5- Conclusion

In summary, we have characterized the dynamics of 11-bromoundecyldimethylchlorosilane (C_{11}Br(DM)) and 11-bromoundecyltrichlorosilane (C_{11}Br) at various densities. Increasing the density resulted in the peak in tan(δ) to become larger in amplitude as well as shifting toward a higher temperature. Generally, there is an increasing trend for the T (τ=100 s) with density. For moderate densities T_g values are in the range of 150K – 160K and then T_g increases to 210 K at the highest density. The fragility is similar with an increase occurring for samples above 60% coverage. We have observed

density dependent glassy dynamics in films consisting of surface bound trichlorosilanes and these dynamics have been related to similar relaxations seen in polyethylene.

Bibliography

[1] H. J. C. Berendsen, J. P. M. Postma, W. F. van Gunsteren, DiNola A., and J. R. Haak, J. Chem. Phys. **81**, 3684 (1984).

[2] R. Car and M. Parrinello, Phys. Rev. Lett. **55**, 2471 (1985).

[3] J. Michl, ACS Nano **3**, 1042 (2009).

[4] G. S. Kottas, L. I. Clarke, D. Horinek, and J. Michl, Chem. Rev. **105**, 1281 (2005).

[5] M. Jimenez-Ruiz, M. A. Gonzalez, F. J. Bermejo, M. A. Miller, N. O. Birge, I. Cendoya, and A. Alegria, Physical Review B **59**, 9155 (1999).

[6] J. A. Crowe-Willoughby and J. Genzer, Advanced Functional Materials **19**, 460 (2009).

[7] R. H. Cole, J. Chem. Phys. **23**, 493 (1955).

[8] D. W. Davidson and R. H. Cole, J. Chem. Phys. **19**, 1484 (1951).

[9] P. A. Miles, W. B. Westphal, and A. Vonhippel, Reviews of Modern Physics **29**, 279 (1957).

[10] V. V. Daniel, *Dielectric Relaxation* (Academic Press, New York, 1967).

[11] H. Frohlich, *Theory of Dielectrics* (Oxford University Press, London, 1952).

[12] H. Eyring, J. Chem. Phys. **3**, 107 (1935).

[13] G. Fulcher, J. Am. Cer. Soc. **8**, 339 (1925).

[14] G. Tammann and W. Hesse, Zeitschrift Fur Anorganische Und Allgemeine Chemie **156** (1926).

[15] H. Vogel, Physikalische Zeitschrift **22**, 645 (1921).

[16] N. G. McCrum, B. E. Read, and G. Williams, *Anelastic and Dielectric Effects in Polymeric Solids* (Dover, New York, 1991).

[17] C. A. Angell, Science **267**, 1924 (1995).

[18] R. Bohmer, K. Ngai, C. Angell, and D. Plazek, J. Chem. Phys. **99**, 4201 (1993).

[19] H. W. Starkweather, Macromolecules **21**, 1798 (1988).

[20] M. W. den Otter, Sensors and Actuators A: Physical **96**, 140 (2002).

[21] H. E. Thomas and C. A. Clarke, *Handbook of Electronic Instruments and Meaurement Techniques* (Prentice Hall, Englewood Cliffs, N. J., 1967).

[22] S. R. Wasserman, Langmuir **5**, 1074 (1989).

[23] J. A. Crowe and J. Genzer, J. Am. Chem. Soc. **127**, 17610 (2005).

[24] I. Luzinov, S. Minko, and V. V. Tsukruk, Progress in Polymer Science **29**, 635 (2004).

[25] I. Luzinov, S. Minko, and V. V. Tsukruk, Soft Matter **4**, 714 (2008).

[26] J. Mano and S. Lanceros-Mendez, J. App. Phys. **89**, 1844 (2001).

[27] S. K. Gupta and W. P. Weber, Macromolecules **35**, 3369 (2002).

[28] M. J. Sanchis, R. Diaz-Calleja, O. Pelissou, L. Gargallo, and D. Radic, Polymer **45**, 1845 (2004).

[29] K. Tadano, Y. Tanaka, T. Shimizu, and S. Yano, Macromolecules **32**, 1651 (1999).

[30] B. A. Bedekar, Y. Tsujii, N. Ide, Y. Kita, T. Fukuda, and T. Miyamoto, Polymer **36**, 4735 (1995).

[31] K. Mohomed, T. G. Gerasimov, F. Moussy, and J. P. Harmon, Polymer **46**, 3847 (2005).

[32] S. Koizumi, K. Tadano, Y. Tanaka, T. Shimidzu, S. Kutsumizu, and S. Yano, Macromolecules **25**, 6563 (1992).

[33] J. Fendler, Chem. Mats. **13**, 3196 (2001).

[34] X. Li, J. Huskens, and D. Reinhoudt, J. Mat. Chem. **14**, 2954 (2004).

[35] R. Smith, P. Lewis, and P. Weiss, Prog. Surf. Sci. **75**, 1 (2004).

[36] N. Katsonis, M. Lubomska, M. M. Pollard, B. L. Feringa, and P. Rudolf, Prog. Surf. Sci. **82**, 407 (2007).

[37] N. Chaki and K. Vijayamohanan, Biosensors & Bioelectronics **17**, 1 (2002).

[38] S. Wise, J. Chrom. A **642**, 329 (1993).

[39] Y. Saito, H. Ohta, and K. Jinno, J. Sep. Sci. **26**, 225 (2003).

[40] L. Sander and S. Wise, J. Chrom. A **656**, 335 (1993).

[41] M. Hostetler and R. Murray, Current Opinion in Colloid & Interface Science **2**, 42 (1997).

[42] A. Badia, R. Lennox, and L. Reven, Acc. Chem. Res. **33**, 475 (2000).

[43] F. Schreiber, Prog. Surf. Sci. **65**, 151 (2000).

[44] C. Vericat, M. Vela, and R. Salvarezza, Phys. Chem. **7**, 3258 (2005).

[45] M. Maroncelli, S. Qi, H. Strauss, and R. Snyder, J. Amer. Chem. Soc. **104**, 6237 (1982).

[46] R. Lam and P. Geil, Poly. Bull. **1**, 127 (1978).

[47] M. Beiner and H. Huth, Nat. Mater. **2**, 595 (2003).

[48] Q. Zhang, Q. Zhang, and L. Archer, J. Phys. Chem. B **110**, 4924 (2006).

[49] L. Clarke, D. Horinek, G. Kottas, N. Varaksa, T. Magnera, T. Hinderer, R. Horansky, J. Michl, and J. Price, Nanotechnology **13**, 533 (2002).

[50] R. D. Horansky, Physical Review B **74**, 054306 (2006).

[51] R. D. Horansky, Physical Review B **72**, 014302 (2005).

[52] A. Ulman, *An Introduction to Ultrathin Organic Films: from Langmuir-Blodgess to Self-Assembly* (Academic Press, Boston, 1991), p. 442.

[53] J. Genzer, Langmuir **18**, 9307 (2002).

[54] T. Ozaki, T. Ogasawara, T. Kosugi, and T. Kamada, Physica B **263**, 333 (1999).

[55] M. Pomerantz, A. Segmuller, L. Netzer, and J. Sagiv, Thin Solid Films **132**, 153 (1985).

[56] M. Grimau, E. Laredo, F. Sanchez, F. Lopez-Carrasquero, M. E. Baez, and A. Bello, Eur. Phys. J. E. Soft Matter **15**, 383 (2004).

[57] A. Genix and F. Laupretre, Macromolecules **38**, 2786 (2005).

[58] Y. Liu, L. K. Wolf, and M. C. Messmer, Langmuir **17**, 4329 (2001).

[59] R. F. Boyer, Macromolecules **6**, 288 (1973).

[60] P. V. K. Pant, J. Han, G. D. Smith, and R. H. Boyd, J. Chem. Phys. **99**, 597 (1993).

[61] K. L. Ngai and C. M. Roland, Macromolecules **26**, 6824 (1993).

[62] R. H. Boyd, R. H. Gee, J. Han, and Y. Jin, J. Chem. Phys. **101**, 788 (1994).

[63] G. D'Angelo, G. Tripodo, G. Carini, A. Bartolotta, G. Di Marco, and G. Salvato, J. Chem. Phys. **109**, 7625 (1998).

[64] V. N. Novikov, E. Rossler, V. K. Malinovsky, and N. V. Surovtsev, Europhys. Lett. **35**, 289 (1996).